AN AB INITIO STUDY OF THE STRUCTURAL, MAGNETIC, AND ELECTRONIC PROPERTIES OF TRANSITION METAL OXIDES

A Dissertation

Presented to the Faculty of the Graduate School

of Cornell University

in Partial Fulfillment of the Requirements for the Degree of

Doctor of Philosophy

by

Turan Birol

August 2013

AN AB INITIO STUDY OF THE STRUCTURAL, MAGNETIC, AND ELECTRONIC PROPERTIES OF TRANSITION METAL OXIDES

Turan Birol, Ph.D.

Cornell University 2013

Transition metal oxides form a large class of compounds that exhibit a very rich and diverse physics. This thesis involves a first-principles computational study of some transition metal oxides and their different physical properties. We study the emergence of ferroelectricity in Sr-Ti-O layered perovskites with strain, the microscopic mechanism of magnetodielectric coupling in $EuTiO_3$, and the structural trends of early transition metal dioxides with the Rutile structure. We explain and support the results of our first-principles calculations with physical models for each system.

BIOGRAPHICAL SKETCH

Turan Birol was born in Sivas, Turkey in 1983. He graduated from Ankara Atatürk High School in 2001 and received his BSc in Physics with high honors from the Middle East Technical University with a minor in Logic in 2005. After receiving a MS in Physics from Koç University in 2007, he started his Physics PhD studies at Cornell University. He joined the group of Craig J. Fennie in 2009.

to my parents,

and to the people of my country,

with all their good, and all their bad...

ACKNOWLEDGEMENTS

While my original intention was to have a complete list of people to whom I am in debt and the reasons why I am so; I realize that this is practically impossible as such a list would be too long. For this reason, I will not really mention my previous teachers, like Ilksen; or old friends, like Bayram, Kutay, Gizem, Elif, Sarp, or Didem; or any of my role models, such as H.T. Tassadar. I will focus only on the physics and Cornell people.

Of course, I will make an exception for my family, for I guess I have finally reached the age at which one feels that romantic admiration towards his parents. I am unmeasurably thankful for both my parents for doing their best for me. I wish my mother could live to see this day as well - she would probably scold me for still being not-married, but would nevertheless be happy. My brother obviously deserves to be thanked as well: Our noisy and violent quarrels certainly built up character. Hopefully in a good way.

My advisor Craig has been very understanding and helpful about so many things, both professional and personal, during my PhD. I can see many ways that things could have gone bad if I had someone else as my advisor, so I am very thankful to him. I should also thank to various past and present members of the Fennie Group for all the time together. Among them Nicole deserves a separate thank you for the long lunch breaks at CTB, and listening to my endless ranting. I should also not forget to mention Johannes (Herr Doktor).

My physics friends here in Ithaca made this little city so much better than I could ever imagine. In this respect, Stephen, Yj, Shankar, Hitesh, Colwyn, Jolyon, Kendra, Katie, Melina, Ben, and various others deserve a big thank you. The homework sessions, hikes, get-togethers, and even the green man incident were so much fun. The Turkish Mafia at Cornell; including, but not limited to

Erdal, Yucel, Onur, Deniz, Baris, Damla, and Cagatay, also deserve to be mentioned given how much they helped me feel less home-sick especially in my first years around here. I am also thankful for the Turkish physics gang with whom I have stayed in touch both here on the East Coast and during my visits to Turkey; Cesim, Serkan, Nadir, Can, Sururi, Ziya, and again, various others.

Finally, there are two very special people who have been exposed to me in a way different from everyone else, and deserve a thank you for that. Nora was by my side for a good chunk of my time in Ithaca, and has been extremely supporting and helpful. I am thankful to her for a lot of things, such as getting me used to tofu. April, while she has been around me for only the good part of a year, introduced me to so many new things and contributed to my life in a very positive way. I am still not sure why she bothers hanging out with me, but I hereby thank her all that she has done, including the games she plays with my subconscious mind.

TABLE OF CONTENTS

LIST OF TABLES

LIST OF FIGURES

CHAPTER 1

INTRODUCTION AND METHODS

1.1 Introduction

Understanding the behavior of electrons in solids has been a major challenge for the physics of the 20th and the early 21st centuries. Even though the fundamentals of the quantum theory were established in 1920s, and calculations on the electrons in atoms were attempted immediately (for example see [77, 76, 44, 73]), the electronic structure of solids still provide open problems to this date. While a detailed review of the complexity of these calculations is beyond the scope of this brief introduction, it is possible to justify the growing interest on them by the richness of new physics that emerges at different scales. We can summarize this in one sentence by the famous motto of solid state physics: "More is different" [5].

Transition metal (TM) oxides is a class of materials that have been in the focus of intense research in the fields of Physics, Chemistry, and Materials Science for almost a century now. They exhibit a very wide range of interesting phenomena; of which ferroelectricity, multiferroicity, metal-insulator transitions, and high temperature superconductivity are just a few. As a result, the amount of research effort focused on TM oxides and the various orders observed in these systems (including, but not limited to, various structural (ferroelectric, ferrodistortive, antiferrodistortive, etc.) as well as different magnetic and orbital orders) is increasing every day. The interplay of these phenomena render the TM oxides a uniquely rich playground for solid state physics.

Both the development of advanced techniques and increasing computer power lead to a surge of computational studies on TM oxides. State of the art first principles methods provide a powerful arsenal to approach the physics of TM oxides, and can be used not only to support and explain experimental results but also to make predictions and guide the experiments. Even though the necessary basic physical laws are known, as discussed above, these methods provide new physical understanding about the complex emergent physics of TM oxides.

This thesis involves a study on the TM oxides and part of the rich physics they host from a computational theory perspective. It consists of three main parts, each of which focus on a specific compound or group of compounds that exhibit a different phenomenon. They are:

- A study of the strain-tunability of ferroelectricity in Sr-Ti-O Ruddlesden-Popper compounds, and a novel polar state that emerges because of the competition of ferroelectricity with antiferroelectricity in them [23]. This part is an example of how the first-principles approaches can be used to study the structural instabilities and phase transitions in TM oxides.
- A study of the microscopic mechanism of the magnetoelectric coupling in $EuTiO_3$, the effect of rare earth f electrons on the dielectric properties and crystal dynamics in this compound, and the connection between the oxygen octahedral rotations with magnetism and ferroelectricity [83, 143]. This part shows how first-principles approaches provide unique capabilities to perform thought experiments that probe the microscopic mechanisms behind the macroscopic properties of materials.
- A study on the structural trends in early 4d and 5d TM dioxides with the

rutile structure, and their connection with the electronic structure. It involves a detailed study of a large number of compounds and performing calculations that isolate certain properties, such as the coupling of structural distortions to strain, which is not possible to achieve without use of computational methods.

The method that has been used throughout these studies is the Kohn-Sham Density Functional Theory [109]. We start by providing a very brief background on our methods in Section 1.2. We then present our studies on the ferroelectricity in $SrTiO_3$, the multiferroicity in $EuTiO_3$ and the structural trends of the rutile compounds in Chapters 2, 3, and 4 respectively. Conclusions are in Chapter 5.

1.2 Methods

In this section we give a very brief background on the methods that we use. A very good discussion of almost everything in this section is present in the manuscript of Martin (Ref. [109]).

1.2.1 Schroedinger Equation for Electrons in the Adiabatic Approximation

The basic Hamiltonian that governs the physics of electrons interacting with atomic nuclei is

$$H = -\sum_i \frac{\hbar^2}{2m_e}\nabla_i^2 - \sum_{i,I} \frac{Z_I e^2}{|\vec{r}_i - \vec{R}_I|} + \frac{1}{2}\sum_{i\neq j} \frac{e^2}{|\vec{r}_i - \vec{r}_j|} - \sum_I \frac{\hbar^2}{2M_I}\nabla_I^2 + \frac{1}{2}\sum_{I\neq J} \frac{Z_I Z_J e^2}{|\vec{R}_I - \vec{R}_J|} \quad (1.1)$$

where small latin indices refer to the electrons, capital latin indices refer to the nuclei, $\vec{r}$ and $\vec{R}$ are the positions of the electrons and the nuclei, m_e is the mass of the electron, M_I and Z_I are the masses and charges of the nuclei, e is the charge of the electron, and $\hbar$ is the Planck's constant [109]. The wavefunction Ψ of the system is a function of the positions of both the electrons and the nuclei, and is in general not seperable in them; i.e. the electronic and nuclear degrees of freedom can be entangled. However, since the nuclear mass is much larger than the electronic one, there is a separation of scales. As a result, we can make the approximation

$$\Psi = \Psi_e \cdot \Psi_n \tag{1.2}$$

where the electronic wavefunction Ψ_e is a function of only the electronic coordinates, and the nuclear wavefunction Ψ_n is a function of only the nuclear coordinates. This is the first step of the so called Born-Oppenheimer approximation. It results in an electronic Schroedinger equation that has the form

$$\begin{aligned} H\Psi_e &= E\Psi_e & (1.3)\\ &= \left(-\sum_i \frac{\hbar^2}{2m_e}\nabla_i^2 + \frac{1}{2}\sum_{i\neq j}\frac{e^2}{|\vec{r}_i - \vec{r}_j|} + V_{ext}\right)\Psi_e & (1.4) \end{aligned}$$

where E is the energy eigenvalue and V_{ext} is the external one-body potential that the electrons feel:

$$V_{ext}(\vec{r}) = \sum_I \frac{Z_I e^2}{|\vec{r} - \vec{R}_I|} \tag{1.5}$$

A further approximation that is commonly made is to consider the nuclei as classical particles that are stationary, and assume that the electrons are always in their ground state. In this regime, solving Eq. (1.3) for the groundstate for fixed nuclear coordinates solves the problem completely. The force on the I^{th} nucleus can then be calculated using the Hellmann-Feynman theorem [54] in terms of the nucleus-nucleus Coulomb energy E_{nn} and the total electronic charge density

$n(\vec{r})$ as

$$\vec{F}_I = -\frac{\partial E_{nn}}{\partial \vec{R}_I} - \int d^3 r n(\vec{r}) \frac{\partial V_{ext}(\vec{r})}{\partial \vec{R}_I} \tag{1.6}$$

Phonon frequencies can be calculated from Eq. (1.6) by defining interatomic force constants as

$$C_{I\alpha J\beta} = -\frac{\partial F_{I\alpha}}{\partial R_{J\beta}} \tag{1.7}$$

and solving the Newton's equations for the nuclei, in the so called Born-von Karman fashion [105, 28]. (The greek indices denote cartesian components.)

This adiabatic approach to phonons can and does indeed fail in two limits. Even tough the nuclear masses are much larger than the electronic one, the quantum fluctuations in the positions of the nuclei can nevertheless be important for lighter nuclei, and also for systems with optical phonons with a small frequency, in other words, systems on the verge of a structural phase transition (for example see [176] and the discussions in Chapters 2 and 3). Also, the approximation that the electrons remain in their groundstate requires that the atomic motion is not rapid enough to excite electrons, i.e., the typical phonon frequency ω is smaller than the electronic gap E_g, $\hbar\omega \ll E_g$. However, for metals, E_g is vanishing, and so phonons decay after a finite lifetime [131]. Nevertheless, the Born-von Karman approach to lattice vibrations provides valuable insight into the lattice dynamics if retardation effects are ignored, and into the structural phase transitions if quantum fluctuations of the nuclei is not significant.

1.2.2 Density Functional Theory

The Hamiltonian of the electrons in a crystalline solid, and the Scroedinger equation which determines the electronic wavefunction is presented in Section

1.2.1. In the words of Dirac, *"The general theory of quantum mechanics is now almost complete. The underlying physical laws necessary for the mathematical theory of a large part of physics and all of chemistry are thus completely known"* [45]. However, the electronic wavefunction Ψ_e of an N electron system is a complex function of $3N$ coordinates, and as a result, is not easy to handle. So, actually solving Eq. 1.3 and obtaining the wavefunction for interacting electrons is not trivial, and in many cases, not even possible.[1]

An approach that can be traced back to the early days of quantum mechanics is to work with the total electronic density $n(\vec{r})$ instead of the many-body wave function [163, 53]. n, being a real function of only three variables, is much easier to handle than Ψ_e. Nevertheless, the original density functional formulation of Thomas and Fermi is far from being precise enough for a practical calculation. The crucial steps that made a density functional theory (DFT) applicable to real systems were taken by Hohenberg, Kohn, and Sham in 1960s. In Ref. [79], Hohenberg and Kohn proved two important theorems (reproduced here from Ref. [109]):

- "For any system of interacting particles in an external potential $V_{ext}(\vec{r})$, the potential $V_{ext}(\vec{r})$ is determined uniquely, except for a constant, by the ground state particle density $n(\vec{r})$."
- "A universal functional for the energy $E[n]$ in terms of the density $n(\vec{r})$ can be defined, valid for any external potential $V_{ext}(\vec{r})$. For any particular $V_{ext}(\vec{r})$, the exact ground state energy of the system is the global minimum value of this functional, and the density $n(\vec{r})$ that minimizes the functional is the exact ground state density."

[1] We emphasize that this is not a practical matter only, but rather an issue of exponential scaling.

These Hohenberg-Kohn theorems prove that for the groundstate, an exact density functional theory can be built. However, obtaining the exact functional $E[n]$ is no easier than solving for the many-body wavefunction Ψ_e: the Hohenberg-Kohn theorems prove only the existence - they do not provide a way to solve for it. In order to solve for density n and the energy, Kohn and Sham came with an ansatz that replaces the original interacting system with a noninteracting system that has the same groundstate density n but under another external potential V_{ext} [88]. The Hamiltonian for this auxiliary system is

$$H_{aux} = -\frac{1}{2}\nabla^2 + V_{KS}(\vec{r}), \tag{1.8}$$

and the density is given by a sum over the occupied orbitals

$$n(\vec{r}) = \sum_i |\phi_i(\vec{r})|^2. \tag{1.9}$$

The kinetic energy part, in terms of the orbitals ϕ_i, is given by

$$T_{KS} = -\frac{1}{2}\sum_i \langle\phi_i|\nabla^2|\phi_i\rangle. \tag{1.10}$$

We also define the Hartree energy as the Coulomb energy of a classical system with density $n(\vec{r})$

$$E_{Hartree} = \frac{1}{2}\int d^3r_1 \int d^3r_2 \frac{n(\vec{r}_1)n(\vec{r}_2)}{|\vec{r}_1 - \vec{r}_2|} \tag{1.11}$$

Putting these together, the ground state energy can be written as

$$E_{KS} = T_{KS} + \int d^3r V_{ext}(\vec{r})n(\vec{r}) + E_{Hartree}[n] + E_{xc}[n]. \tag{1.12}$$

The quantum many-body effects in the form of exchange and correlation energies are included in E_{xc}. Taking the derivative of E_{KS} with respect to $\phi_i(\vec{r})$ gives the Kohn-Sham potential in Eq. (1.8) as

$$V_{KS}(\vec{r}) = V_{ext}(\vec{r}) + V_{Hartree}(\vec{r}) + V_{xc}(\vec{r}), \tag{1.13}$$

$$V_{Hartree}(\vec{r}) = \frac{\delta E_{Hartree}}{\delta n(\vec{r})}, \tag{1.14}$$

$$V_{xc}(\vec{r}) = \frac{\delta E_{xc}}{\delta n(\vec{r})}. \tag{1.15}$$

The Kohn-Sham wavefunctions ϕ_i, energy, etc. can be obtained by solving Eq. (1.8)-(1.15) self consistently. However, in order to have an exact theory, the form of V_{xc} needs to be known. While this is not the case, there are multiple approximations to V_{xc}. Some examples are the so called Local Density Approximation (LDA) or various Generalized Gradient Approximations (GGAs). These approximations introduce errors in the calculated ground state properties, and as a result they should be used with caution. For example, LDA is known to underestimate volumes in solids by few percent, which can have dramatic quantitative effects on the dielectric properties of oxides. Nevertheless, very often, the use of an approximate V_{xc} is justified by the small errors and the computational ease.

1.2.3 DFT+U

LDA performs surprisingly well in various compounds, and it gives very robust results especially for crystal structure and dynamics. However, despite its success, there is also a tremendous range of materials that it fails in and physical properties that it cannot reproduce. An example is the *strongly correlated* materials that have ions with partially filled d or f shells. For example, it has been noticed early on [42] that while LDA reproduces the lattice stability for the parent compound of high-T_c oxide superconductors correctly, it often predicts them to be metallic. However, these compounds are antiferromagnetic insulators. There are numerous other examples; even the simple electronic structure

of classical oxides such as MnO or NiO, which are antiferromagnets, cannot be reproduced by LDA correctly [125], and LDA predicts them to be nonmagnetic.

These issues are not essentially problems of DFT but rather that of LDA. While DFT is exact, LDA is not, and it is problematic especially in situations that are far from the homogenous electron gas which is the starting point of LDA. In particular, the derivative discontinuity of the energy [129] does not exist for the homogenous electron gas, so LDA or simple GGAs cannot reproduce this discontinuity. At this point, one can consider abandoning LDA altogether and resorting to advanced methods such as configuration interaction. Another approach is to consider extensions of DFT that correct for shortcomings of LDA. An example is the so called Self Interaction Correction (SIC) method [81, 109], which involves canceling the nonphysical interaction of the electrons by themselves in the DFT+LDA scheme. There are also the Hybrid Functionals which add some exact Hartree-Fock exchange [15, 128]. However, these methods all bear enormous computational cost.

In this work, we use only a simple yet robust method, DFT+U, which is an extension of DFT+LDA with virtually no extra energy cost. While it has shortcomings of its own, DFT+U provides significant improvements over LDA in various properties and systems. In particular, it predicts the correct groundstate for the aforementioned systems like MnO. The major reason that LDA fails in reproducing the magnetic state in these systems is that it cannot take into account the strong Coulomb interaction of localized electrons in systems such as Mott insulators. The magnetism in a homogenous electron gas is due to the exchange interaction between delocalized electrons and can be explained by the Stoner physics. While LDA can properly describe the Stoner physics, it fails to repro-

duce the correlated physics of the Hubbard-like terms that is the driving force of spin (and orbital) polarization in various insulating transition metal oxides [7, 46]. This strongly correlated physics, however, is known to be explained well with Hamiltonians like the Hubbard or Anderson impurity models. DFT+U is a (static) mean field method that introduces the Hubbard physics of the strongly correlated d or f orbitals to the DFT+LDA calculations. The particular flavor of DFT+U we use involves adding a potential to the atomic d or f orbitals [7]:

$$V_{m\sigma} = U \sum_{m'} \left(n_{m',-\sigma} - n^0 \right) + (U - J) \sum_{m' \neq m} \left(n_{m'\sigma} - n^0 \right). \tag{1.16}$$

Here, the sums are over the local (atomic-like) orbitals which have occupations $n_{m\sigma}$, and average occupation n^0. σ denotes the spin. It is possible to calculate the two undetermined parameters U and J from first-principles [96], or they can be fitted to experimental measurements of a quantity of interest. In either case, scanning a range of U and J values to check for robustness of the physical results is necessary. Also, there is arbitrariness in the choice of the orbitals that this potential is added to, which is a shortcoming of the DFT+U method as presented in Eq. 1.16. However, there are ways to overcome this issue and achieve basis set independent realizations of DFT+U [103].

Physically, U corresponds to the Hubbard parameter, which adds an energy cost of occupying a state that is proportional to the total occupation of all the other states. This way, it makes up for the strong Coulomb repulsion between electrons occupying these states. Screening effects should be taken into account when determining the quantitative value of U since the s-p, d-s etc. transitions are faster than the d or f electrons' fluctuations and hence can screen them [7]. (This latter fact also justifies the applicability of model Hamiltonians with only few local degrees of freedom to such systems.) One usually uses a U that is no larger than $\sim 6 - 8$ eV for 3d electrons, and even smaller values for the lower

rows of the periodic table, which are much smaller than the atomic values. J can be associated with the Stoner parameter which aligns spins in different orbitals. It adds an energy gain for occupying parallel spin states. Its typical energy scale is much smaller than U and is less than $\sim$ 1 eV. While the quantitative value of J is usually considered not to be as important as U, there are studies that underline its significant effects, for example in noncollinear magnetic systems [30].

Note that in the Hubbard hamiltonian for a single site,

$$E \sim U \sum_{m,\sigma,m',\sigma'} n_{m\sigma} n_{m'\sigma'}, \tag{1.17}$$

the spin and orbital polarizations are treated on equal footing. Since it is energetically favorable to concentrate occupation on as few states as possible, orbital polarization is induced as well as the spin polarization [7]. This improves the properties of Mott insulators in DFT since an orbital polarization is necessary to open a Mott-Hubbard gap away from half filling of the d or f orbitals [103]. Orbital polarization is also necessary for the orbital ordering observed in Jahn-Teller compounds such as $KCuF_4$. These compounds displays a crystal structure that goes along with an ordering of the occupation of d orbitals on the Cu ion. It is shown in [103] that LDA fails to reproduce both the orbital order and the crystal structure, but LDA+U predicts the correct crystal structure, as long as orbital polarization is allowed. (Note that for this type of calculations the basis set independence of the particular DFT+U formulation used is essential, since the electronic structure itself is required to break the orbital symmetry.)

The DFT+U method also reintroduces the derivative discontinuity of the energy functional that is missing in the LDA (or GGA) form of the exchange-correlation energy. To see this more clearly, we ignore J and switch to an al-

ternative DFT+U formulation due to Dudarev et al. [46] which is rotationally invariant and involves adding the following term to the Kohn-Sham energy:

$$E_{Dudarev} = \frac{U_{eff}}{2} \sum_{m,\sigma} \left(n_{m,\sigma} - n_{m,\sigma}^2 \right). \tag{1.18}$$

This introduces an energy cost that is vanishing when total number of electrons N is integer. Near integer N, $E_{Dudarev}$ is linearly increasing for both increasing and decreasing N, which creates a kink and hence a derivative discontinuity. The derivative discontinuity is missing from LDA because it approximates the convex, piecewise linear energy functional with a smooth function. The discrepancy between the real functional and the LDA approximation is minimum for integer N and as a result $E_{Dudarev}$ tries to make up for the difference between them. (For a pedagogical exposition of this point, see the discussion and Fig. 3.1 in [39].)

Adding a term that favors integer occupation to the Hamiltonian obviously can change the hybridization of an atom with others as well. This, in turn, can lead to changes in covalent bonding and the quantitative features such as Born Effective Charges [62] and the value of electronic contribution to electric polarization. While it is not argued explicitly in the literature, LDA tends to overestimate the electronic contribution to polarization. For example, it has been noticed more than a decade ago in [62] that the polarization of $BaTiO_3$ calculated from Born Effective Charges from LDA is about $\sim$ 30 % larger than the experimental value even when the experimental lattice structure is used in the calculations. It can be argued that the shortcomings of LDA about the correlations on the B-site Ti atom's d orbitals makes it easier for the O atoms' occupied p states to hybridize with the Ti ion, thus making it less costly for charge to be transferred from O to Ti ion when polarization sets in, increasing the Born Effective Charges and hence the polarization. The results of our calculations (not

shown) indicate that using the LDA+U formalism and adding a Hubbard-U to the Ti *d* orbitals indeed decreases the anomalously large effective charge of Ti ion thus reproduces a polarization that agrees better with experiment. An extreme example of a similar case is the improper ferroelectric $HoMn_2O_5$, which has a large electronic polarization that is induced by the symmetry breaking by the collinear antiferromagnetic order and the resulting spin-dependent hybridization [64]. It is shown in [64] that depending on the value of U used, the polarization in the same crystal structure is not only 'decimated' but can even change sign. LDA+U also corrects the overestimation of polarization in the similar compound $TbMn_2O_5$ [36].

We conclude our discussion of DFT+U method by briefly mentioning some alternatives to it. A commonly used alternative is the hybrid functionals, which involve adding a fraction of exact Hartree-Fock exchange to the LDA exchange correlation energy (for example, see [122]). This cancels some of the exchange interaction of the electrons by themselves, and as a result lead to improvements. Hybrid functionals have been extensively used for TM oxide systems, are shown to give good results for, for example, the spin-phonon coupling in various compounds [80, 3]. The insulating phase of VO_2, which cannot be reproduced by DFT+U, is predicted correctly by the Hybrid functionals thanks to the nonlocal nature of the exact exchange added [49]. However, the computational cost of Hybrid functionals, while spanning a wide range depending on the formulation, is significantly larger than DFT+U. There exist meta-GGA's [160], which are significantly cheaper than hybrid functionals. They involve an exchange-correlation energy that depends not only on the density and its gradient but also on the kinetic energy density. While they have found widespread use in chemistry literature, the use of meta-GGA's in physics community is not

wide spread so far. (For example, the study on the implementation of meta-GGA's in a Projector Augmented Wave framework, Ref. [159], has accumulated only five citations in about two years.)

In summary, DFT+U has proven very successful for various TM oxide systems despite its simplicity. It bears no extra computational cost on top of DFT, and is easy to implement. As a result, it is now implemented in pretty much all widespread DFT packages. There exist other methods, such as Dynamical Mean Field Theory which includes and goes beyond DFT+U; however, the low computational cost associated with DFT+U, as well as its simplicity that renders the results easy to analyze, makes it a very useful and popular tool.

1.2.4 The Projector Augmented Wave Method

In this section, we very briefly introduce the Projector Augmented Wave (PAW) method, which is used to make the numerical DFT calculations more feasible. Throughout the work presented in this thesis, the PAW method as implemented in the Vienna Ab initio Simulation Package (VASP) is extensively used. Further details of the method and comprehensive discussions of it can be found in [24, 109].

In real materials, the wavefunctions of the electrons exhibit very different characteristics near the atoms than they do far from them. Near the atoms, the wavefunctions oscillate very rapidly, and atomic orbitals form a suitable basis to expand them. In the space between the atoms, on the other hand, the wavefunctions are more easily expanded in terms of planewaves. The PAW method provides both a means to describe the wavefunctions with high accuracy, and also

a degree of freedom that can be used to choose a computationally convenient basis. In the PAW formalism, the space is divided into two parts: in the so-called augmentation region (Ω) near the atoms, the wavefunctions are expanded in the atomic orbitals, whereas outside the augmentation region planewaves are used for the same purpose. On the boundary of Ω, boundary conditions are imposed to match the two expansions and their derivatives.

The PAW formalism also involves transforming the physical wavefunctions $|\Psi\rangle$ to wavefunctions in a pseudo (PS) Hilbert space $|\tilde{\Psi}\rangle$ by a linear operator: $|\Psi\rangle = T|\tilde{\Psi}\rangle$. The PS wavefunctions $|\tilde{\Psi}\rangle$ are equivalent to to $|\Psi\rangle$ outside the augmentation region but differ from them inside it. Expectation value of any operator $\hat{A}$ can be calculated using the PS wavefunctions as $\langle\Psi|A|\Psi\rangle = \langle\tilde{\Psi}|T^{\dagger}\hat{A}T|\Psi\rangle$. Since Ψ and $\tilde{\Psi}$ differ only the augmentation region Ω, T is equivalent to identity outside Ω and hence it can be written as

$$T = 1 - \sum_i (|\phi_i\rangle - |\tilde{\phi}_i\rangle)\langle\tilde{p}_i|. \tag{1.19}$$

Here, $|\phi_i\rangle$ and $|\tilde{\phi}_i\rangle$ are the *partial waves* that are used to expand the wavefunctions in the physical and PS hilbert spaces respectively, and $\langle\tilde{p}_i|$ are the *projector functions* which are localized in Ω. The partial waves in the two spaces have a one to one correspondence, i.e.

$$|\tilde{\Psi}_i\rangle = \sum_i c_i|\tilde{\phi}_i\rangle, \tag{1.20}$$

and

$$|\Psi_i\rangle = \sum_i c_i|\phi_i\rangle \tag{1.21}$$

with the same coefficients $c_i = \langle\tilde{p}_i|\tilde{\Psi}\rangle$.

An advantage of defining the projectors and working in the PS Hilbert space is that the operators are invariant under the addition of another operator of the

form

$$\hat{B} - \sum_{i,j} |\tilde{p}_i\rangle\langle\tilde{\phi}_i|\hat{B}|\tilde{\phi}_j\rangle\langle\tilde{p}_j| \tag{1.22}$$

with $\hat{B}$ localized in the augmentation region. This freedom can be exploited to remove the singularities like the one that the Coulomb interaction has near the origin. This renders the results less sensitive to energy cutoff of the plane waves, making numerical calculations less costly. As we do not make any development of the PAW formalism but only use it as implemented in publicly available software packages, we do not elaborate further and refer to the literature for details of it [24, 94, 109].

CHAPTER 2

FERROELECTRICITY IN LAYERED PEROVSKITES $Sr_{n+1}Ti_nO_{3n+1}$

In this chapter, we study the quantum paraelectric $SrTiO_3$ and the closely related compounds $Sr_{n+1}Ti_nO_{3n+1}$ with the Ruddlesden-Popper (RP) structure [23, 140, 141]. The RP compounds provide a extra degree of freedom to the perovskite structure: the layering (n). We analyze in detail how a ferroelectric instability emerges with increasing n and strain, and provide a model that explains the ferroelectric soft-mode behavior and is consistent with the first-principles calculations. We also predict a novel polar state which involves degenerate ferroelectric and antiferroelectric states in these materials. Finally, we briefly compare our results with experimental observations.

Understanding the ferroelectric behavior of the Sr-Ti-O RP compounds is important because these materials can be tuned to the verge of a parelectric–ferroelectric transition to achieve a large dielectric response. Also, they are observed to accommodate nonstoichiometry by shear planes and thus resist to defect formation [100]. This reduces the significant dielectric loss due to the defects, and hence leads to a very high figure of merit in microwave tunability.

2.1 Introduction

Control over the emergence of (anti)ferroelectric and antiferrodistortive order remains a fundamental challenge for the atomic-scale rational design of new phenomena. Complex oxide heterostructures, layered thin-films, and other low-dimensional systems provide a novel platform to address this ongoing challenge. There have been two well-explored approaches to control ferroicity in

these systems: epitaxial strain engineering – which has been used to induce ferroelectricity [70], multiferroicity [20] and to create strongly coupled multiferroics [52] – and tailoring electrostatic boundary conditions. A significant challenge in the field of ferroelectric thin-films has been understanding the evolution of the spontaneous polarization ($P_\perp$ in Fig. 2.1) in ferroelectric/paraelectric heterostructures [119] and ferroelectric nanoscale thin film capacitors as the dimension parallel to the polarization direction is reduced [90, 82, 168, 155, 144]. Today it is clear that this is driven almost entirely by the electrostatic depolarizing field arising at the interface.

(Anti)Ferroelectric and antiferrodistortive distortions are cooperative phenomena involving the coherent motion of atoms extending over many unit cells [104]. Therefore, these ferroic states may also be greatly influenced by introducing a perturbation with a characteristic length scale below (or near) that of the coherence length of the ferroic distortion [21, 63]. Design strategies based on such an effect have lead to the emergence of many novel ferroic states, such as multiferroicity [151] and relaxor ferroelectricity. The ability to control ferroic order on the scale of the coherence length therefore represents an opportunity to understand and create novel ferroic phenomena. However, in bulk materials, the only known tuning mechanisms are atomic disorder (which in many cases tends to introduce electronic defects that are detrimental to the desired properties) or free surfaces [112]. Clearly, alternative pathways are desired.

In this chapter we show how a complex oxide interface can exploit the coherence length of a ferroic instability in a controlled way and use it to design an unusual polar state in which ferroelectricity is nearly degenerate with antiferroelectricity, a relatively rare form of ferroic order. In contrast to the well studied

'finite-size effects' problem in (anti)ferroelectrics [29], the physics discussed here involves the emergence of local polar instabilities in a direction parallel to the interface. For such an in-plane direction, the polarization ($P_{\parallel}$ in Fig. 2.1) never comes 'in contact' with the interface, electrostatic boundary conditions correspond to a short circuit, perfect screening of the depolarization field is always achieved and the system is structurally infinite.

As a model system we take the perovskite/rocksalt interface in the naturally occurring Ruddlesden-Popper (RP) layered perovskite, $Sr_{n+1}Ti_nO_{3n+1}$. Dielectric studies and previous first-principles calculations have shown that low-n members of the series ($n = 1 - 5$) are paraelectric with low dielectric permittivities [69, 121, 101]. This is surprising given that the structure of the RP homologous series [140, 141], alternatively written as $(SrTiO_3)_n/(SrO)$, can be thought of as that of a $SrTiO_3$ perovskite with an extra SrO monolayer inserted every n perovskite unit cells along [001] as shown in the inset of Fig. 2.1. $SrTiO_3$ (the $n = \infty$ member of the RP series) is a well-known quantum paraelectric (QP) that displays a large dielectric constant (≈10,000 at low temperature) and can be driven ferroelectric with the application of a modest amount of biaxial strain [70, 8].

The key discovery we make is that structural relaxations occurring at the RP fault, that is, at the $SrO/SrTiO_3$ interface, break the coherence of the infinitely long Ti-O-Ti chains parallel to the interface in different perovskite slabs. Even at a tensile strain value more than sufficient to drive $SrTiO_3$ ferroelectric (where the polarization lies in-plane, $P_{\parallel}$), here we find that the $n = 1$ RP is still very far from displaying a polar instability, even though the electrical boundary conditions and the length of the Ti-O-Ti chains in the relevant direction are identical to that of $SrTiO_3$. An in-plane polar state must emerge with increasing n [101],

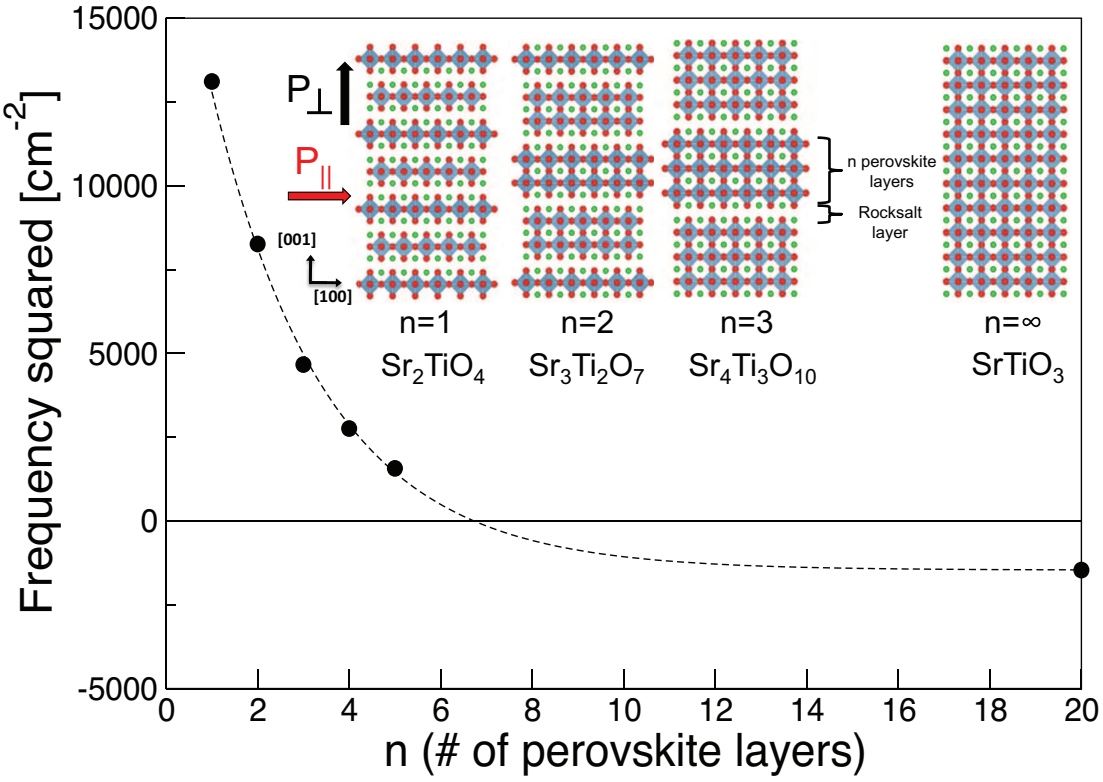

Figure 2.1: (Inset) The Ruddlesden-Popper, $Sr_{n+1}Ti_nO_{3n+1}$, homologous series showing two possible polarization directions: in-plane, $P_{\parallel}$, and out-of-plane, $P_{\perp}$. (Main figure) Calculated in-plane polar phonon frequency as a function of n for a fixed in-plane lattice constant of $SrTiO_3$. (Dots are first-principles calculations, curve is a fit to a single exponential.)

the nature of which and how or why this happens is unknown. In the remainder of this chapter we explore these questions and show how, unlike in $SrTiO_3$, epitaxial strain does not induce ferroelectricity in these materials. Instead, we elucidate the novel role of strain in tuning the perpendicular coherence length of the polar mode and use it to tune a system to a region of the phase diagram where ferroelectricity and antiferroelectricity compete with each other.

2.2 Methods

We performed density-functional theory (DFT) calculations within the PBEsol approximation using PAW potentials, as implemented in VASP [95, 93, 24, 94]. The wavefunctions were expanded in plane waves up to a cutoff of 500 eV. Integrals over the Brillouin zone were approximated by sums on a Γ-centered k-point mesh consistent with an 8×8×8 mesh for the primitive perovskite unit cell. A low force threshold of 0.5 meV/Å was used for all geometric relaxations in order to resolve the small energy differences. Phonon frequencies and eigendisplacements were calculated using two methods: the direct method using symmetry adapted modes in VASP and Density Functional Perturbation Theory (DFPT) as implemented in the Quantum Espresso package. For the DFPT calculations, Vanderbilt Ultrasoft Pseudopotentials were used within Local Density Approximation. We ignore quantum fluctuations of nuclei and therefore bulk $SrTiO_3$ is predicted to have a ferroelectric ground state (See Section 2.8.3).

2.3 Coherence Length

To begin to unravel the novel polar state that emerges in strained RP phases, we calculate the in-plane polar (E_u) phonon frequencies of the $n = 1$ to $n = 5$ members and the $n = \infty$ bulk. We fix the in-plane lattice constant of all RP structures to that of theoretical $SrTiO_3$, $a = 3.899$ Å. Note that the equilibrium in-plane lattice constant a increases monotonically with increasing n; the $n = 1$ member, Sr_2TiO_4, has a 0.5% smaller lattice constant than bulk perovskite $SrTiO_3$. As Fig. 2.1 shows, the soft mode frequency decreases monotonically with increasing n, even though the in-plane lattice constant was fixed to the same value for

all n (and therefore the in-plane strain is actually decreasing with increasing n). Such a trend is surprising. The observed decay of the phonon frequency with increasing n can in fact be easily modeled. It is exactly what one would find in a toy model calculation of the interplanar force constants of a finite thick, infinite slab as more layers are added to the slab (see Section 2.8.2). It is, however, not clear why the RP phases, which are bulk materials, should display this kind of crossover from two-dimensional to three-dimensional behavior as n increases, given that the Ti-O-Ti chains are continuous and infinite parallel to the direction of the polar mode. Additionally, why does the polar mode of the $n = 1$ member have such a high frequency? We propose that in $SrTiO_3$ there is a coherence length perpendicular to the direction of the polar mode and that coherence between different perovskite blocks is broken by the double rocksalt layers in the RP phases, effectively reducing the dimensionality of the system. There are therefore two questions that need to be answered: (1) does it make sense that a perpendicular coherence length exists in $SrTiO_3$ and if so can it be manipulated? and (2) can the double rocksalt layer really suppress the coherence between perovskite blocks?

2.4 Critical Thickness

Our basic premise is that the real-space coherence requirements of the lattice instabilities in the RP phases can be deduced from the phonon dispersion curves of the bulk cubic perovskite. Fig. 2.2a shows that there are two main instabilities for bulk $SrTiO_3$: an R-point instability involving rotations of the oxygen octahedra, and the unstable polar mode at Γ. An alternative way to visualize the distribution of lattice instabilities in reciprocal space is by plotting the

$\omega^2 = 0$ isosurface in the first Brillouin zone [175, 63], Fig. 2.2(b). The enclosed volumes on the zone boundary correspond to the *R*-point octahedral rotation instability and the FE instability is associated with the volume in the zone center. We point out that this picture is similar to that obtained by Lasota *et al.*, [97] who previously considered the coherence properties of the *R*-point rotation instability only. Fig. 2.2(a) shows that the branch stemming from the Γ instability becomes stable at wave vectors away from Γ in all the of high symmetry directions – towards X, M or R – and is therefore localized in reciprocal space to a finite volume around the zone center.

From Fig. 2.2(b) it is seen that the volume of the FE instability has a strongly anisotropic structure: it consists of three perpendicular disks. Each disk encloses wave vectors that have an instability involving ionic displacements in the direction perpendicular to the plane of the disk. The finite thickness of the disks, corresponding to a finite longitudinal coherence length, $l_{\parallel} \sim 1/q_{\parallel}$, has been previously discussed in perovskite ferroelectrics such as $BaTiO_3$ [63] and $KNbO_3$ [175]. The finite radius of the unstable disks in the reciprocal space found in $SrTiO_3$ suggests that the frequency of the unstable branch also depends on the perpendicular component of the wavevector, corresponding to a finite perpendicular coherence length, $l_{\perp} \sim 1/q_{\perp}$ (See Section 2.8.1). In contrast, in $BaTiO_3$ [63] and $KNbO_3$ [175] the isosurfaces consist of three almost perfectly flat slabs that are infinitely extended, indicating that the frequency of the unstable branch is the same regardless of the component of the wavevector that is perpendicular to the direction of the ionic displacements. This implies that the critical thickness for an infinite slab of $BaTiO_3$ is zero [59].

Assuming the rocksalt layers break the perpendicular coherence between

different perovskite blocks (we will shortly prove this is true), the non-vanishing critical thickness required for ferroelectricity in $SrTiO_3$ imposes a geometric condition, n_{crit}, for RPs to display an in-plane ferroelectric instability; $n < n_{crit}$ members cannot have an energy lowering FE distortion simply because the number of perovskite blocks between the rocksalt layers do not satisfy the coherence condition. However, as n increases, the structures should get closer to the FE transition. This is exactly what we have shown in Fig. 2.1, where the soft mode frequency ω vanishes at $n_{crit} \sim 7$, agreeing with the lower bound from the reciprocal space picture of the instability of $SrTiO_3$.

2.5 Tuning the Coherence Length

The effects of strain [43] and pressure [146] on ferroelectricity in perovskites are well known; they alter the balance between the short-range forces (which favor the centrosymmetric state) and long-range Coulomb forces (which favor the ferroelectric state). But what are their effects on the coherence requirements? In Fig. 2.2 (b) and (c) we plot the phonon dispersion curves and the corresponding $\omega^2 = 0$ isosurfaces of cubic $SrTiO_3$ for isotropic tensile strains of 0.6% and 1.7%, respectively. As shown, negative pressure not only softens the Γ instability (the well-known strain-induced ferroelectricity [8]) but also increases the volume of unstable q-vectors in reciprocal space. By 0.6% strain, the instability reaches the X point and at 1.7% strain the branch is unstable and relatively dispersionless in the entire Γ-X-M plane. In fact, the $\omega^2 = 0$ isosurface at this isotropic strain value resembles that of $BaTiO_3$ [63]. We present $\omega^2 = 0$ isosurfaces for $SrTiO_3$ under tensile biaxial strain in Fig. 2.3. The tensile biaxial strain boundary condition results in two components of the polar mode soften whereas the third

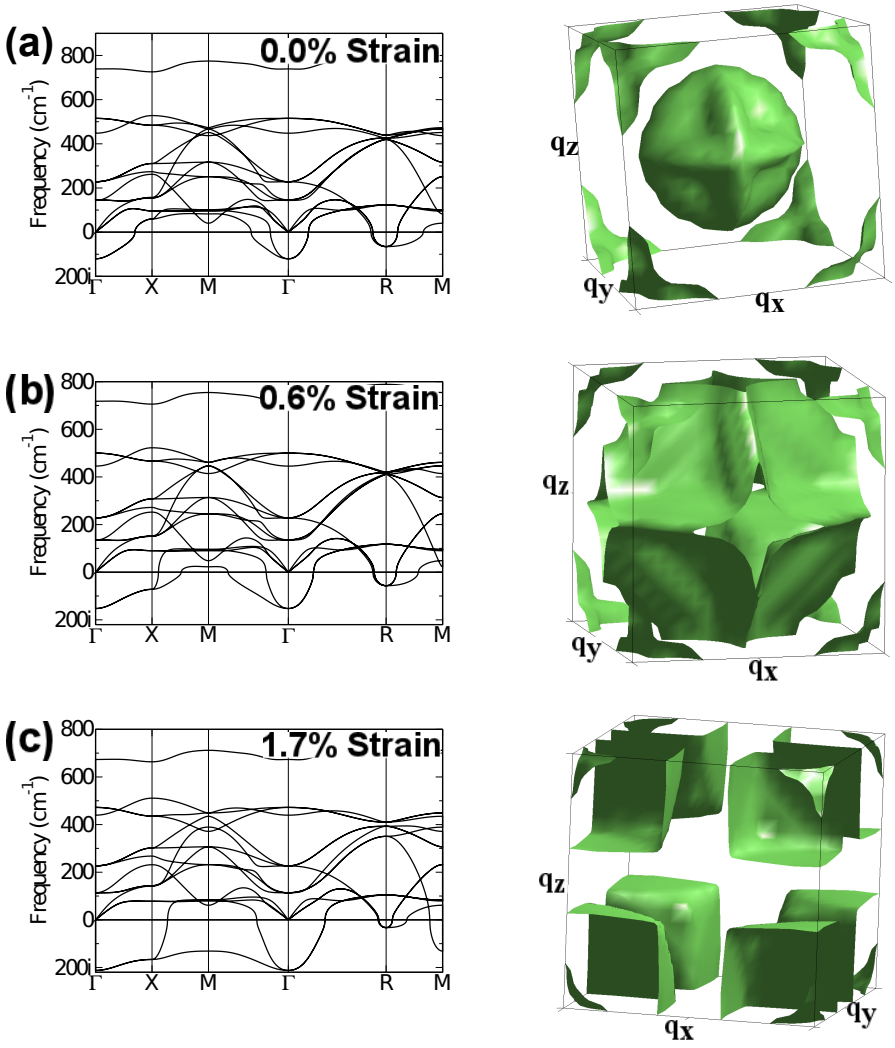

Figure 2.2: Phonon dispersions of $SrTiO_3$ in its cubic ($Pm\bar{3}m$) phase at (a) experimental volume, and under (b) 0.6 % and (c) 1.7 % isotropic tensile strain with respect to the experimental lattice constant. The corresponding $\omega^2 = 0$ isosurfaces are shown next to each phonon dispersion curve.

(out-of-plane) component hardens. This results in two of the three disks in the reciprocal space getting larger, while the third one shrinks.

These results suggest that under increasing biaxial, in-plane tensile strain [147] the critical thickness for in-plane ferroelectricity in $SrTiO_3$, and hence n_{crit} in the RPs, should decrease and eventually vanish. This is clearly seen for the RPs in Fig. 2.4(a). Note that at a tensile strain value of 1.1% – a strain more than sufficient to drive $SrTiO_3$ ferroelectric – the perpendicular coherence length ($l_\perp$) in $SrTiO_3$ is still non-zero. This results in the $n = 1$ RP remaining very far from displaying a polar instability. It isn't until a strain of ~1.4% that $l_\perp \approx 0$ and the $n = 1$ structure develops a polar instability.

As further proof of a crossover from 2d to 3d ferroelectric behavior (and the direct strain control thereof), we parameterize from first-principles a finite thick, infinite perovskite slab force constant model for which we add additional layers of SrO and TiO_2 planes. (For details, see Section 2.8.2.) The softest force constant eigenvalue is plotted in Fig. 2.4b for different strain values as the number of $SrTiO_3$ layers, m, is increased. Notice that the in-plane polar force constant in this 2d model slab (Fig. 2.4b) is evolving with both thickness and strain exactly like the in-plane polar instabilities in the structurally 3d RPs (Fig. 2.4a). This is clear evidence of the proposed coherence physics and the direct control of with strain. (A similar calculation for unstrained $BaTiO_3$, which has a $l_\perp \approx 0$, shows that a single TiO_2 layer in bulk $BaTiO_3$ is unstable.)

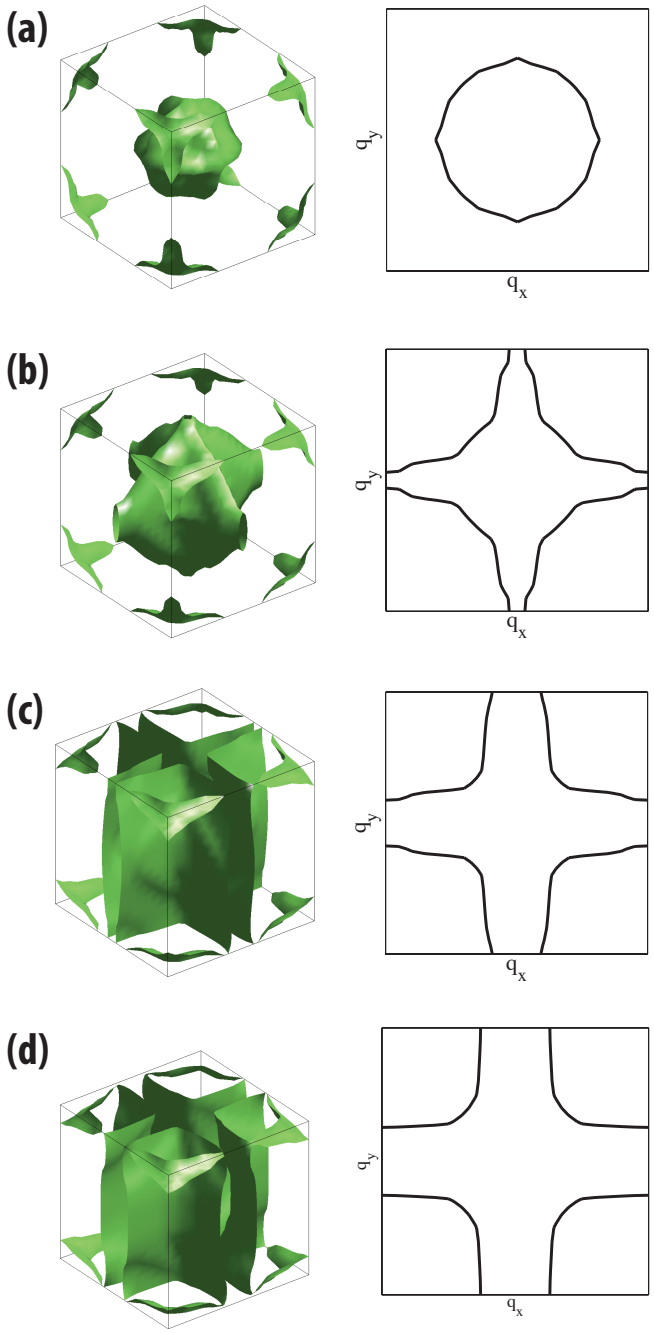

Figure 2.3: The $\omega^2 = 0$ isosurfaces for $SrTiO_3$ under (a) 0.0%, (b) 0.5%, (c) 1.1%, and (d) 1.7% biaxial strain. Right panels show the cuts of the isosurfaces on $k_z = 0$ planes. For (c) and (d), the slight anisotropy on the surfaces of $DyScO_3$ and $GdScO_3$ substrates are taken into account, however, this anisotropy gives barely visible results.

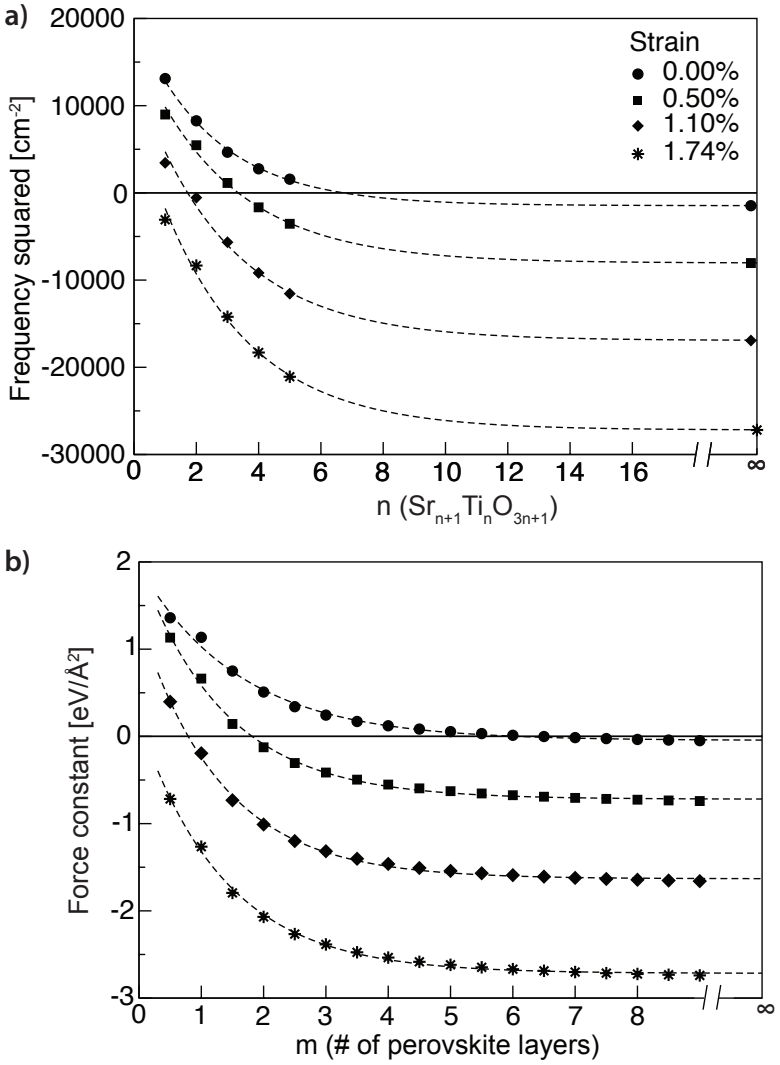

Figure 2.4: (a) **Ruddlesden-Popper**, $(SrTiO_3)_n(SrO)$: In-plane polar soft mode frequency squared versus layering number n. (b) **Perovskite Slab Model**, $(SrTiO_3)_m$: Lowest in-plane polar interplanar force constant matrix eigenvalue versus thickness of $SrTiO_3$. Strain values are given with respect to the lattice constant of $SrTiO_3$. The slab thickness in panel b, given in number of $SrTiO_3$ layers, corresponds to half the number of atomic SrO or TiO_2 layers in the slab. Half integer values correspond to an odd number of atomic layers that are terminated by TiO_2 layers o both sides. Similar calculations for slabs terminated by SrO layers, not presented here, give qualitatively similar results even though the force constants are higher for small thicknesses. The lines are fits to exponentials.

2.6 The Effect of Rumpling

These results suggest that the rocksalt layer in $Sr_{n+1}Ti_nO_{3n+1}$ breaks the coherence between perovskite blocks. Why and how? Note that rumpling of the SrO layers is permitted by symmetry in paraelectric RPs and that the distance along the [001] direction between the Sr and O ions within the rocksalt layer can be as large as 0.20 Å [51] and quickly gets smaller in the layers further away, Fig. 2.5(b). In RPs with $n > n_{\text{crit}}$, the in-plane polar displacements of Ti along the infinite Ti-O-Ti chains get smaller the closer the chain is to the rocksalt layer. We propose that the rumpling at the double SrO layers breaks the coherence between perovskite slabs.

To test this hypothesis, we artificially zero the rumpling by moving the Sr and Ti atoms to exactly the same plane as the oxygens, and repeat the phonon calculations. We find that even the $n = 1$ Sr_2TiO_4 under zero strain has an in-plane polar instability and it is in fact almost equal in magnitude to that of $SrTiO_3$, that is, the decay of the phonon frequency with n disappears [1].

2.7 A Novel Polar State

What are the implications of our findings? We propose that strained RPs, which lack coherence across the rocksalt layers, can not be ferroelectric, but rather display a novel polar state. In Fig. 2.5c we plot the energy versus mode amplitude in, e.g., $Sr_4Ti_3O_7$ ($n = 3$) for both the ferroelectric mode and an antiferroelectric distortion involving polar distortions of neighboring perovskite slabs antipar-

[1] Note that strain has little influence on the amount of rumpling; rumpling does not differ by more than ~ 15% in structures under different values of strain or with different n.

allel to each other (Fig. 2.5a shows a comparison of these modes). Notice that the energy surfaces for these distortions are degenerate up to the precision of this plot. In Fig. 2.5d we plot the results of a similar calculation except that the rumpling was artificially zeroed; without rumpling, the degeneracy of the AFE and FE modes is lifted. These calculations (we found similar results for n = 1, 2 and 3 at two different values of strain) prove that the RP fault indeed breaks the coherence between perovskite slabs, resulting not only in a suppression of polar distortions for $n < n_{\text{crit}}$, but also for $n > n_{\text{crit}}$ polar distortions in neigboring perovskite slabs do not interact with each other significantly even at higher than quadratic order. All of this suggests that there are an infinite number of degenerate states involving uncorrelated atomic-scale polar regions. We surmise that the ground state may be a form of relaxor ferroelectricity without disorder, the consequences of which remain unclear.

2.8 Auxiliary Material

In this section, we provide some details of the arguments and calculations that are used in preceding sections. In Section 2.8.1, we explain how to obtain a crude estimate of the critical thickness from bulk phonon dispersions. In Section 2.8.2, we explain the details of the toy model that makes use of the Interplanar Force Constants. Finally, in Section 2.8.3, we calculate the energy gain with respect to the paraelectric state in the polar state and estimate the critical n that a polar distortion can experimentally be observed in.

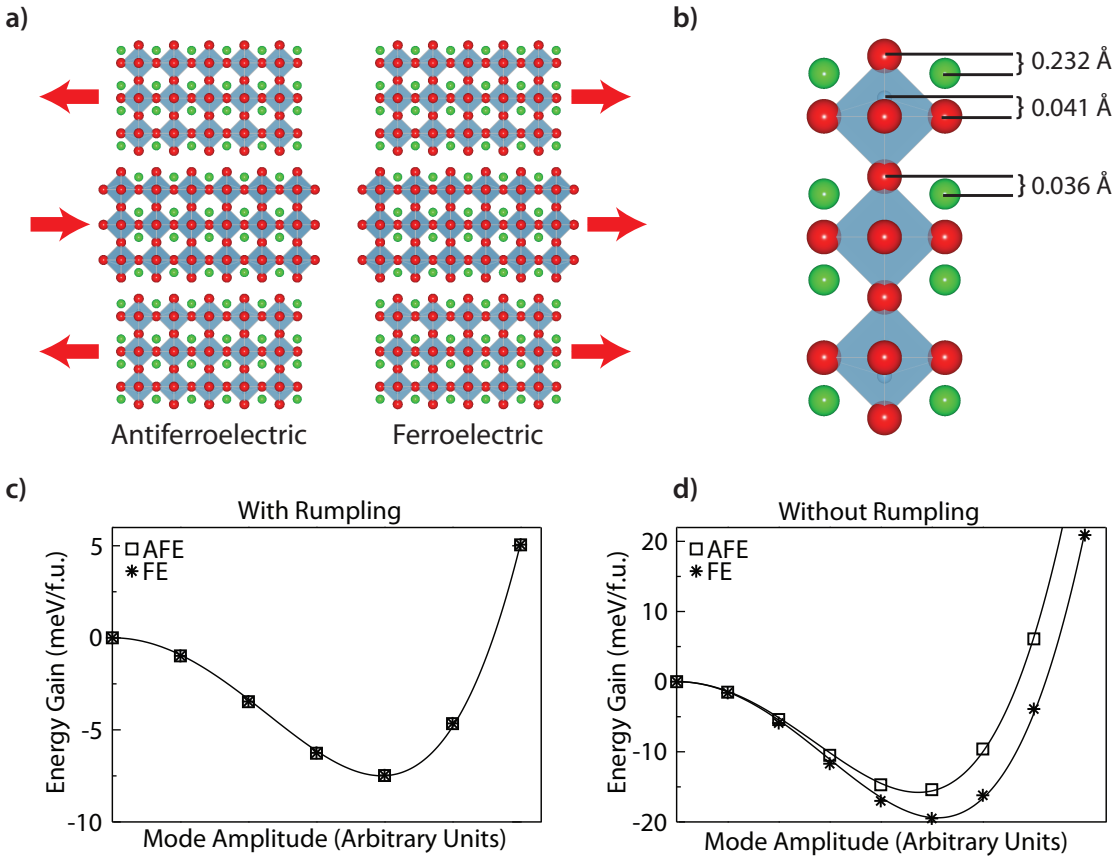

Figure 2.5: $Sr_4Ti_3O_{10}$ ground state under 1.1% tensile strain. (a) Schematic of ferroelectric (FE) and antiferroelectric (AFE) distortions. (b) Rumpling distortion (defined as the distance along [001] between cations and oxygens on the same layer). (c) Energy gain due to FE and AFE distortions in structures with rumpling. (d) The same as (c) except the rumpling distortion has been artificially set to zero.

2.8.1 Perpendicular Coherence Length

It is possible to obtain information about the perpendicular coherence properties of a ferroelectric instability from the phonon dispersions of the high symmetry (paraelectric) structure. Let us consider a cubic structure with $\hat{x}$, $\hat{y}$ and $\hat{z}$ axes aligned with the (100) directions, and focus on the $\hat{z}$ component of polarization only. Fig. 2.6 includes the sketch of distortion patterns corresponding to vari-

ous wave vectors with $q_z = 0$. The argument for $BaTiO_3$ [1] or $KNbO_3$ [2] is the following: As the unstable branch is dispersionless in the whole Γ - X - M plane, all of the distortion patterns in Fig. 2.6 are equally unstable. (See Fig. 2.7 for the labels of high symmetry points.) This indicates that whether a mode on the polar branch is unstable or not does not depend on the variation of displacement pattern in the direction perpendicular to the polarization, and so a one unit cell thick chain of atoms is unstable by itself – even if all the atoms in the rest of the crystal are fixed in their high symmetry positions. (One can imagine taking a superposition of phonon modes with different wave vectors to obtain a distortion pattern where only ions on such a thin chain are displaced.) Hence, the perpendicular coherence lengths for $BaTiO_3$ and $KNbO_3$ are zero. In other words, in a $BaTiO_3$ or $KNbO_3$ crystal in its high symmetry paraelectric phase, a coherent displacement of atoms that form a single unit cell thick chain can reduce energy.

The situation is different for (unstrained) $SrTiO_3$. Referring to Fig. 2.2a, while there is a Γ point instability with local polar atomic displacements as shown in Fig. 2.6(a), the branch stemming from this instability is stable at the X (Fig. 2.6(c)) and M (Fig. 2.6(e)) points. Therefore the polar instability is localized around the Γ-point in the q-space, stiffening as one transverses about halfway along Γ - X (Fig. 2.6(b)) and also along Γ - M (Fig. 2.6(d)) points. This indicates that the frequency of the polar branch is *not* independent of the perpendicular component of the wave vector. A superposition of modes over this restricted volume of unstable phonon modes results in a finite thickness of the Ti-O-Ti chains. The minimum thickness of this unstable distortion is inversely proportional to the radius of the disks in figure 2a of main text ($q_\perp$ in Fig. 2.8), as this radius sets the number of unstable phonon modes that can be superposed

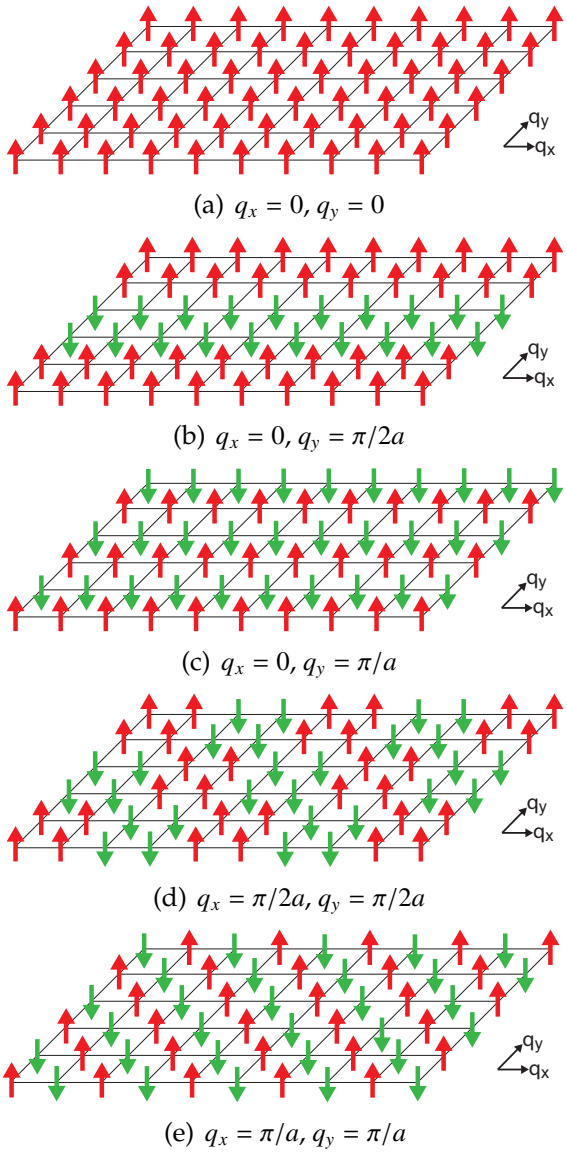

Figure 2.6: Displacement patterns for the branch stemming from the FE mode for various wave vectors. Each arrow represents the local polarization direction (direction which the cations are displaced) of a single primitive unit cell.

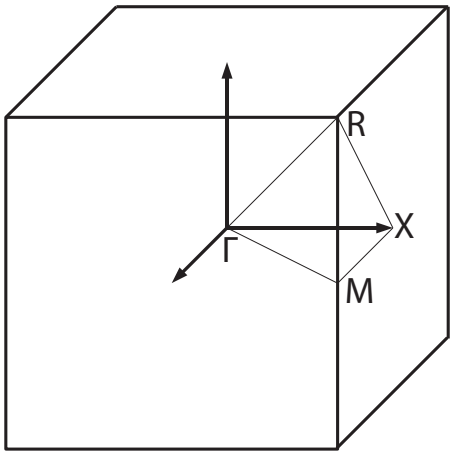

Figure 2.7: First Brillouin zone for bulk $SrTiO_3$ in space group $Pm\bar{3}m$.

to obtain a localized distortion. (The shortest wavelength of an unstable mode with $q_z = 0$ is $\sim 1/q_\perp$.) Hence for unstrained $SrTiO_3$ to display a polar instability, a critical thickness of unit cells in a direction perpendicular to the polarization direction, must be achieved.

Note, however, that this thickness scale obtained from the reciprocal space picture of the instability is a lower limit to the critical thickness, as the reciprocal space unstable disks are not perfectly flat, and that the relevant phonon branch is not perfectly dispersionless.

2.8.2 Interplanar Force Constants

In this Section we parameterize from first-principles a perovskite slab force constant model (finite thickness along out-of-plane direction [001], infinite along in-plane directions [100] and [010]) for which we add additional layers of SrO and TiO_2 planes along [001] and calculate the critical thickness for $SrTiO_3$ to

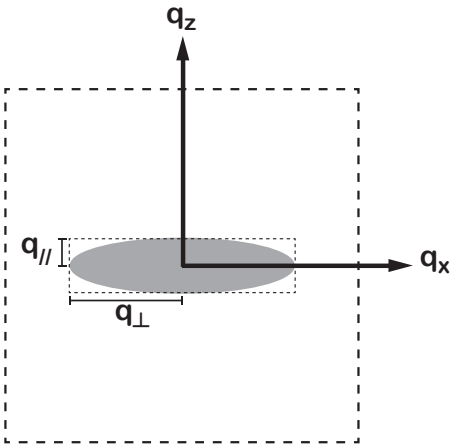

Figure 2.8: Projection of one of the disks in Figure 2a of main text on the q_x–q_z plane.

display a polar instability along an in-plane direction.

The energy of a crystal can be expanded, in terms of atomic displacements with respect to the high symmetry positions of ions, up to quadratic order, as

$$E = E_0 + \sum_{\kappa,\kappa'} \sum_{\alpha,\alpha'} \sum_{\vec{R},\vec{R}'} C^{\alpha\alpha'}_{\kappa\kappa'}(\vec{R},\vec{R}')\Delta u^{\alpha}_{\kappa}(\vec{R})\Delta u^{\alpha'}_{\kappa'}(\vec{R}') \tag{2.1}$$

Here, $\Delta u^{\alpha}_{\kappa}(\vec{R})$ is the displacement of the κ^{th} atom in the unit cell designated by the Bravais lattice vector $\vec{R}$, in the α^{th} direction, and $C^{\alpha\alpha'}_{\kappa\kappa'}(\vec{R},\vec{R}')$ are the interatomic force constants (IFC). In general, $\vec{R} = n_1\vec{a}_1 + n_2\vec{a}_2 + n_3\vec{a}_3$ where $\vec{a}_i$ are the primitive lattice vectors and n_i are integers. For a simple tetragonal system $\vec{a}_1 \perp \vec{a}_2 \perp \vec{a}_3$. In order to be specific, let $\vec{a}_3$ be along [001], which is the out-of-plane direction. We consider in-plane distortions only, $\Delta u^3_{\kappa}(\vec{R}) = 0$, The high symmetry structures we consider have 4-fold rotational symmetry so we can assume $\Delta u^2_{\kappa}(\vec{R}) = 0$ without loss of generality. From now on we drop the superscript, so $\Delta u^1_{\kappa}(\vec{R}) = \Delta u_{\kappa}(\vec{R})$.

We next impose in-plane translational invariance: The displacement of an ion in the unit cell $\vec{R} = n_1\vec{a}_1 + n_2\vec{a}_2 + n_3\vec{a}_3$ does not depend on n_1 or n_2, but only

on n_3. That is:

$$\Delta u_\kappa(\vec{R} = n_1\vec{a}_1 + n_2\vec{a}_2 + n_3\vec{a}_3) = \Delta u_\kappa(n_3) \tag{2.2}$$

The energy can now be expressed as

$$E = E_0 + N \sum_{\kappa,\kappa'} \sum_{n_3,n_3'} C_{\kappa\kappa'}(n_3, n_3')\Delta u_\kappa^1(n_3)\Delta u_{\kappa'}^1(n_3') \tag{2.3}$$

where N is the number of unit cells in a layer, and $C_{\kappa\kappa'}(n_3, n_3')$ is the *interplanar force constant per atom* (IPFC for short). $C_{\kappa\kappa'}(n_3, n_3')$ is related to the force on an ion when a whole layer of ions are displaced, and it is intensive in the thermodynamic limit.

The matrix of IPFCs can be calculated using the direct method. For this purpose we built a $1 \times 1 \times 6$ supercell of $SrTiO_3$ (Fig. 2.9a) extended in the [001] direction. In order to get all the necessary IPFCs; 5 different displacements need to be considered: 1 for Sr (Fig. 2.9b), 1 for Ti (Fig. 2.9c) and 3 for O's (Fig. 2.9d). For each of these, we did a DFT calculation and obtained a column in the table of IPFCs, presented in Table 2.1 for unstrained $SrTiO_3$.

Next step is to build the IPFC matrices for a certain number of layers; and diagonalize them to obtain the lowest force constant eigenvalue. Size of the IPFC matrix of a slab is determined by the number of atoms in unit area (one perovskite unit cell). For instance, the IPFC matrix corresponding to slab that consists of a single TiO_2 layer is 3×3:

$$C_{(1)} = \begin{pmatrix} 2.617 & -0.190 & 0.304 \\ -0.190 & 12.285 & -5.453 \\ 0.304 & -5.453 & 4.115 \end{pmatrix} \tag{2.4}$$

Here the first column corresponds to the displacement of Ti ion, and the other two columns correspond to the displacements of the two O ions on the same

layer. (All the components are given in units of eV/Å^2.) A two-layer slab, which consists of a TiO_2 layer and a neighboring SrO layer, has a 5×5 IPFC matrix

$$C_{(2)} = \begin{pmatrix} 2.617 & -0.190 & 0.304 & -1.491 & 0.119 \\ -0.190 & 12.285 & -5.453 & -0.582 & -2.672 \\ 0.304 & -5.453 & 4.115 & 0.146 & 0.445 \\ -1.491 & -0.582 & 0.146 & 3.483 & 0.371 \\ 0.119 & -2.672 & 0.445 & 0.371 & 4.824 \end{pmatrix} \tag{2.5}$$

where the last two columns are for displacements of Sr and the O on the same layer. The smallest eigenvalues of these two matrices are 1.36 eV/Å^2 and 1.13 eV/Å^2 respectively. These values give the first two data points for 0.0% strain curve in Fig. 3b of the main text.

Both $C_{(1)}$ and $C_{(2)}$ involve force constants between ions only on the same or neighboring atomic layers, in other words, in the same perovskite layer. (One perovskite layer is two atomic layers.) So, they can be obtained solely from the '0$^{\text{th}}$ layer' row in Table 2.1. The IPFC for a 3 atomic layer (TiO_2 – SrO – TiO_2) slab, on the other hand, involves force constants between different TiO_2 layers as well:

$$C_{(3)} = \begin{pmatrix} 2.617 & -0.190 & 0.304 & -1.491 & 0.119 & -0.025 & 0.067 & -0.009 \\ -0.190 & 12.285 & -5.453 & -0.582 & -2.672 & 0.067 & -0.126 & 0.006 \\ 0.304 & -5.453 & 4.115 & 0.146 & 0.445 & -0.009 & 0.006 & -0.090 \\ -1.491 & -0.582 & 0.146 & 3.483 & 0.371 & -1.491 & -0.582 & 0.146 \\ 0.119 & -2.672 & 0.445 & 0.371 & 4.824 & 0.119 & -2.672 & 0.445 \\ -0.025 & 0.067 & -0.009 & -1.491 & 0.119 & 2.617 & -0.190 & 0.304 \\ 0.067 & -0.126 & 0.006 & -0.582 & -2.672 & -0.190 & 12.285 & -5.453 \\ -0.009 & 0.006 & -0.090 & 0.146 & 0.445 & 0.304 & -5.453 & 4.115 \end{pmatrix} \tag{2.6}$$

The last three columns/rows of this matrix are for the atoms on the second TiO_2 layer, the corresponding off diagonal elements are taken from the '1st layer' row in Table 2.1. Similarly, the 4 layer slab has two more column/rows:

$$C_{(4)} = \begin{pmatrix}
2.617 & -0.190 & 0.304 & -1.491 & 0.119 & -0.025 & 0.067 & -0.009 & 0.000 & 0.022 \\
-0.190 & 12.285 & -5.453 & -0.582 & -2.672 & 0.067 & -0.126 & 0.006 & -0.001 & -0.045 \\
0.304 & -5.453 & 4.115 & 0.146 & 0.445 & -0.009 & 0.006 & -0.090 & 0.002 & 0.007 \\
-1.491 & -0.582 & 0.146 & 3.483 & 0.371 & -1.491 & -0.582 & 0.146 & 0.036 & -0.037 \\
0.119 & -2.672 & 0.445 & 0.371 & 4.824 & 0.119 & -2.672 & 0.445 & -0.037 & -0.427 \\
-0.025 & 0.067 & -0.009 & -1.491 & 0.119 & 2.617 & -0.190 & 0.304 & -1.491 & 0.119 \\
0.067 & -0.126 & 0.006 & -0.582 & -2.672 & -0.190 & 12.285 & -5.453 & -0.582 & -2.672 \\
-0.009 & 0.006 & -0.090 & 0.146 & 0.445 & 0.304 & -5.453 & 4.115 & 0.146 & 0.445 \\
0.000 & -0.001 & 0.002 & 0.036 & -0.037 & -1.491 & -0.582 & 0.146 & 3.483 & 0.371 \\
0.022 & -0.045 & 0.007 & -0.037 & -0.427 & 0.119 & -2.672 & 0.445 & 0.371 & 4.824
\end{pmatrix} \tag{2.7}$$

Note that the diagonal components, which correspond to the self force constants, repeat, while the off diagonal components involve IPFCs from lower rows of Table 2.1. This way, by using Table 2.1, it is possible to build the IPFC for a slab of arbitrary number of layers and obtain the other data points in Fig. 3b of the main text.

Finally, this whole procedure should be repeated to obtain the IPFCs and the eigenvalues corresponding to different strain states, and hence the other curves in Fig. 3b of the main text.

2.8.3 Transition Temperature Estimate

Fluctuations, both quantum [3] and thermal, are absence in DFT, so the presence of a ferroelectric instability does not necessarily imply that the ground state is ferroelectric, even in the absence of other competing lattice instabilities. In order

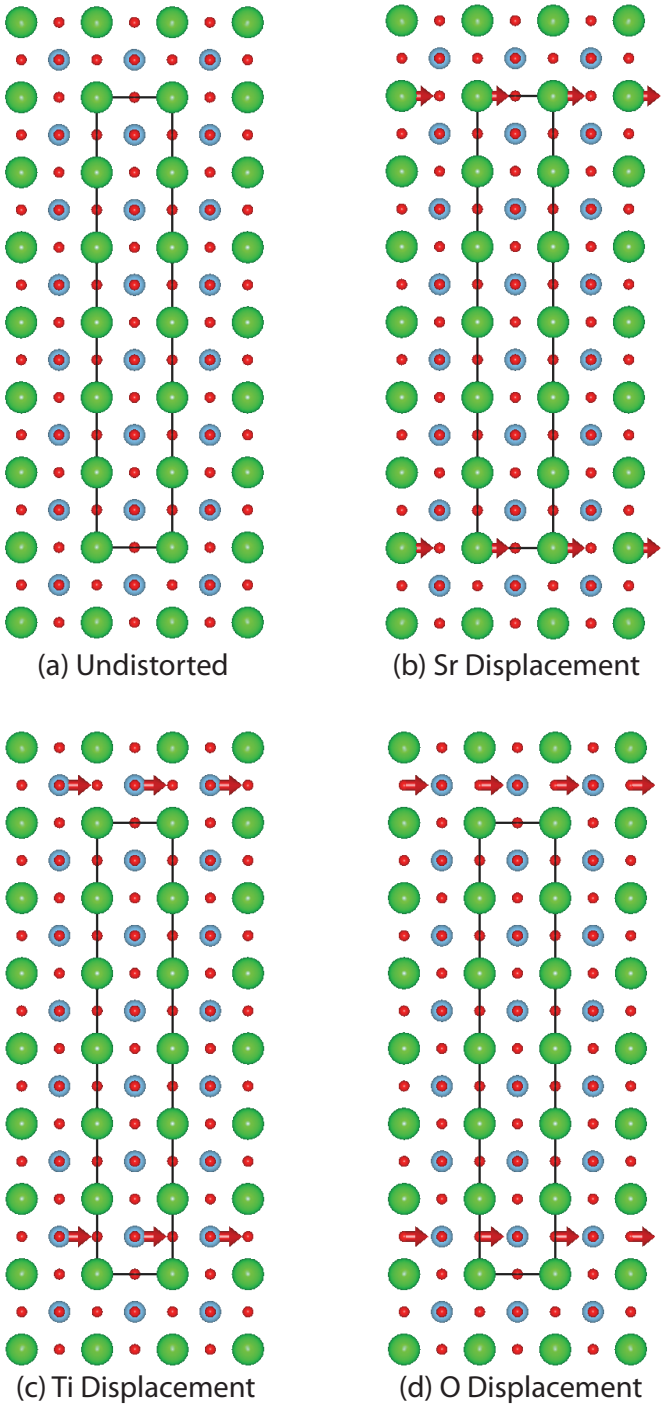

Figure 2.9: The $1 \times 1 \times 6$ perovskite supercell and 3 of the 5 inequivalent displacements used to calculate the IPFCs. Green spheres correspond to Sr ions, blue ones to Ti ions, and red ones to O ions.

		Ti	$O_{Ti\parallel}$	$O_{Ti\perp}$	Sr	O_{Sr}
0^{th} layer	Ti	2.617	-0.190	0.304	-1.491	0.119
	$O_{Ti\parallel}$	-0.190	12.285	-5.453	-0.582	-2.672
	$O_{Ti\perp}$	0.304	-5.453	4.115	0.146	0.445
	Sr	-1.491	-0.582	0.146	3.483	0.371
	O_{Sr}	0.119	-2.672	0.445	0.371	4.824
1^{st} layer	Ti	-0.025	0.067	-0.009	0.000	0.022
	$O_{Ti\parallel}$	0.067	-0.126	0.006	-0.001	-0.045
	$O_{Ti\perp}$	-0.009	0.006	-0.090	0.002	0.007
	Sr	0.000	-0.001	0.002	0.036	-0.037
	O_{Sr}	0.022	-0.045	0.007	-0.037	-0.427
2^{nd} layer	Ti	-0.005	0.005	-0.001	0.001	0.003
	$O_{Ti\parallel}$	0.005	-0.005	0.001	0.001	-0.003
	$O_{Ti\perp}$	-0.001	0.001	-0.001	0.001	0.000
	Sr	0.001	0.001	0.001	0.000	-0.001
	O_{Sr}	0.003	-0.003	0.000	-0.001	-0.019
3^{rd} layer	Ti	-0.001	0.001	-0.001	—	—
	$O_{Ti\parallel}$	0.001	0.000	0.001	—	—
	$O_{Ti\perp}$	-0.001	0.001	0.000	—	—
	Sr	—	—	—	0.001	0.000
	O_{Sr}	—	—	—	0.000	-0.003

Table 2.1: Interplanar force constants for the unstrained structure, in units of $eV/Å^2$/ion. Columns denote the ion that is moved, rows denote the ion that the force acts on. Layers are listed in increasing distance from the displaced ion, and due to the finite size of the supercell, force constants for atomic layers as far as 3 unit cells are calculated. Subscripts for O's denote whether they are on a TiO_2 or an SrO plane, and $O_{Ti\parallel}$ denotes the force on the oxygen on the Ti–O chain parallel to the displacement direction, $O_{Ti\perp}$ denotes the other oxygen on the TiO_2 layer. The force constants presented are symmetrized. This process ensures that all the $C_{(n)}$ matrices are perfectly symmetric (the symmetrization changed the lowest eigenvalues no more than $\sim 1\%$).

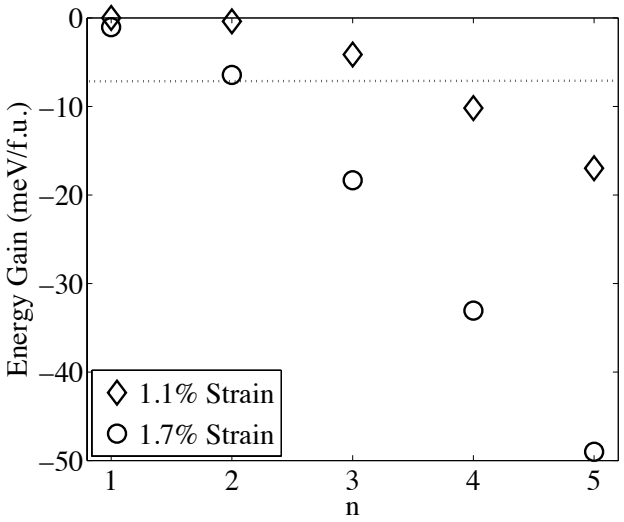

Figure 2.10: Energy gain, per formula unit, of the ferroelectric mode for $n = 1$ to $n = 5$ RP phases under different strain states. The horizontal dotted line corresponds to the energy gain per formula unit of $SrTiO_3$ under 1.1% tensile biaxial strain.

to obtain a crude estimate of transition temperatures, we present in Fig. 2.10 the energy gain of the FE state with respect to the PE state, as a function of n, calculated from first principles.

Note that the energy gain for unstrained bulk $SrTiO_3$ is ~ 0.4 meV/f.u., and so we assume that quantum fluctuations are more than enough to suppress an instability with this energy scale. This value is comparable to that of $n = 1$ under 1.7 % strain and $n = 2$ under 1.1 % strain. We therefore expect RPs with $n < 2$ and $n < 3$ not to distort in an experiment under 1.7 % strain and 1.1 % strain respectively.

Another point of comparison is the energy gain calculated from first-principles, ~ 8 meV/f.u., for 1.1% strained $SrTiO_3$, which is ferroelectric at room temperature experimentally [4]. This is shown as the dotted line in Fig. 2.10. RPs with comparable energy gains, such as $n \geq 4$ under 1.1% strain or $n \geq 2$

under 1.7 % strain are expected to undergo transitions on the order of room temperature.

2.9 Comparison to Experiments

High quality films of Sr-Ti-O RP compounds have been grown using molecular beam epitaxy by Lee et al. [100, 164]. In this section, we briefly compare our results with the relevant experimental measurements. For other experimental observations, such as the measurement of the highest dielectric figure of merit measured so far, can be found in the original papers [100, 164, 121].

In Fig. 2.11, the results of dielectric measurements of Lee et al. are presented. In Fig. 2.11a, we plot the in-plane dielectric constant as a function of temperature. A peak in the dielectric constant of $n = 3-6$ compounds under 1.1% tensile strain shows the emergence of a polar instability in these compounds. $n = 2$ compound $Sr_3Ti_2O_7$, on the other hand, has no dielectric peak, which is consistent with our expectation that the polar instability in this compound is weak enough to be suppressed by quantum fluctuations of the nuclei. The positions of the peaks have a frequency dependence, which hints to a relaxor behavior. This could be a signature of the novel polar state that we predict.

In Fig. 2.11b, the critical temperature T_c where the polar instability emerges is plotted for films on $DyScO_3$ and $GdScO_3$ substrates, which provide $\sim$ 1.1% and $\sim$ 1.7% tensile strain. In line with the theoretical predictions, which indicates that energy gain of the polar distortion is larger for larger n as well as larger tensile strain, T_c increases with increasing n and increasing strain.

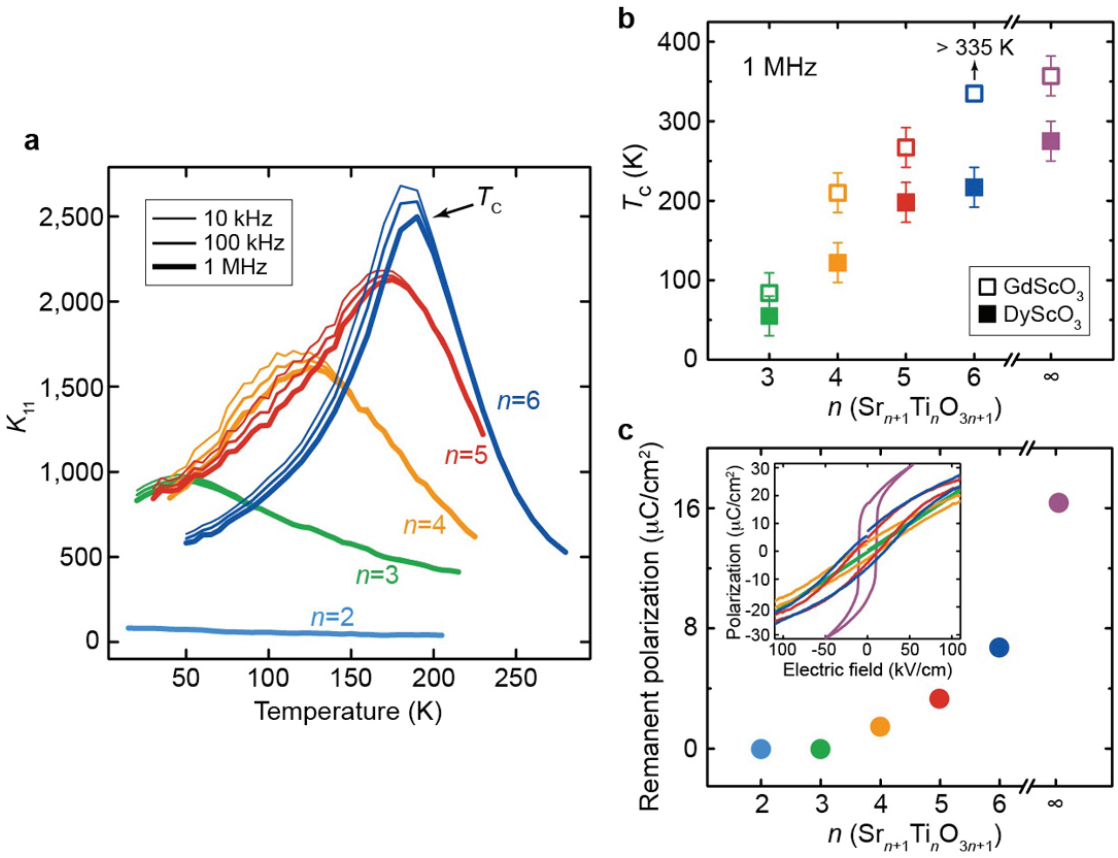

Figure 2.11: Experimental results for dielectric properties of Sr-Ti-O RP compounds. (a) Real part of the in-plane dielectric constant of films deposited on $DyScO_3$ substrate, as a function of temperature at different frequencies. (b) Critical temperature T_c of the films deposited on $DyScO_3$ and $GdScO_3$ substrates. T_c is calculated from the position of the dielectric constant peak at 1 MHz. Error bars give a measure of the variation of T_c in separately grown samples. (d) Remanent polarization at 10 K of the films on $DyScO_3$. Inset: Polarization hysteresis loops at the same temperature. (Figure reproduced from [100].)

In Fig. 2.12, we plot the energy per perovskite slab (per n) of the Sr-Ti-O RP compounds as a function of polar displacement amplitude in the (001) plane, from first-principles. The displacement pattern for the $n = 1$ compound is obtained from the force constants matrix eigenvector. For $n > 1$ compounds, the difference of the groundstate structure with that of the high symmetry paraelectric structure is used as the polar distortion pattern. For all compounds, the minimum energy is obtained with polarization along $\langle 110 \rangle$ directions, and the total ionic displacement that gives the minimum energy increases with n. Since this quantity is roughly proportional to the ground state polarization, we conclude that the polarization monotonically increases with increasing n. This supports the experimental observation that the remanent polarization, presented in Fig. 2.11c increases with increasing n.

2.10 Summary

In this chapter, we presented a first-principles study on the ferroelectricity in $Sr_{n+1}Ti_nO_{3n+1}$ RP compounds. Our linear response calculations show that a ferroelectric instability emerges in these compounds with increasing tensile biaxial strain, as well as increasing stacking parameter n. Both of these observations can be explained by the concept of a critical thickness and its evolution under strain. We supported this point by providing a toy model that involves the force constants of bulk $SrTiO_3$. We further argued that the groundstate of $Sr_{n+1}Ti_nO_{3n+1}$ RP compounds under strain is not ferroelectric but rather there exists a new polar regime where the ferroelectric state is degenerate with the antiferroelectric state. We proved this point by explicit calculations and proposed that it can lead to relaxor behavior in these compounds. Our predictions and quantitative results

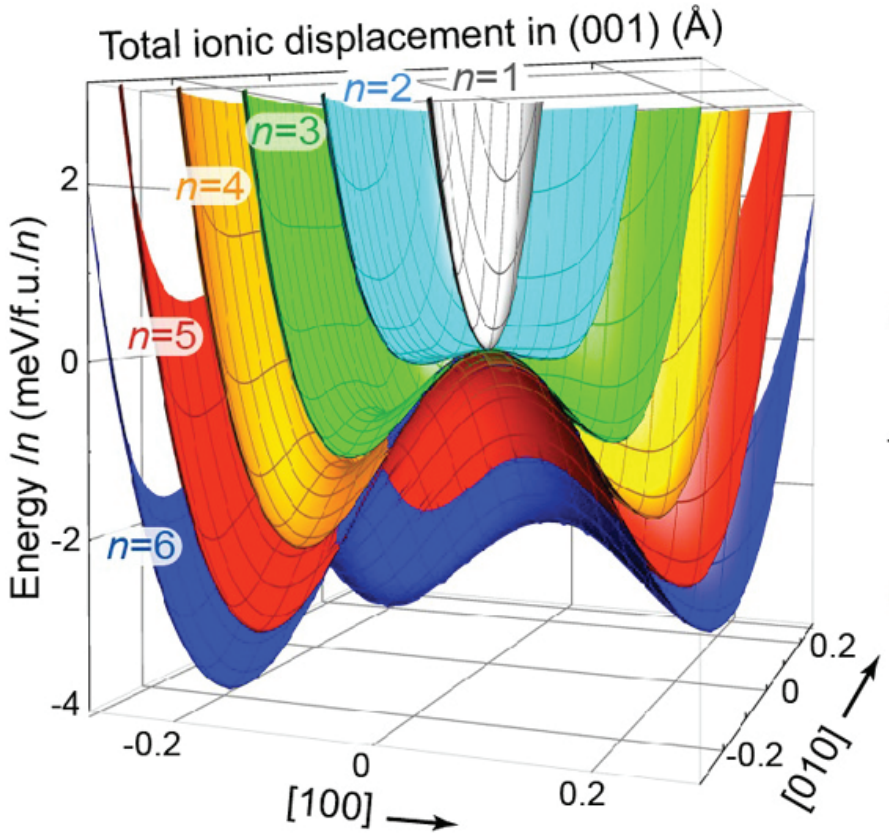

Figure 2.12: Energy (per n) of the Sr-Ti-O RP compounds as a function of polar displacement amplitude in the (001) plane. For all compounds, the minimum energy is obtained with polarization along $\langle 110 \rangle$ directions. (Figure reproduced from [100].

are in line with experiments on thin films grown by Molecular Beam Epitaxy.

This chapter provides not only a comprehensive theoretical study of the polar behavior of $Sr_{n+1}Ti_nO_{3n+1}$ RP compounds, but also a conceptually new way to look at the emergence of ferroelectricity with strain. We believe that the ideas put forth here, such as the critical thickness and its relation to the coherence volume, can be used in the context of various different systems, especially ones that involve a layered structure. Our results underline the importance of layering as a 'knob' to tune structural phase transitions as well.

CHAPTER 3

WHY $EuTiO_3$ IS NOT A FERROELECTRIC AND THE MICROSCOPIC MECHANISM OF MAGNETODIELECTRIC COUPLING

In this chapter, we present a study of the magnetoelectric perovskite $EuTiO_3$ [37]. This compound has been in the focus of intense recent research because of the strong magnetodielectric coupling (i.e. dependence of the dielectric constant on the external magnetic field) [86] and strain induced multiferroicity (i.e. transition to a ferroelectric-ferromagnetic phase under strain) [52, 102] observed in this compound. Despite a plethora of both experimental and first-principles theoretical studies on $EuTiO_3$, the microscopic mechanism that gives rise to the magnetoelectric effect in bulk $EuTiO_3$ is still unknown. This chapter is an attempt to elucidate why such a coupling exists in bulk $EuTiO_3$. In order to do so, we first ask the question why $EuTiO_3$ is not a ferroelectric (or a quantum paraelectric like $SrTiO_3$) and show that the hybridization between the occupied Eu f states and the unoccupied Ti d orbitals not only drive $EuTiO_3$ away from a ferroelectric phase transition, but is also responsible of the magnetodielectric coupling observed in this compound.

In terms of first-principles methods, in this chapter we utilize two tools that we do not use in the rest of this thesis: In order to explicitly show the hybridization and visualize it in an intuitive way, we employ Maximally Localized Wannier Functions (MLWFs) as implemented in the Wannier90 code [110, 115]. Also, we use the DFT+U method, introduced in Section 1.2.3, to not only reproduce the properties of the localized Eu f electrons correctly, but also to probe the physics of the system and in particular, change the effect of Eu-f/Ti-d hybridization.

Our results in this chapter underline the importance of f electrons of rare earth ions in the lattice dynamics and structural properties of TM oxides [158]. While we do not discuss any other materials in detail, there is no reason to consider the mechanism we identify as unique to $EuTiO_3$.

3.1 Introduction

In the last ten years there has been an intense effort to discover new materials that display strong magnetoelectric coupling. Such materials could enable novel devices in which an electric-field control magnetism [118, 108, 107, 75]. In this pursuit first-principles computational methods have played a key role by successfully predicting new material realizations [40, 56, 154, 71, 17, 31, 22, 132, 174] even when the underlying microscopic mechanisms have not always been clear. Elucidating these mechanisms is important for both fundamental understanding and also for guiding the search for new magnetoelectrics. One example is the perovskite $EuTiO_3$ [111].

Bulk $EuTiO_3$, shown in Fig. 3.1a, is a paraelectric antiferromagnet that displays a dielectric anomaly at the magnetic ordering temperature ($T_N \sim 5.3$ K) [37, 86]. Much more relevant to the possibility of magnetoelectric phase control were the pioneering experiments of Katsufuji and Takagi, which showed that $EuTiO_3$ exhibits a magnetodielectric effect; at low temperatures, the dielectric constant depends strongly on the magnitude of the external magnetic field [86]. They suggested that this effect stemmed from spin-phonon coupling, i.e., the dependence of the polar phonon frequencies on spin correlations. Subsequent first-principles studies [52, 134] and direct measurements of the phonon frequencies under magnetic field by infrared reflectrometry [84, 83] have largely

confirmed this picture.

Regarding the magnetoelectric properties of $EuTiO_3$, it was shown from first principles how the underlying physics leading to the observation of spin-phonon coupling can be exploited to enable control over the dielectric and the magnetic ground state [52]. Epitaxial strain was proposed as the explicit control 'knob' that tunes the antiferromagnetic-paraelectric ground state into a simultaneous ferromagnetic-ferroelectric phase. Furthermore it was argued that under increasing strain but before reaching this novel multiferroic phase, a giant magnetoelectric response would occur in the vicinity of the strain-induced phase transitions due to phase competition [120, 165]. Subsequent experiments on epitaxially strained thin films have observed the strain induced ferromagnetic-ferroelectric phase [102] and also the suppression of the antiferromagnetic order by an external electric field [143], both of which are consistent with the original prediction, yet the giant magnetoelectric effect has yet to be observed (possibly due to a lack of high quality substrates that would provide the necessary value of strain).

While it has been suggested that the physics of $EuTiO_3$ largely originates from a cation-mediated exchange mechanism [2, 22], the microscopic mechanism of the spin-phonon coupling, and subsequently of the magnetoelectric phase control, is unknown. Here we ask an important, but overlooked, question whose answer makes these clear; *Why isn't $EuTiO_3$ a ferroelectric in bulk*?

Before we begin discussing our results we must make it clear in what sense we are 'surprised' that $EuTiO_3$ is not ferroelectric in bulk. First, note the similarity to the perovskite $SrTiO_3$: both compounds in the cubic phase have almost identical lattice constants (to two significant figures), both have nominally Ti^{4+}

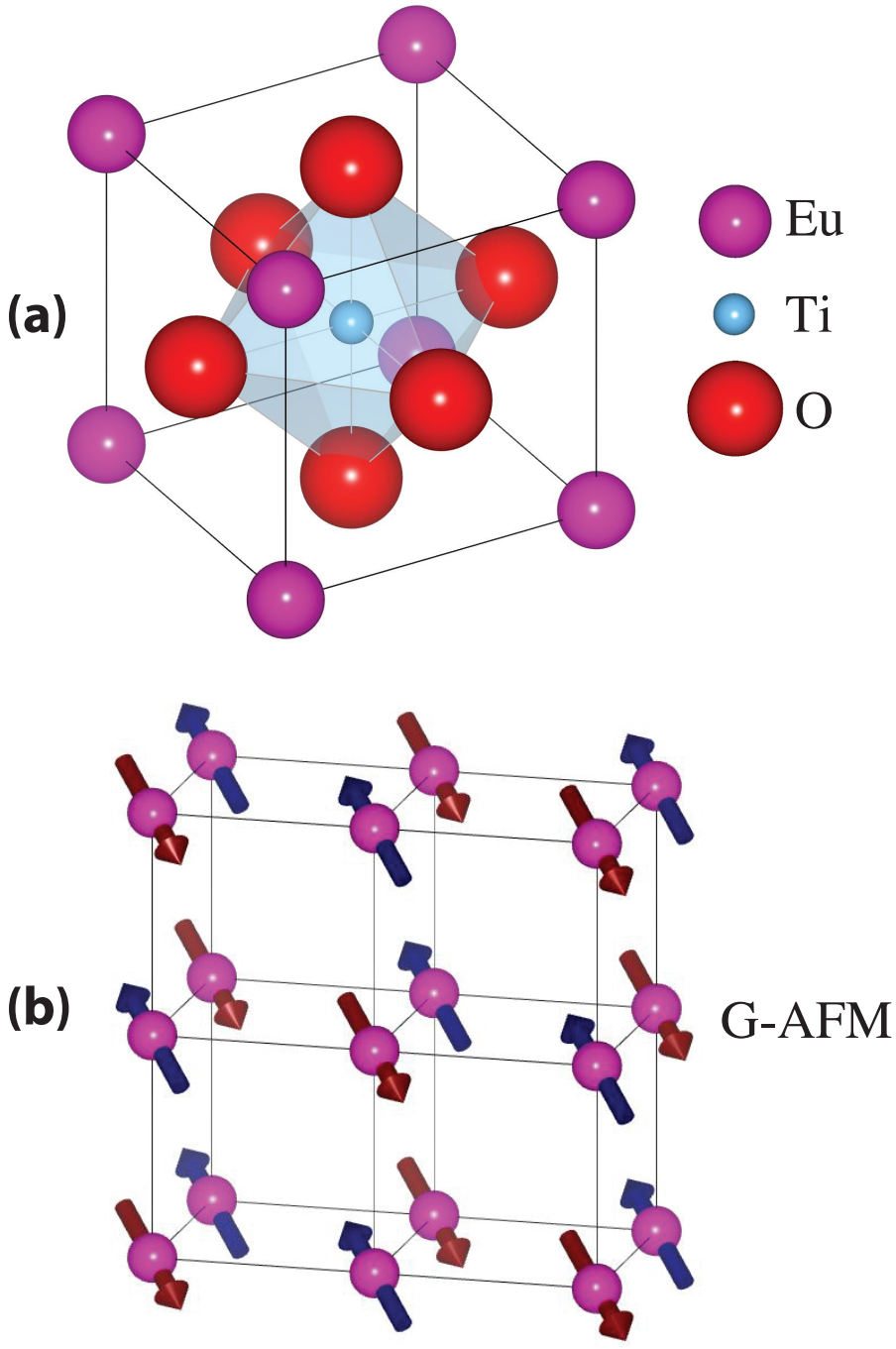

Figure 3.1: (a) Crystal structure of perovskite $EuTiO_3$ in the cubic phase. (b) Sketch of G-type antiferromagnetic order. Arrows denote the direction of spins.

in an oxygen octahedral environment, and both have an A^{2+} cation on the A-site. In fact these two perovskite compounds have very similar band structures. Both have a charge transfer gap – between filled oxygen 2p states and empty Ti d states – of similar magnitude. The only major difference is the presence of narrow Eu 4f bands in $EuTiO_3$ (Fig. 3.2a and 3.2b). These 4f electrons, however, are well localized and shielded by the 5s and 5p electrons. As a result, they are not expected to contribute significantly to chemical bonding. Because of these facts there is good reason to believe that the structural and dielectric properties of $EuTiO_3$ and $SrTiO_3$ should be quite similar.

Consistent with this conjecture is the observation that both compounds undergo a structural phase transition due to the softening of a zone-boundary, antiferrodistortive mode (corresponding to a rotation of the octahedra) [142, 102, 173]. In $EuTiO_3$, however, this occurs at a much higher temperature ($\approx$100K for $SrTiO_3$, $\approx$300K for $EuTiO_3$) [55, 4]. Even more surprising is the fact that $SrTiO_3$ displays a static dielectric constant of $\epsilon \sim 10^4$ at low temperature [117, 169]. This huge dielectric constant has been explained in a picture of a nominally unstable zone-center polar phonon mode being weakly stabilized by quantum fluctuations [176, 117], and as such, is referred to as a quantum paraelectric. Indeed, first-principles calculations of the infrared-active (polar) phonons within Density Functional Theory, DFT, have shown that at the experimental lattice constant, $SrTiO_3$ displays a weak ferroelectric instability. (All DFT studies of $SrTiO_3$ that we know of used the most common formulation of DFT, which is a static theory where fluctuations of the nuclei, quantum or thermal, are not considered). Quantum Monte Carlo studies of a first-principles parameterized effective Hamiltonian indeed show that this ferroelectric state is suppressed by quantum fluctuations [176], consistent with a picture of $SrTiO_3$ being a quantum

paraelectric.

In contrast, for $EuTiO_3$, first-principles calculations of the polar phonons within DFT at the experimental cubic lattice constant have shown that all the polar modes are quite hard, with the softest mode being $\omega \sim +70$ cm^{-1}. It is therefore hard to imagine that $EuTiO_3$ is close to a ferroelectric phase transition. Consistent with this is the fact that the low temperature ($\sim$ 5K) dielectric constant of $EuTiO_3$ is two orders of magnitude smaller, $\epsilon \sim 10^2$, than in $SrTiO_3$ [86]. While there appears to be a 'rounding off' of the dielectric constant below $\sim$ 10K in $EuTiO_3$, which people consider to be an observable effect of quantum fluctuations, we stress that $EuTiO_3$ would remain a paraelectric even in their absence. This is clear from every DFT study ever conducted [52, 142, 83], and from the experimental determination of the Cochran fit to soft-mode frequency, which gives $\omega_{SO} \sim 75$ cm^{-1} at zero temperature [84]. Because of these facts we would not refer to $EuTiO_3$ as a quantum paraelectric.

Our question should therefore be understood within the following sense: given that lattice instabilities in $A^{2+}TiO_3$ perovskites tend to be controlled by volume (baring chemistry differences, e.g., the Pb^{2+} lone-pair cation), and that $SrTiO_3$ and $EuTiO_3$ have almost identical volumes in the cubic phase, what leads to the giant hardening of the soft polar mode is $EuTiO_3$ compared with $SrTiO_3$? What seems to be the only possible explanation is that somehow the Eu 4f electrons have a giant effect on the lattice instabilities: dramatically decreasing (increasing) the tendency for $EuTiO_3$ to display a ferroelectric instability (rotational instability).

In this chapter we discuss the answer to these questions, thereby providing a microscopic picture of spin-phonon, or more accurately spin-lattice, coupling

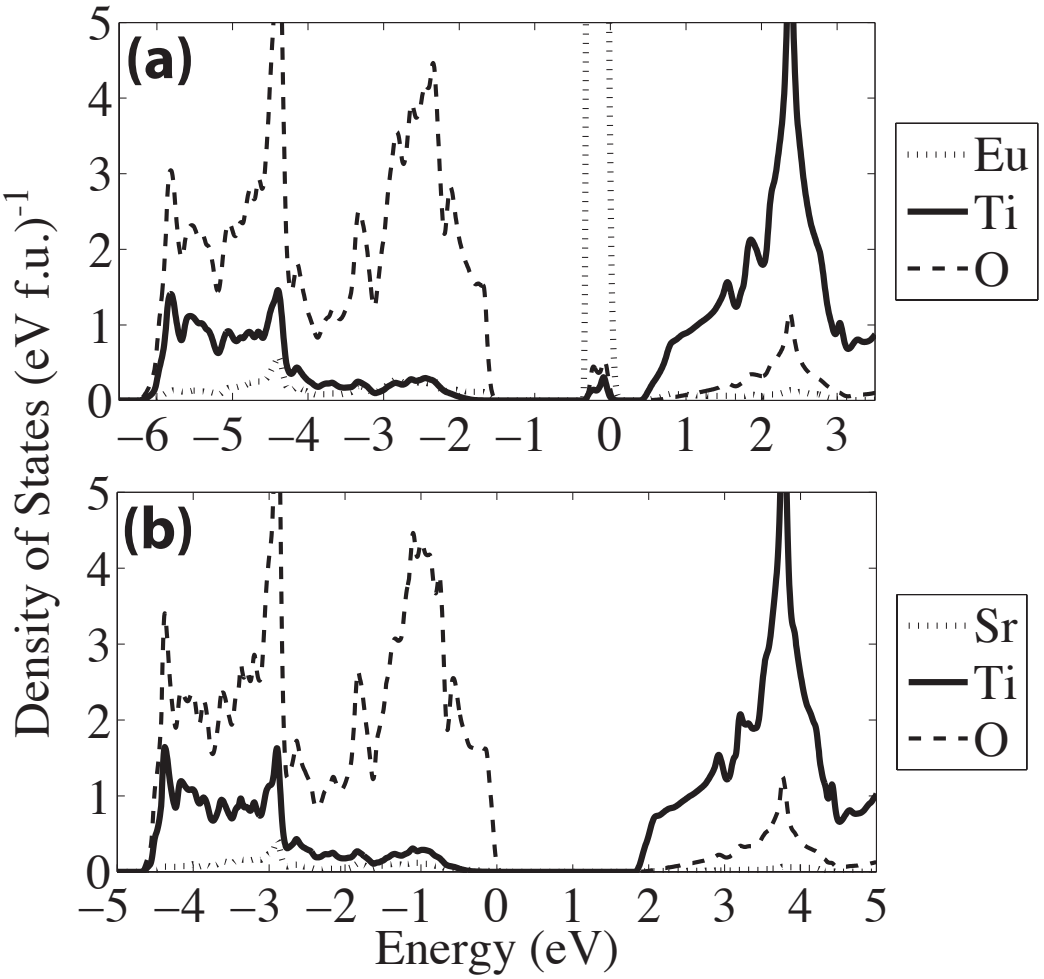

Figure 3.2: (a) Density of states (DOS) of $EuTiO_3$, calculated from first-principles. (b) DOS of $SrTiO_3$, calculated from first-principles. The zero points of energy in the DOS plots are aligned with the highest occupied level.

in $EuTiO_3$ from first principles. (Note, the physics of spin-phonon coupling that we are discussing is in actuality a spin-lattice coupling, i.e., the effect of the magnetic order/correlations on the force constants, an inherently static quantity [22].) We explain our methods in Section 3.2 and give a brief background on $EuTiO_3$ in Section 3.3.1. In Section 3.3.2, we explain the evolution of the polar soft-mode frequency under changing Hubbard-U_{Eu}. We then elucidate the

key role played by the hybridization of the filled Eu 4f states with those of the nominally empty Ti d states in Section 3.3.3 . In Section 3.3.4 we show how this leads to a giant hardening of the polar soft mode, subsequently driving $EuTiO_3$ away from ferroelectricity and rendering it a paraelectric with a small dielectric constant. In Section 3.3.5 we explore the magnetic order dependence of this hybridization and show how it is the dominant cause of spin-lattice coupling. In Section 3.3.6 we argue that the much stronger oxygen octahedral rotations in $EuTiO_3$ compared to $SrTiO_3$ also originates from the hybridization of the Eu f electrons. Finally, we conclude with a summary in Section 3.4.

3.2 Methods

First-principles calculations were performed within density functional theory using the PBE-GGA exchange-correlation functional [127] and the Projector Augmented Wave method [24, 94] as implemented in VASP [93, 92]. Because of the well-known deficiency of PBE-GGA in describing the localized nature of f-electrons of e.g., Eu, the DFT+U formalism is used [6, 103]. The on-site exchange J_{Eu} is kept fixed at 1.0 eV, while a Hubbard-U_{Eu} = 6.2 eV was found to give the best fit to experiment (where we compared the ratio of the Néel to Curie temperatures calculated within mean field theory). The value of U_{Eu}, however, is often varied in our calculations in order to probe the physics of the system, as will be described. The cubic lattice constant is kept fixed to the experimental value of a = 3.90 Å. Phonon frequencies are calculated using both Density Functional Perturbation Theory and frozen phonons technique and no discrepancy is observed. We made extensive use of the Isotropy Software Package [157] and the Bilbao Crystallographic Server [11, 10, 9, 162]. Visualization of crystal

structures are made using Vesta [113]. Maximally Localized Wannier Functions (MLWF) are calculated using the Wannier90 code [110, 115].

3.3 Results

3.3.1 Background

The cubic crystal structure of perovskite $EuTiO_3$ is shown in Fig. 3.1a. Rotations of oxygen octahedra, which are known to exist in bulk $EuTiO_3$, were recently shown to have a strong effect on magnetism [1, 3, 142, 173, 143, 65]. In particular, they alter the magnetic exchange interactions in a way that strongly favors antiferromagnetism over ferromagnetism. Additionally, rotations tend to suppress the tendency towards ferroelectricity [173, 143]. In the epitaxial strain phase diagram of $EuTiO_3$ this results in an increase in the critical strain value necessary to induce a transition form the paraelectric-antiferromagnetic phase to the ferroelectric-ferromagnetic phase. For tensile strain, however, this increase in critical strain is almost canceled by the larger value of Hubbard-U_{Eu}, which lowers the critical strain, that is now necessary to give a reasonable fit of the magnetic exchange interactions in the presence of rotations to experiment (see Ref. [143] for a complete discussion).

Magnetism in $EuTiO_3$ stems from the half filled 4f shell of the Europium cation, which have 7 electrons in a high-spin state. These well localized spins order in a collinear G-type antiferromagnetic fashion (Fig. 3.1b) so that the spin of each Eu cation is opposite to all of its nearest neighbors. As seen in the density of states (DOS) in Fig. 3.2a, there is a wide charge transfer gap between the

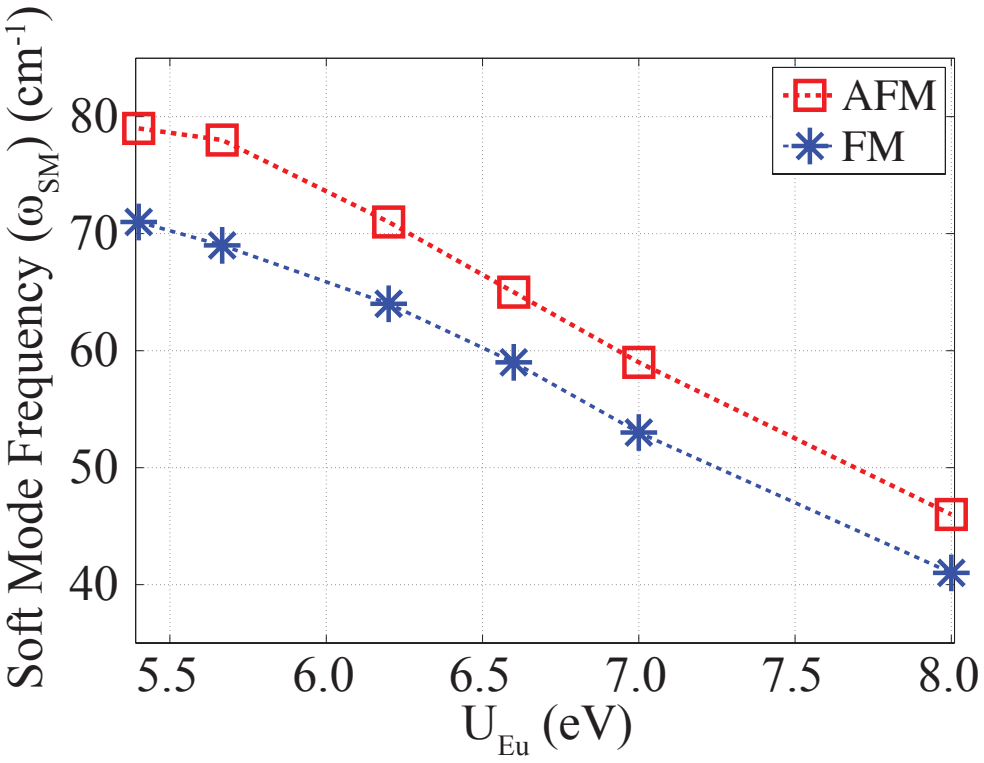

Figure 3.3: Polar soft-mode frequency, ω_{SM}, vs. the on-site interaction U_{Eu} on Eu 4f orbitals. Red squares and blue asterisks denote the frequencies calculated in AFM and FM states respectively.

the occupied O-p states and the conduction band that consists of unoccupied Ti-d states. The half-occupied Eu 4f states form narrow bands below the Fermi level in this charge transfer gap. There is very little hopping between the Eu-4f orbitals and the neighboring cations, since the radii of the 4f orbitals are much smaller than that of the 5s or 5p orbitals. This is the reason that the Néel temperature is low, and the Eu-f bands are narrow. (The Néel temperature is further lowered because of the competition between ferromagnetic and antiferromagnetic exchange interactions.) The Hubbard-U applied on the Eu-f states (U_{Eu}) shifts the energy level of the narrow Eu-f bands, and hence determines the gap between them and the Ti d or O p bands.

3.3.2 An Intriguing Thought Experiment: Polar Mode Frequency versus Hubbard-U

To begin unraveling the mechanism behind the soft mode behavior of $EuTiO_3$, we perform a thought experiment where we calculate the frequencies, ω_{SM}, of the polar phonons of cubic (space group $Pm\bar{3}m$) $EuTiO_3$ from first principles, for several different values of the Hubbard-U (applied to the Eu-f states, U_{Eu}). This is plotted in Fig. 3.3. Note that the frequency at a value of $U_{Eu} \sim 6$ eV reproduces well the experimental value, $\omega_{SM} \sim 75$ cm^{-1}, determined from a Cochran fit.[1]

There are two clear trends in Fig. 3.3: (i) as is now well-known, ω_{SM} is lower in the ferromagnetic (FM) state, which explains [52] an increase in the ionic contribution to the dielectric constant [38], $\epsilon_{\text{ion}} \sim 1/\omega_{SM}^2$, under external magnetic field, and (ii) ω_{SM} depends sensitively on U_{Eu}. With regards to the latter, notice how a relatively modest increase in U_{Eu} greatly decreases ω_{SM}. This is surprising as the polar soft-mode of $EuTiO_3$ is driven by the off-centering of the Ti^{4+} cation, i.e., B-site driven, in a second order Jahn-Teller like process [18, 41, 133, 19] (we elaborate on this below), and therefore it is not expected to depend so sensitively on the energy of the Eu bands, or U_{Eu}. Furthermore, the Hubbard-U_{Eu} acts only on the 4f shell of the Eu ion, which has a smaller radius than the fully occupied 5s and 5p shells, making a direct effect on the phonon frequencies less likely.

These observations, along with the fact that magnetism originates from the unpaired electrons on Eu, suggests that the Eu-f states may play a role in the

[1] It is pleasing that the original DFT paper determined a value of U similar to this by comparing the calculated magnetic exchange parameters to experiment, and then predicted a ω_{SM} frequency remarkably close to the experiment.

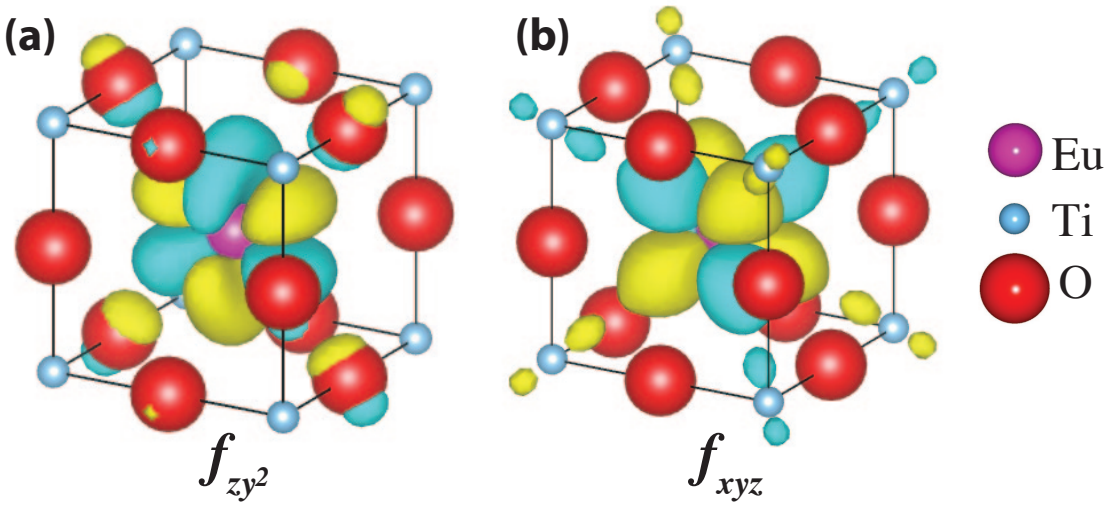

Figure 3.4: Two examples of maximally localized Wannier functions of Eu f electrons in $EuTiO_3$. (a) $f_{zy^2} \sim z(4y^2 - z^2 - x^2)$, (b) $f_{xyz} \sim xyz$. Yellow and green parts of the Wannier Function correspond to isosurfaces of opposite sign, and the Europium ion is in the center of the cubic cell.

origin of spin-lattice coupling. To probe this further, next we take a closer look at the spin-dependent hybridization of Eu-f electrons with other orbitals and with its effect on the soft-mode behavior.

3.3.3 Magnetic Order Control of Eu-f/Ti-d/O-p Hybridization

Despite the small radii of the Eu 4f orbitals, there are no bands purely of Eu character. This is seen in the site-projected density of states (DOS) as shown in Fig. 3.2a. The DOS peak right below the Fermi level is of dominantly Eu-f character, i.e., the wavefunctions in the energy window corresponding to this peak are mostly localized on the Eu ions, and have the symmetry of f states. There is, however, a small but non-zero contribution from Ti and O ions to this peak as well, indicating that the Eu-f states hybridize with both Ti and O atomic

orbitals [2]. This becomes strikingly clear by considering maximally localized Wannier functions (MLWFs) [110]. In Figure 3.4, we show two examples of occupied Eu f MLWFs, f_{zy^2} and f_{xyz} Wannier orbitals, respectively.[2]

Of particular interest is the Eu-ion's f_{xyz} Wannier orbital, Fig. 3.4b, which has lobes directed towards the Ti cation. Notice that the MLWF is mostly localized around the ion's core. There is, however, a small, but nonzero, weight around the neighboring Ti ions. This is an explicit sign that this Eu state hybridizes with a nominally empty Ti-d state(s). This hybridization is important for several reasons, e.g., it has been shown previously that it leads to a superexhange interaction mediated through the Ti cations [135, 2, 22].

Our interest here is in the fact that this component of the MLWF can be thought as representing the partial occupation of the Ti-d orbitals. It turns out that the dependance of this hybridization on a Hubbard-U applied to the Eu-f states, U_{Eu}, brings out the underlying physics of spin-phonon coupling in $EuTiO_3$. In Fig. 3.5, we plot the total charge within the Ti-d manifold of states due to the hybridization with Eu-f states (σ_{Ti}) as a function of U_{Eu}, considering both the ground state G-type antiferromagnetic and ferromagnetic spin configurations. We obtain σ_{Ti} by integrating the DOS projected onto the Ti-d shell over the energy window corresponding to the Eu-f bands (between ≈ -0.5 and ≈ 0.0 eV). This quantity, σ_{Ti}, is also related to the weight of the Eu-f MLWFs localized on a Ti site seen in Fig. 3.4b. Although σ_{Ti} is small, there are two clear trends that are evident in Fig. 3.5.: (i) σ_{Ti} decreases with increasing U_{Eu} and (ii) σ_{Ti} is larger in the AFM state compared to the FM one.

[2] All of the Wannier functions presented in this study are calculated using an energy range that covers only the Eu f bands. No unentanglement is required since these bands are well separated in energy from others.

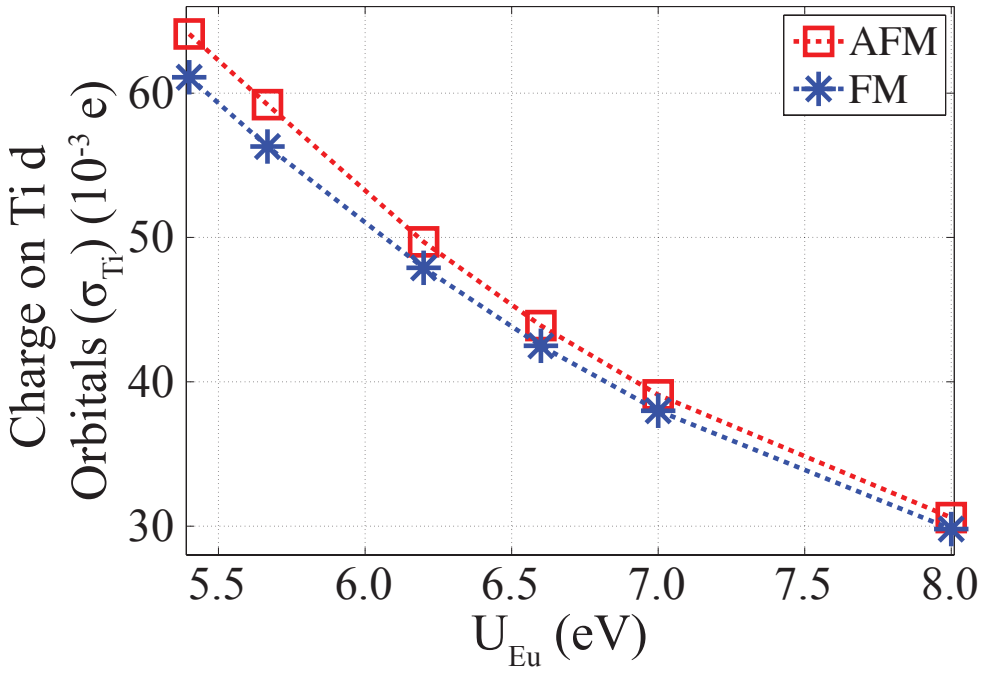

Figure 3.5: Charge on Ti d orbitals due to hybridization of the Eu f states (σ_{Ti}) versus Hubbard-U_{Eu} used in DFT+U calculations. Red squares and blue asterisks denote values in AFM and FM states respectively.

The latter will be explained in the proceeding section while the former, a change in the amount of hybridization with increasing U_{Eu}, is not surprising. For example, adding a Coulomb interaction, U, to DFT causes the corresponding electrons to become more local. Increasing U_{Eu} makes it energetically favorable for electrons to remain localized in Eu-f orbitals. As a result this decreases the hybridization between the Eu-f and the Ti-d states. This is also clearly visible in Fig. 3.6, where the f_{xyz} MLWF is plotted for different values of U_{Eu}. As the Coulomb interaction increases, the lobes localized near the Ti cation get smaller and eventually disappear, consistent with a decreasing σ_{Ti}.

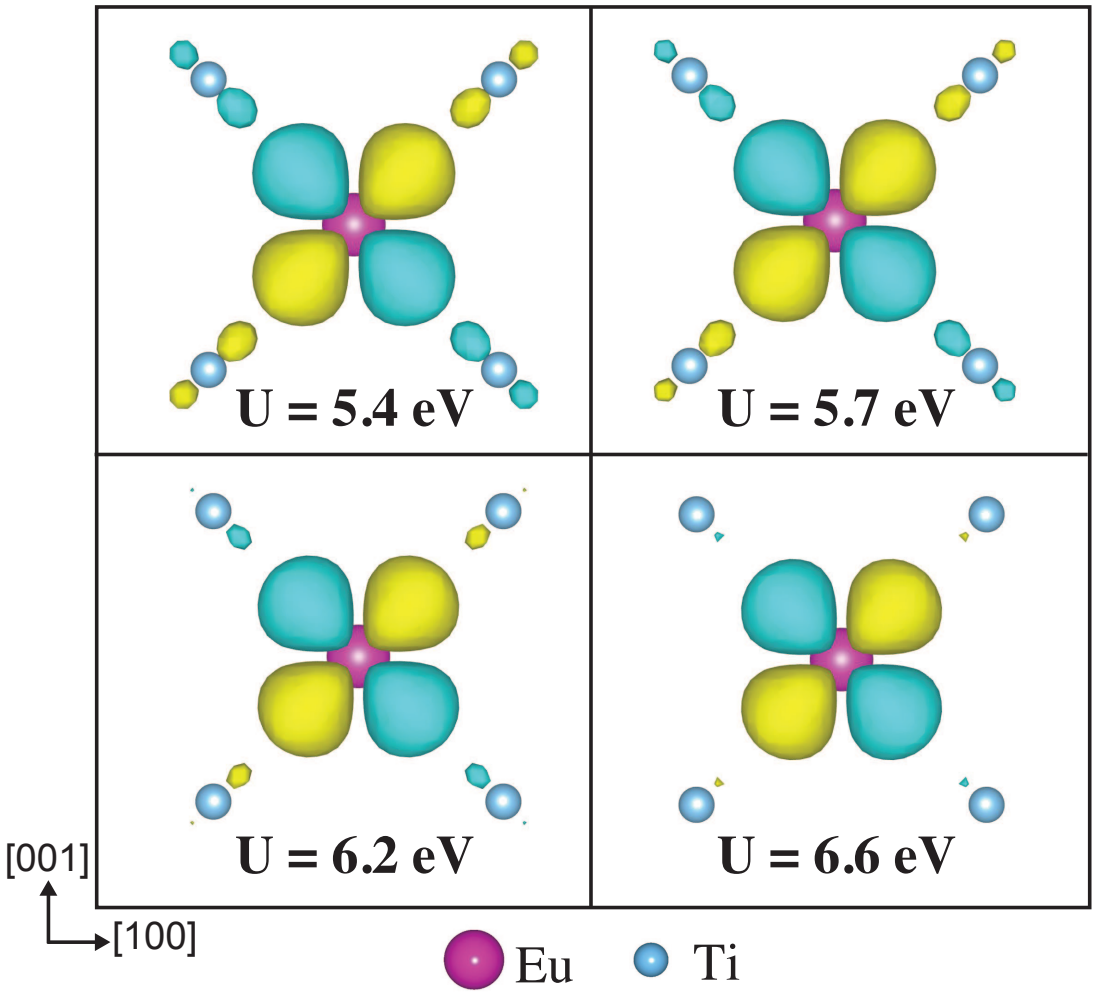

Figure 3.6: The Eu f_{xyz} MLWF for different values of U_{Eu}. For simplicity, the oxygen ions are not shown on the figure.

3.3.4 The Suppression of Ferroelectricity

Ferroelectricity in prototypical perovskite ferroelectrics such as $BaTiO_3$ originates from a 'cross-gap' hybridization [150] of a cation's empty orbitals at the bottom of the conduction band (typically either a transition metal cation's d-orbitals, e.g., Ti^{4+}, or a lone pair active cation's p-orbitals, e.g., Bi^{3+}) and the occupied p states of the oxygens at the top of the valence band. This mechanism

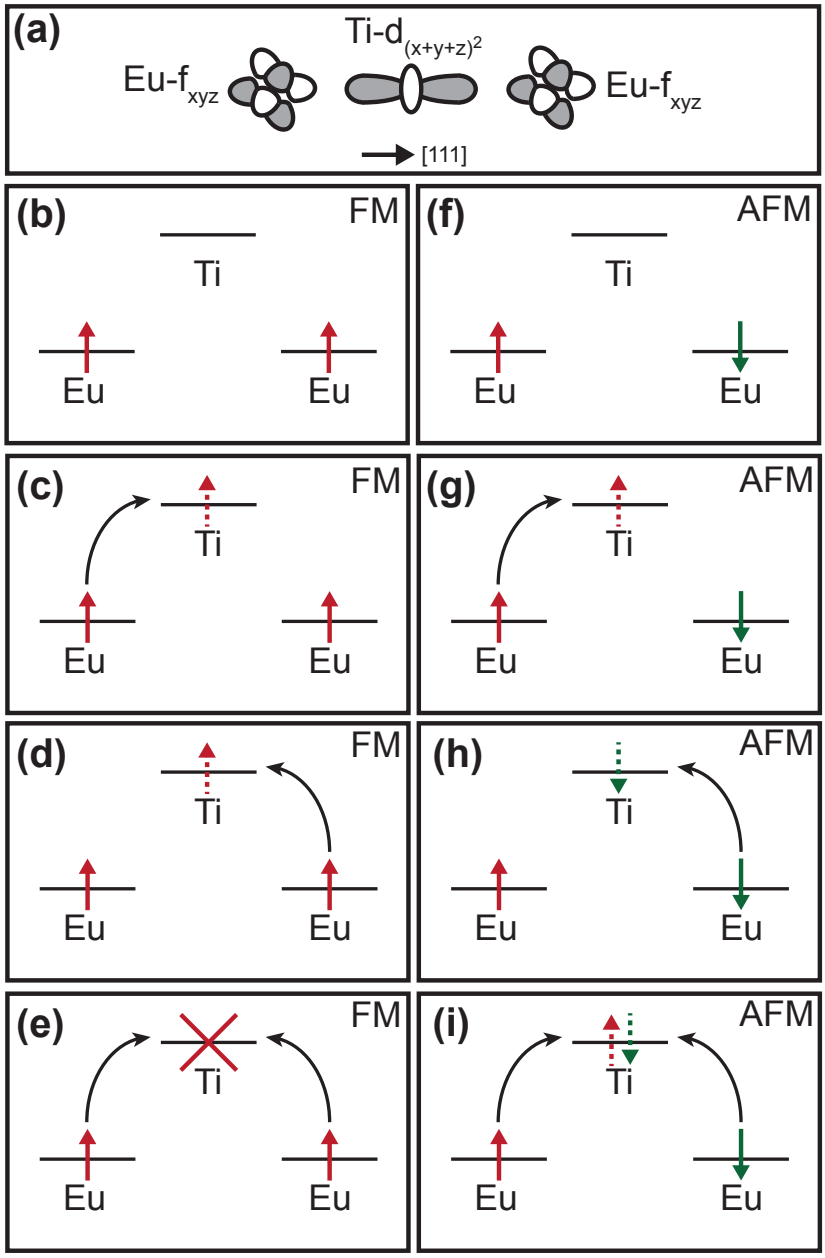

Figure 3.7: (a) Sketch of the f_{xyz} orbitals on 3^{rd} neighbor Eu ions and the intermediate Ti ion's $d_{(x+y+z)^2}$ orbital. (b) Energy levels of the three orbitals in the FM state. Lowest lying excitations where an electron hops onto the Ti cation, (c) and (d), are allowed, but not both the electrons can hop at the same time because of Pauli exclusion (e). However, in the AFM state, (f), not only the lowest excitations (g) and (h) but also the correlated hopping sketched in (i) is allowed.

can be thought of as a second order Jahn-Teller like process [18, 41, 133, 19]. This is the mechanism for ferroelectricity in strained $EuTiO_3$. Here, the displacement of a Ti cation towards one of the oxygens increases the Ti-3d/O-2p hybridization, thereby moving the hybridized empty states to higher energies, while lowering the energy of the hybridized occupied states. This 'rehybridization' leads to a second order energy gain favoring ferroelectricity. If, however, the transition metal d states are partially occupied, there is an extra energy cost associated with moving these states to higher energies, and the tendency towards ferroelectricity is reduced [87]. This argument has been mentioned often in the context of the incompatibility of ferroelectricity with B-site magnetism [78], and is central to both the suppression of ferroelectricity and the origin of spin-lattice coupling in $EuTiO_3$. But first we must understand why σ_{Ti} is larger in the AFM state than in a state with parallel spins (FM).

Consider the Eu-Ti-Eu exchange pathway along the [111] direction. In bulk $EuTiO_3$ these Eu cations have a strong AFM interaction, which leads to the observation of (predominantly) G-type magnetic order [1, 3, 143]. In Fig. 3.7a, the f_{xyz} orbitals on two neighbor spin-polarized Eu^{2+} cations, and the $d_{(x+y+z)^2}$ orbital on the intermediate non-magnetic Ti^{4+} cation are shown. (This particular *d* orbital has lobes directed towards both Eu cations and therefore will have the largest hopping to/from the f_{xyz} orbitals.)

First, imagine that the Eu spins were aligned parallel (FM), rather than in the observed AFM configuration. In Fig. 3.7b, we sketch the energy levels of the three orbitals in this state. Notice that an electron from either Eu cation is allowed by symmetry to hop to the Ti cation (Fig. 3.7c and d), but that the higher order process where both electrons hop to the Ti atom simultaneously (Fig. 3.7e)

is not allowed due to Pauli exclusion principle. Next consider the same process but with the spins aligned antiparallel (AFM) (Fig. 3.7f). Now, in addition to the two individual hopping processes, Fig. 3.7g-h, the correlated hopping process in Fig. 3.7i is allowed, leading to a larger hybridization, thus, a larger σ_{Ti} in the AFM state. Combining the physics represented in Figure 3.7 with that of the rehybridization mechanism of ferroelectricity leads to a straightforward explanation for the suppression of ferroelectricity and the origin of spin-lattice coupling in $EuTiO_3$.[3]

As a thought experiment, initially consider bulk $EuTiO_3$ in which the Eu-f/Ti-d hybridization was removed. One way this can be done from first-principles is by putting the f-electrons in the core of the PAW potential. In this case, the Ti-d states are essentially empty and are free to hybridize with the O-2p states as the Ti^{4+} cations move off-center, creating a polar lattice distortion is a second-order Jahn-Teller process. In this case, $EuTiO_3$ should have a ferroelectric instability as in $SrTiO_3$. Our calculations directly confirm this. Turning on the Eu-f/Ti-d hybridization, by moving the f-eletroncs from the core of the PAW potential to the valence, increases the occupancy of the Ti d states. This lowers the energy gained from the 2nd order Jahn-Teller thereby decreasing the tendency towards ferroelectricity, and thus hardening the polar soft-mode. This not only explains the suppression of ferroelectricity in $EuTiO_3$ but also our previous result shown in Fig. 3.3 (another 'dial' one can turn to remove, albeit partially, the Eu-f/Ti-d hybridization, and thus increase the tendency towards ferroelectricity, is to increase the Hubbard-U applied to the Eu f states, U_{Eu}.)

[3]Note that DFT with the LDA or GGA approximations is essentially a mean field theory [103] and as a result such correlated processes are not included in it. However, the requirement that the Kohn-Sham states (and the corresponding Wannier states) are orthonormal essentially leads to the same result that if the Eu spins are antiparallel the f electrons can delocalize to the d states of the Ti ion more.

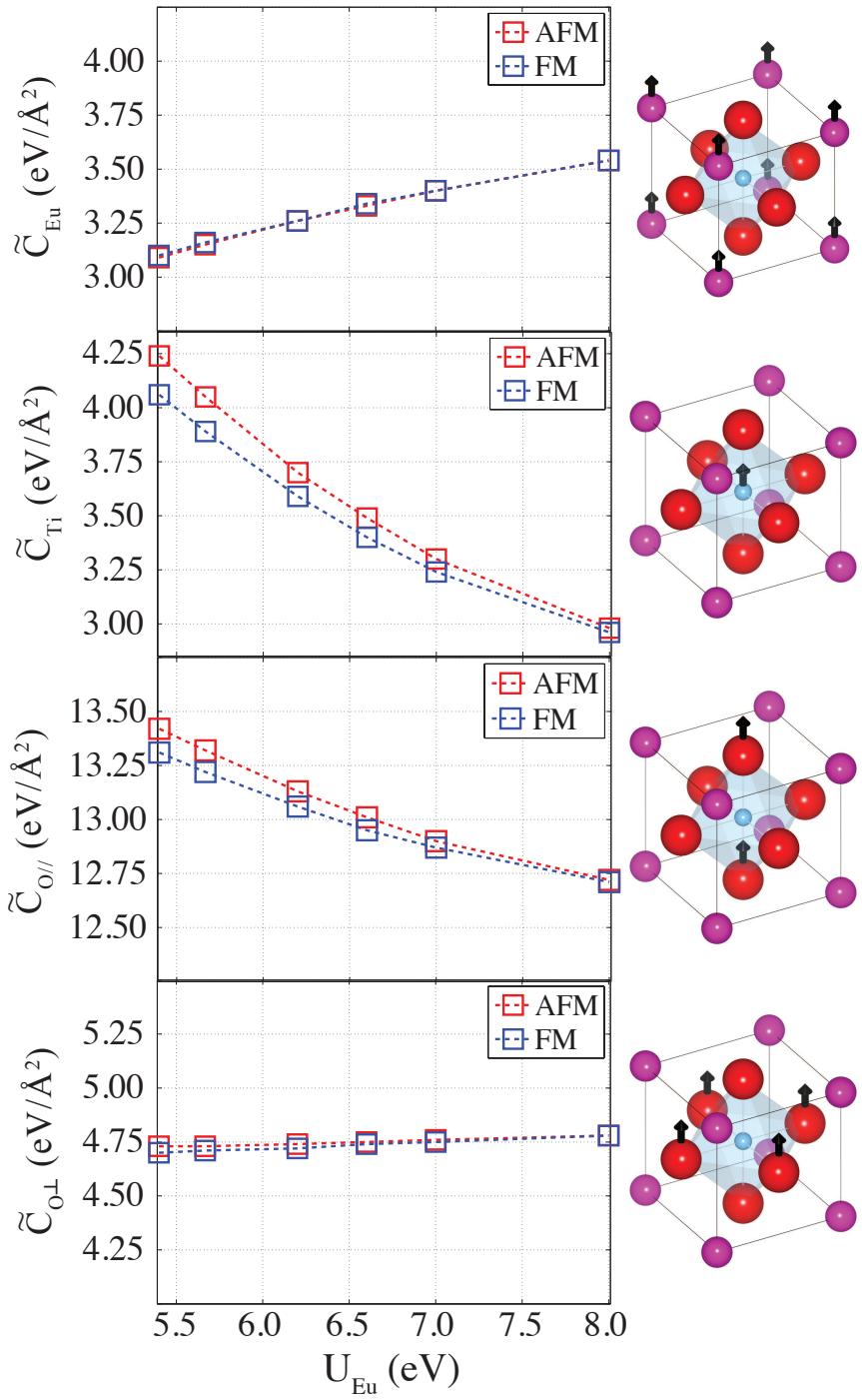

Figure 3.8: Self force constants ($\tilde{C}$) for the four Γ point symmetry adapted modes (left) and the corresponding displacement patterns (right). Red squares and blue asterisks denote the force constants in AFM and FM states respectively.

In order to lend support for this scenario, the self force constants, $\tilde{C}$ (i.e., the second derivatives of the total energy with respect to the corresponding ionic displacements) of the 4 symmetry adapted modes of the infrared-active (IR-active) irrep are plotted as a function of U_{Eu} in Fig. 3.8. First note that only $\tilde{C}_{Ti}$ and $\tilde{C}_{O\parallel}$, which are the only symmetry adapted modes that lead to a first order change in Ti-O distances, decrease significantly with increasing U_{Eu}, while $\tilde{C}_{Eu}$ actually increases. Therefore, the softening of ω_{SM} with increasing U_{Eu} primarily comes from the softening of the relative motion of Ti moving against $O\parallel$ and not from the Eu motion. These observations support the claim that the phonon softening with increasing U_{Eu} is a consequence of decreasing Eu-Ti hybridization.

3.3.5 The Mechanism of Spin-Lattice Coupling and the Origin of Ferromagnetism in Strain-Induced Ferroelectric $EuTiO_3$

If the spins in $EuTiO_3$ could be aligned in a parallel direction, e.g., in the presence of a strong magnetic field, the system would respond by decreasing the Eu-f/Ti-d hybridization, which would subsequently decrease the occupancy of the Ti-d states, σ_{Ti}, and result in a softening of the polar soft-mode. As a result, $\tilde{C}_{Ti}$ and $\tilde{C}_{O\parallel}$ should (and do) have a significant FM-AFM splitting, while $\tilde{C}_{Eu}$ and $\tilde{C}_{O\perp}$ have none, as clearly seen in Fig. 3.8. Also note that the splittings of $\tilde{C}_{Ti}$ and $\tilde{C}_{O\parallel}$ decrease with increasing U_{Eu}, since σ_{Ti} decreases. This is the microscopic origin of the spin-phonon observations of Katsufuji and Takagi. (Note that the AFM-FM splitting of ω_{SM} does not decrease significantly with U_{Eu}, Fig. 3.3, be-

cause the eigenvector changes.)

Now imagine that the tendency towards ferroelectricity is greatly increased so as to dominate over the electronic energy gained from the Eu-f/Ti-d hybridization. The system would respond by decreasing the occupancy of the Ti-d states, σ_{Ti}, so as to further increase the energy gain from the polar lattice distortion. This is accomplished by decreasing the Eu-f/Ti-d hybridization, thereby promoting FM interactions between the spins.

As an additional cross-check, in Fig. 3.9 we plot $\tilde{C}_{Ti}$ as a function of σ_{Ti}. The self force constant of Ti is seen to have an almost linear dependence on σ_{Ti} and more importantly, it does not depend on the particular magnetic order, FM or AFM. This universal behavior indicates that the dominant factor determining the change in $\tilde{C}_{Ti}$, and therefore ω_{SM}, is indeed σ_{Ti}. [4]

As a final check of the validity of our arguments we add a Hubbard-U on the Ti d orbitals as well. Increasing the energy cost of occupying Ti d states suppresses both the spin-phonon coupling and the dependence of ω_{SM} on U_{Eu} as expected. The strong dependence of spin-phonon coupling to the energy of Ti d states explains why similar spin-lattice physics has not been observed in other compounds similar to $EuTiO_3$, such as $EuZrO_3$ [89]. (Our calculations for cubic $EuZrO_3$ and $EuHfO_3$ indicate that the spin-phonon coupling in these materials is smaller than the numerical error, in line with our arguments.)

[4]Note, however, that the data obtained from the calculations in the AFM state (red) have a slightly larger slope than the one obtained from calculations in the FM state (blue). This indicates that while there are other contributions to spin-phonon coupling apart from the mechanism discussed in this study, they are relatively small.

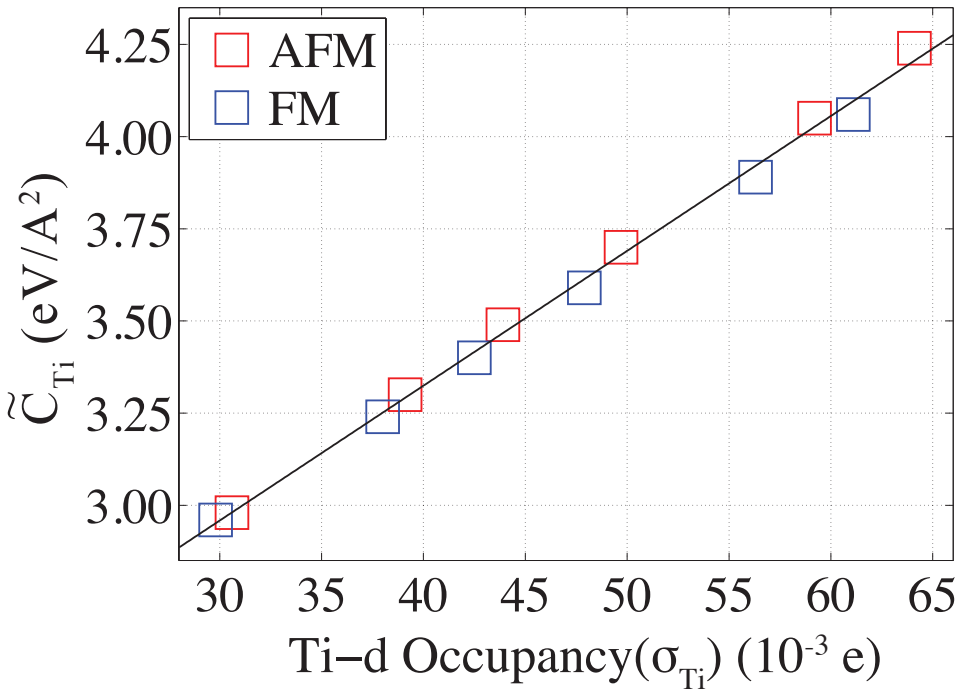

Figure 3.9: Self force constant of Ti ion ($\tilde{C}_{Ti}$) as a function of σ_{Ti} (the charge on Ti d shell due to hybridization with Eu f states). Red and blue curves denote values calculated in AFM and FM states respectively. Black line is a best fit to the data. Note that the data on this plot can be extracted from Fig. 3.5 and 3.8.

3.3.6 Oxygen Octahedral Rotations

The second question we posed in the introduction concerned the much stronger energy scale associated with rotations of the octahedra in $EuTiO_3$ compared with those in $SrTiO_3$. The experimentally measured octahedral rotation angle is also much larger in $EuTiO_3$ (3.6°) compared to $SrTiO_3$ (2.1°) [145, 65, 4]. As we now discuss, this also can be answered by considering the effect of Eu-f states.

Woodward, in his seminal work, showed that covalent bonding between the A-site cation and the oxygen anions has a stabilizing effect on the oxygen octa-

hedral rotations in perovskites [172]. The octahedral rotations change the coordination environment of the A-site and as a result significantly alter the covalent bonding strength and hybridization between the A-site cation and the oxygens. Akamatsu et al. pointed out another important effect of octahedral rotations in $EuMO_3$ (M=Ti, Zr, Hf) perovskites; they increase the overlap between the Eu-f and B-site d orbitals [3]. This results in an enhanced hybridization between these orbitals, which can also be seen explicitly in the charge density [3]. Just as the increased A–O covalency stabilizes octahedral rotations, this increased A–B hybridization also lowers the energy and hence stabilizes the rotational lattice distortion. This explains the stronger rotations observed in $EuTiO_3$ compared to $SrTiO_3$.

To help shed light on this observation, in Fig. 3.10a we plot the phonon frequency associated with the R point rotation mode in cubic $EuTiO_3$ as a function of U_{Eu}. With increasing U_{Eu}, the f electrons become more localized on the Eu ion, and as a result the stabilizing effect of the Eu-f/Ti-d hybridization decreases. This in turn results in the rotation soft mode becoming more stable (the magnitude of the imaginary frequency decreases). A similar trend is also observed in the ground state octahedral rotation angles reported in Fig. 3.10b; the rotation angle decreases with increasing U_{Eu}, approaching the value of $SrTiO_3$.[5] In other words, in terms of the octahedral rotations, the behavior of $EuTiO_3$ gets closer to that of $SrTiO_3$ with increasing U_{Eu}.

We also performed similar calculations to compare $EuZrO_3$ with $SrZrO_3$, using the same rotation pattern as $EuTiO_3$. The rotation angle difference between these two zirconates is as small as $\approx 0.3^\circ$. This is because $EuZrO_3$ has a much

[5]Note that the optimized rotation angles we calculate are much larger than the experimental value for both $EuTiO_3$ and $SrTiO_3$. The overestimation of rotation angles with respect to experiment is very common in DFT, for example, see Ref. [145].

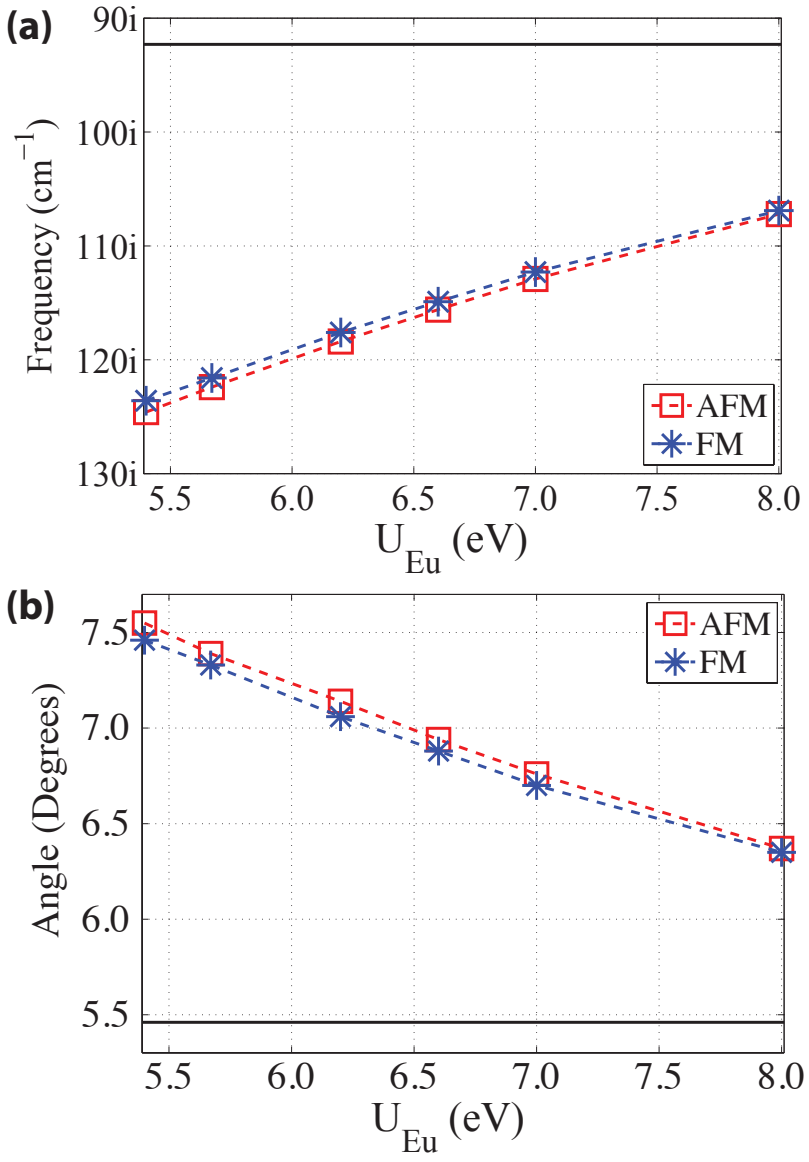

Figure 3.10: (a) R point rotation soft mode frequency as a function of U_{Eu} in the FM and the AFM states and the cubic structure with lattice constant fixed to 3.90 Å. The horizontal black line corresponds to the soft mode frequency in $SrTiO_3$, calculated with the same settings. (b) Octahedral rotation angle, obtained by relaxing the ions in fixed cubic cell, as a function of U_{Eu} in the FM and the AFM states. The horizontal black line corresponds to the rotation angle in $SrTiO_3$, calculated with the same settings. Lines connecting the data points are provided to guide the eye.

larger band gap than $EuTiO_3$, and as a result there is not a significant hybridization between the Eu-f and the Ti-d states that strengthens the octahedral rotations. The same applies to $EuHfO_3$, which has an octahedral rotation angle of 11.9°; merely $\sim 0.3°$ degrees larger than $SrHfO_3$.

3.4 Summary

In summary, in this chapter we elucidated the key role played by the Eu-f/Ti-d hybridization in $EuTiO_3$ by employing DFT+U calculations and MLWFs. The resultant charge transferred to the Ti-d states (σ_{Ti}) drives the system away from a ferroelectric (or quantum paraelectric) phase, and causes a dielectric behavior manifestly different from that of $SrTiO_3$. The dependence of σ_{Ti} on the magnetic order causes the polar soft-mode frequency to depend on the magnetic state. This is the leading contribution to spin-phonon coupling in $EuTiO_3$. Octahedral rotations are also affected from Eu f states' hybridization with Ti d orbitals, and are stronger in $EuTiO_3$ compared to $SrTiO_3$ as a result.

These results underline the importance of rare earth f electrons in the lattice dynamics and dielectric behavior of TM oxides [158]. While this chapter is focused on $EuTiO_3$, similar effects could exist in other compounds as well. Taking advantage of the hybridization of rare earth cation with the TM ion might be used as a new knob to tune the system away or close to the ferroelectric transition or perhaps to a quantum critical point.

CHAPTER 4

STRUCTURAL TRENDS IN TRANSITION METAL DIOXIDES WITH RUTILE AND RELATED STRUCTURES

In this chapter, we present a study on the structural properties of 12 different TM dioxide compounds. Our aim is to understand the properties of the so called Rutile crystal structure that is observed most of these compounds. The Rutile structure, originally observed in the mineral Rutile (TiO_2), is very common in transition metal dioxides and has been in the focus of intense research since its original observation in 1916 by Vegard [167]. Since it is a very common and relatively simple structure observed in so many different compounds, it is natural to seek to understand what determines the structural trends in various compounds with Rutile and related structures. There exist multiple experimental and theoretical studies that approach this issue. In particular, it has been studied in detail what determines the structural parameters in the Rutile phase, and why certain compounds exhibit a symmetry lowering distortion. (See Section 4.3 for a brief overview.) However, there exists no comprehensive first-principles study that considers a large counter of compounds and looks for systematic trends.

The aim of the study presented in this chapter is to consider, systematically, the dioxides formed by 4d and 5d transition metals of groups from 4 to 9, and understand the connection between their electronic and crystal structures. Particular emphasis is given to the cation pairing: In many of these compounds metal cations in edge sharing oxygen octahedral environments are displaced towards each other from the center of the octahedra to form cation pairs. We present a comprehensive symmetry analysis and linear response calculations to

understand not only the driving force of this symmetry lowering but also the effect of competing forces, such as the effect of the oxygen cations which resist such a displacement. We hope that our efforts bring a unified understanding to this topic and fill the gap between previous first-principles studies that focus on single compounds.

4.1 Introduction

The Rutile structure is ubiquitous in transition metal (TM) dioxides [34]. All but two early TM dioxides at least have a polymorph that has a Rutile related structure; i.e. either the Rutile, or a distorted variant of it. (See Table 4.1.) Two well-known examples of compounds in this family are TiO_2, which has been the state-of-the-art photocatalyst for water splitting for the last 40 years [57], and VO_2, which undergoes coincident metal-insulator and structural phase transitions at 340 K [114, 68]. Interest in TM dioxides in Rutile related structures stems from mainly two reasons: First, as a simple and very common structure that, in different compounds, lead to a variety of properties, it is natural to study the crystal and electronic structures of Rutile related TM dioxides. Second, with their bandgaps spanning a wide range, these compounds are perfect candidates for catalysis, both as the catalyst itself and as catalyst support [12]. There are also various recent studies on composites made of these compounds, which also call for a thorough understanding of the properties of the Rutile structure [123, 12].

The aim of this chapter is to study the structural and electronic trends of early TM dioxides in the Rutile related structures, and provide a common explanation of the details of the crystal structure. To the best of our knowledge, there

4d	ZrO_2 Not Rutile related structure	NbO_2 Distorted Rutile ($I4_1/a$)	MoO_2 Distorted Rutile ($P2_1/c$)	TcO_2 Distorted Rutile ($P2_1/c$)	RuO_2 High Symmetry Rutile ($P4_2/mnm$)	RhO_2 High Symmetry Rutile ($P4_2/mnm$)
5d	HfO_2 Not Rutile related structure	TaO_2 Distorted Rutile (?) ($I4_1/a$)	WO_2 Distorted Rutile ($P2_1/c$)	α-ReO_2 Distorted Rutile ($P2_1/c$)	OsO_2 High Symmetry Rutile ($P4_2/mnm$)	IrO_2 High Symmetry Rutile ($P4_2/mnm$)

Table 4.1: Low temperature experimental structures of the dioxides of the 4d and 5d transition metals from 4^{th} to 9^{th} groups; i.e. with 0 to 5 electrons in the outer d orbitals of the M^{4+} cation. By 'High Symmetry Rutile' we refer to the rutile structure with no symmetry lowering structural distortions. Data taken from Ref. [25, 27, 137, 138, 149, 148].

exists no complete first-principles study on the structural trends of these compounds [48]. So far, first-principles studies focused on either one or only few compounds at a time. Other theoretical studies such as Hueckel or shell model calculations did not consider more than a handful of compounds at a time either [152, 61]. This is despite a plethora of experimental studies that look for "systematic correlation of crystal chemistries" in these compounds [138, 139]. Lack of a complete first-principles studies on systematic trends is surprising because the first-principles methods provide the perfect toolbox for this purpose: Using Density Functional Theory (DFT) aided with group theory, it is possible to freeze out certain effects, such as strain coupling, and isolate and quantify tendencies for individual lattice distortions, such as cation pairing. It is also possible gain insight from the details of bandstructure and phonon spectra of high symmetry phases, which is otherwise not achievable in experiments.

In this chapter, we consider the 4d and 5d transition metals, from 4^{th} to 9^{th} groups, and their dioxide compounds with the Rutile and related structures.

By employing first-principles DFT calculations, we show that the crystal structure of these compounds is determined through an interplay between electronic structure [33], M-O coordination, and also the connectivity of the oxygen octahedron network. We hence present a unified picture that explains the structural trends of these compounds.

The chapter is organized as follows: We start by listing our methods in Section 4.2. We then give a brief overview of some of the previous studies on the Rutile compounds in Section 4.3. In Section 4.4, we explain the Rutile structure and its degrees of freedom in detail. We present our first-principles results for the high symmetry Rutile phase in the absence of lattice distortions in Section 4.5. We also discuss what determines the structural parameters in this phase, and consider the the effects of cation size, M-O coordination environment, metallic M-M bonding, and O-O repulsion. In Section 4.6, we study the cation pairing which is observed in many compounds with the Rutile structure. We present a group theoretical analysis, and the results of our linear response calculations. We then discuss the microscopic mechanisms that lead to a cation paired phase, and elucidate what determines the structural groundstate among different possible cation paired states. A discussion of whether the cation pairing is a cooperative phenomenon is also presented. We conclude with a summary in Section 4.7.

4.2 Methods

First-principles calculations are performed with Projector Augmented Waves [24, 94] using the VASP code [95, 93, 92]. Spin-Orbit interaction is ignored,

and Local Density Approximation [126] (LDA) is used in order to calculate the exchange-correlation energies. Certain trends are also checked by repeating calculation using the PBEsol exchange correlation functional [127] and no discrepancy is observed. An unshifted $8 \times 8 \times 14$ k-point grid is employed for the primitive cell. Gaussian smearing with an electronic temperature of 0.1 eV is used in all calculations. Certain Fermi surface related properties, such as the soft phonon mode frequencies due to a Kohn anomaly, depend strongly on the Fermi surface smearing [32, 58]. As a result, the exact quantitative values of quantities such as soft mode frequencies or the corresponding force constants matrix eigenvalues should be considered with care.

The force constants matrix (FCM) and its eigenvalues are calculated using Density Functional Perturbation Theory (DFPT) and building supercells for zone boundary modes [13]. Note that the very standard way that the linear response to the lattice displacements are treated, the Born-Von Karman Theory [105, 28], assumes that the electrons are always in their groundstate, and the Born-Oppenheimer approximation is made. For this reason, this approach is meaningful only for insulators which have a finite band gap. It is possible to treat metals with the same formalism only if damping and retardation effects are neglected [131] and we do so throughout this study. Also, note that since we focus on the FCM eigenvalues, which are static quantities, such effects are not as important as they are for phonons.

At various points in this study, we made extensive use of the Isotropy Software Package [157] and the Bilbao Crystallographic Server [11, 10, 9, 162]. Visualization of crystal structures and calculation of certain properties have been achieved using Vesta [113].

4.3 History

Many TM dioxides have a structure which has the same bonding geometry as the Rutile structure, but is a distorted variant of it. This distorted variant often is a monoclinic structure where the metal cations are displaced along the [001] direction and form pairs; such as in NbO_2 at low temperatures, or in MoO_2. In particular, the so-called MoO_2 structure is very common: It is observed in VO_2, MoO_2, TcO_2, WO_2, and ReO_2. Interest in the paired state, and the transition to it, sparkled in 1959, when Morin discovered a metal-insulator transition in VO_2 that is coincident with the structural transition to the paired state [114]. Since then, VO_2 is studied extensively (for example see Ref. [98] and [161]). Prominent examples of work that focuses on VO_2 span a wide time range, including Goodenough's early theoretical work [68] as well as very recent first-principles calculations [49, 170, 16]. In Ref. [68] Goodenough explained the transition by the energy lowering of the occupied cation d states when cations pair. While the early DFT work could not reproduce the insulating state of VO_2; recent hybrid functional [49], LDA+nonlocalDMFT [170], and LDA+DMFT+V [16] studies are successful at that, and point to a 'Peierls-Mott insulator'. There are also many studies that consider the metal-metal (M-M) interactions in oxides and use VO_2 as an example: these include early theoretical work of Goodenough [67], as well as various tight binding [34] and early first-principles calculations [153].

Rutile structure provides a natural playground to study the direct M-M interactions not only because it allows a small separation between the metal cations, but also because a large number of different transition metal dioxides exist in this structure. As a result, other TM dioxides with Rutile and related structures other than VO_2 are studied in detail as well. For some examples, see Ref. [148]

for TaO_2, Ref. [149] for RhO_2 and PtO_2, Ref. [25] for NbO_2, Ref. [27] for MoO_2 and TcO_2, and Ref. [26] for GeO_2, SnO_2, RuO_2, and IrO_2. Even TcO_2, which is radioactive, has multiple studies dedicated to it [138, 137].

Since early 2000s, the development of computers and first-principles methods lead to an increase in first-principles studies of Rutile compounds. Examples include, but are not limited to, Eyert et al. who studied VO_2, NbO_2, and MoO_2 [50, 47, 48]; Hamad who studied TiO_2, VO_2, RuO_2, IrO_2, and SnO_2 [72]; Sorantin and Schwartz who studied TiO_2, VO_2, CrO_2, and RuO_2 [153]; and Rodriguez et al. who performed calculations on TcO_2 to support their experimental data [137]. Finally, in the last few years, more advanced first-principles methods have been put into use: In order to reveal the properties of the transitions in VO_2, Lazarovits et al. used cluster DMFT, Belozerov et al. used LDA + DMFT + V, and Eyert used hybrid functionals [99, 16, 49].

Despite this large number of studies on various different compounds, there is no consensus on why some of these compounds exist in a cation paired state whereas others do not. Goodenough predicted [68] that cation pairing would not be favorable in the presence of more than one electrons in the d orbitals. Eyert, in his works on MoO_2 and NbO_2, coined the term 'embedded Peierls instability' [50, 47] to explain a Peierls-like instability that can exist in the presence of multiple partially filled bands, thus contradicting Goodenough. Eyert's picture is consistent with that of Burdett et al. [34], who also emphasized the effect of anion sublattice in opposing the Peierls distortion [33]. The fact that pairing exists in compounds with different number of electrons in the TM d shell is argued to preclude possibility of pairing being a Fermi surface effect [50]. Also, a clear connection (or lack thereof) between the proposed scenarios and Fermi

surface effects, i.e. nesting, is missing. Finally, whether the cation pairing is a cooperative phenomenon, i.e. requires a certain number of atoms to be coherently displaced from their high symmetry (unpaired) position, or a single cation pair can lower its energy by forming a local bond is also an unanswered question [67].

4.4 The Rutile Structure

In this section, we give a detailed explanation of the Rutile structure, its degrees of freedom, and its bonding geometry. The Rutile structure with the simple tetragonal spacegroup $P4_2/mnm$ is shown in Figure 4.1a. Its primitive unit cell contains two MO_2 formula units, where the metal cations form a body-centered tetragonal lattice and oxygen anions form an octahedral cage around each metal cation. In our convention, metal cations are at reduced coordinates $(0,0,0)$ and $(1/2,1/2,1/2)$, and oxygens are at $(u,u,0)$, $(1-u,1-u,0)$, $(1/2+u,1/2-u,1/2)$ and $(1/2-u,1/2+u,1/2)$. There are three degrees of freedom: in-plane lattice constant a, the out-of-plane lattice constant c, and the anion parameter u. The octahedra in general are not regular: the apical axis, which is along [110] (or $[\bar{1}10]$) direction, has a different length then the two basal axes that are along [111] and $[\bar{1}11]$ (or $[11\bar{1}]$ and $[\bar{1}1\bar{1}]$) directions. The interplay of u with c/a determines how close the octahedra are to a regular octahedron.

The oxygen octahedra form a connected network in all three directions. The properties of this octahedral network is more complex compared to that in perovskites, which have been focus of intense research in the field of oxides. Oxygen octahedra in perovskites form a corner sharing network along all three di-

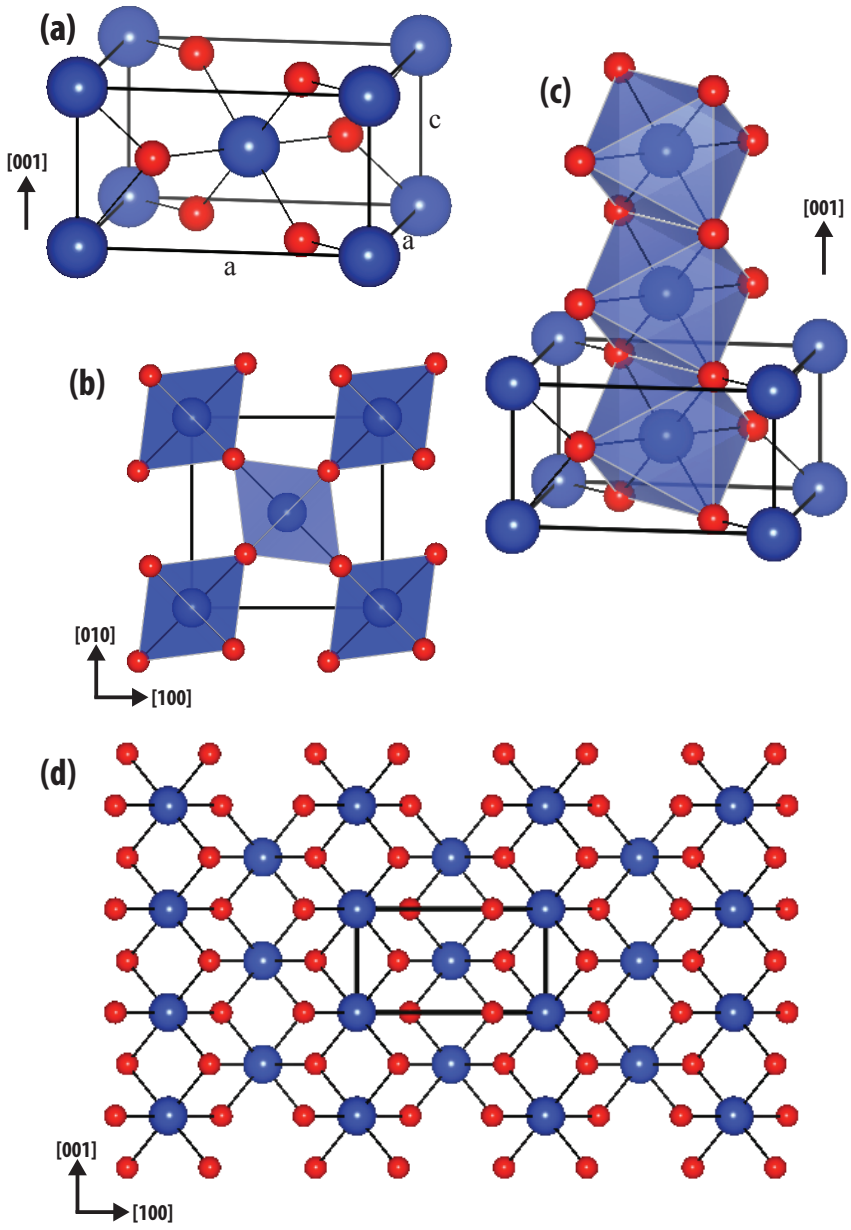

Figure 4.1: The Rutile structure. Red spheres represent oxygens, and blue spheres represent metal cations. (a) The primitive unit cell, which contains two formula units. Each metal ion is surrounded by six oxygens, and each oxygen makes bonds with three cations. (b) The corner-sharing octahedron network, as seen from [001] direction. (c) Oxygen octahedra form edge sharing chains in the [001] direction. (d) The metal-oxygen network as seen from [100] direction.

rections. The network in Rutiles is likewise corner sharing in the (001) planes, however, two planes of cations that are separated by half a lattice vector along [001] lead to two layers of octahedra that are translated by half a lattice vector. As a result, the apical axis of neighboring octahedra alternate between [110] and [$\bar{1}$10] (Fig. 4.1b). Along [001], the octahedra are not corner sharing but edge sharing instead (Fig. 4.1c). The resulting pattern of metal-oxygen (M-O) bonds (Fig. 4.1d) precludes the possibility of any octahedron rotation/tilting degree of freedom: There is no normal mode that just changes the orientation of oxygen octahedra without distorting them or displacing metal cations as well. Another result of the edge-sharing octahedra is a small metal-metal (M-M) distance that causes strong direct M-M interactions, as opposed to M-M interactions that are mediated by the oxygen anions [35, 67]. This can lead to structural instabilities as suggested by Pauling's third rule, and to formation of covalent bonds between metal cations [67].

Because of the octahedral coordination, each metal cation is bonded with six oxygens. Each oxygen, on the other hand, is bonded with three cations. There are two inequivalent M-O bond lengths in each octahedron: Two apical and four basal bonds. Bond angles are not equivalent either: For each oxygen anion, the three M-O-M bonds are split to 2+1 inequivalent angles. O-M-O bond angles are split as well: O-M-O angles between an apical and a basal oxygen are 90°, whereas the O-M-O angle between two basal oxygens differ from 90°.

4.5 Structural Trends of Early Transition Metal Dioxides in the High Symmetry Rutile Phase

4.5.1 First-principles Results

We start our survey by studying the structural trends of early 4d and 5d transition metal dioxides in the Rutile structure, which has the space group $P4_2/mnm$. In order to differentiate it from a structure with cation pairing, we refer to this structure as the high symmetry (HS) Rutile from now on. While compounds such as RuO_2 have this structure at all temperatures, for other compounds such as MoO_2 the HS Rutile structure is not observed experimentally. In this respect, we use the power of first-principles methods to perform a thought experiment and consider these compounds in this yet to be observed phase where distortions that reduce the symmetry from the HS Rutile phase are zeroed out. We perform full ionic relaxations by keeping the spacegroup as $P4_2/mnm$, i.e. without permitting any symmetry lowering. The minimum energy structure is obtained by optimizing the energy over the three degrees of freedom, a, c, and u.

In Figure 4.2, the resulting lattice constants, anion parameter, and unit cell volume are plotted for all 4d and 5d compounds we considered. All of these quantities display very similar trends for 4d and 5d compounds as a result of the similar chemical properties of 4d and 5d elements. The unit cell volume monotonically decreases going from left to the right of the periodic table (i.e. with increasing d orbital filling), which can be explained by the decrease in the ionic radii (Fig. 4.3). This fact that the trend of the volume can be explained solely by ionic radius is experimentally verified in distorted Rutile type struc-

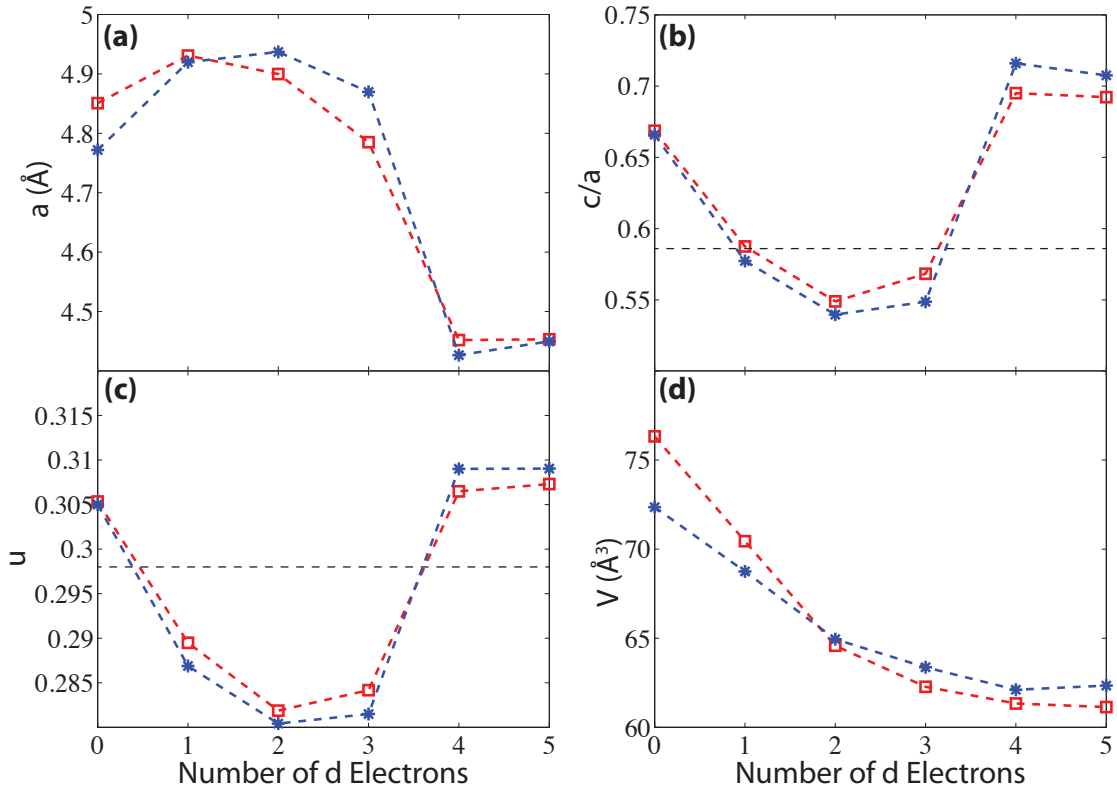

Figure 4.2: Structural parameters from first-principles calculations for the TM dioxides in hugh symmetry Rutile phase as a function of the number of d electrons on the M^{4+} cation. (a) In-plane lattice constant a. (b) c/a ratio; i.e. the ratio of in-plane and out-of-plane lattice constants. (c) The anion parameter u. (d) Volume of the primitive unit cell. Red and blue data correspond to 4d and 5d compounds respectively. Horizontal, dashed black lines correspond to the values of c/a and u in the ideal Rutile structure, i.e. when the oxygen octahedra are regular.

tures as well [138]. However, the nonmonotonic trends of a, c/a and u cannot be explained simply by geometric arguments. We will consider the reasons behind these trends in Section 4.5.2.

The Baur Distortion Indices and Bond Angle Variances are plotted in Fig. 4.4. (See Section 4.8 for a definition of these quantities.) The values of B for different compounds span only a very narrow range, and are no larger than

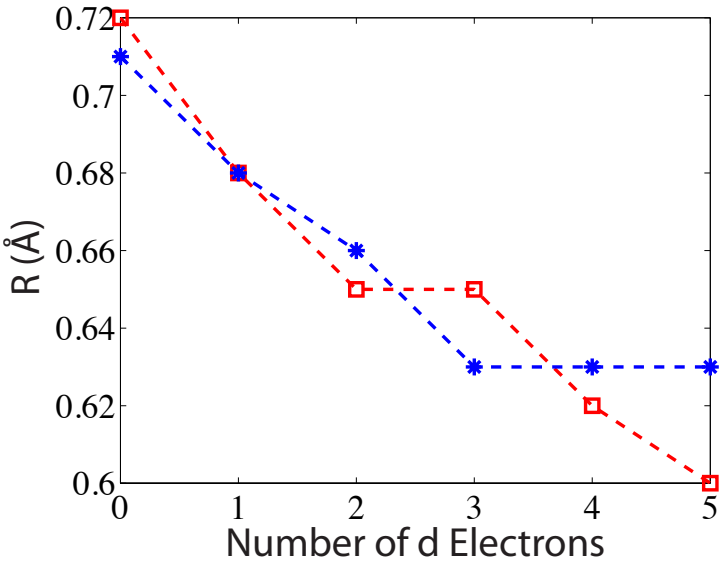

Figure 4.3: Effective ionic radii for transition metal ions in the 4+ oxidation state, as a function of the number of d electrons on the M^{4+} cation. Red and blue data correspond to 4d and 5d cations respectively. (Data from Ref. [116].)

$\sim$ 0.02. This indicates that the M-O bond lengths are very regular in all the compounds. However, this does not mean that the oxygen octahedra are close to regular: The Bond Angle Variance σ_θ is as large as 8° in d^4 and d^5 compounds, which shows that the octahedra are quite distorted.

4.5.2 What Determines c/a, u and How Regular the Octahedra Are

While the trend of the cell volume in different compounds can be explained by decreasing ionic radii of cations as one goes from the left to the right of the periodic table, the trends of c/a and u are not as easy to explain. These parame-

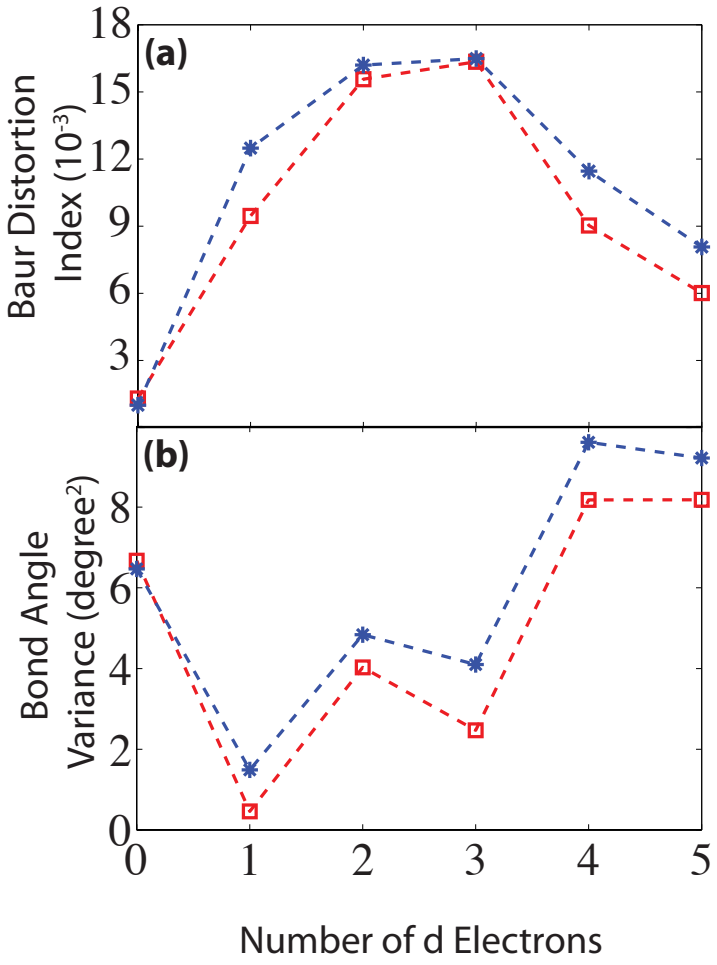

Figure 4.4: (a) Baur Distortion Indices and (b) Bond Angle Variances for TM dioxides in the high symmetry Rutile structure as a function of the number of d electrons on the M^{4+} cation. Red and blue data correspond to 4d and 5d cations respectively.

ters are determined by an interplay of multiple factors, such as the electrostatic repulsion between the anions, the metal-metal bonding, and the geometry of oxygen sp^2 orbitals [153, 26]. In this section, we consider each these effects and explain the reasons behind the observed trends.

The oxygen octahedra in the TM dioxides in the high symmetry Rutile structure are in general not regular. Following Ref. [153], we refer to the Rutile struc-

ture with regular octahedra as the *ideal Rutile* structure.[1] The regular octahedra condition determines both the c/a ratio and the anion parameter u uniquely: The requirement that all M-O distances are equal sets

$$u = \frac{1}{4} + \frac{1}{8}\left(\frac{c}{a}\right)^2 \tag{4.1}$$

which determines u as a function of c/a. This, combined with the condition that all O-O distances are equal sets [153]

$$u_{ideal} = 1 - \frac{1}{\sqrt{2}} \simeq 0.293, \tag{4.2}$$

and

$$\left(\frac{c}{a}\right)_{ideal} = 2 - \sqrt{2} \simeq 0.586. \tag{4.3}$$

Even though it consists of regular octahedra, the ideal Rutile structure is by no means the most favorable structure in terms of the M-O bonding: this is because of the unfavorable M-O-M bond angles [153]. Oxygen ions are three-fold coordinated with metal cations, and the hybrid sp^2 orbitals on the oxygens call for three equal 120° M-O-M angles. However, ideal Rutile structure has two 135° and one 90° angles (Fig. 4.6a), which is highly unfavorable. In order to relieve this stress on the bond angles, the compounds tend to have larger u and c/a values than those in equations (4.2) and (4.3). For example, our calculations show that the archetype TiO_2 has $c/a = 0.642$ and $u = 0.304$.

The results in Fig. 4.2 indicate that compounds with d^1, d^2 or d^3 cations, both u and c/a are lower than their ideal values, which is totally contrary to what is expected. This is an indication of strong M-M interactions in these compounds [138, 26]: The attractive interaction, which is the result of metal-metal bonds, decreases the c/a ratio, in the expense of unfavorable M-O-M angles. Strength

[1] By calling it ideal, we by no means imply that this is the most favorable structure.

of the metallic cation-cation bonding and the resulting decrease in the c/a ratio depends on the electronic structure, and will be studied in detail in the next Section.

The value of u, in turn, is determined by the metals' tendency to have a symmetric anion coordination, i.e. the M-O bond lengths being of the same length, and the electrostatic repulsion between the anions. In other words, c/a determines u [26]. In order to prove this point, in Fig. 4.5b we plot the value of u that is obtained from c/a using Eq. 4.1. The trend of u that gives the lowest energy, plotted again in Fig. 4.5a, is caught pretty well by Eq. 4.1, indicating that the preferred value of u is determined in order to have a symmetric ligand environment for the metal cations for every value of c/a. The values that Eq. 4.1 gives are slight overestimates because the repulsion between oxygen anions is not taken into account: optimized u is lower so that the O-O distances are larger.

In Fig. 4.6 the variation of M-O-M angles is presented. Note that depending on the c/a ratio, the angles can be either below or above their ideal values. This is the reason of the rise in σ_θ for d^2 compounds compared to d^1 and d^3 ones.

4.5.3 Electronic Structure and the M-M Bonding in the High Symmetry Rutile Phase

It is argued in the context of various compounds that the crystal structure of the TM dioxides with Rutile related structures are strongly affected by their electronic structure [33, 34, 138, 72, 68, 50, 47, 48, 49]. In this section, we consider the coordination geometry, the resulting bonding between the TM d orbitals,

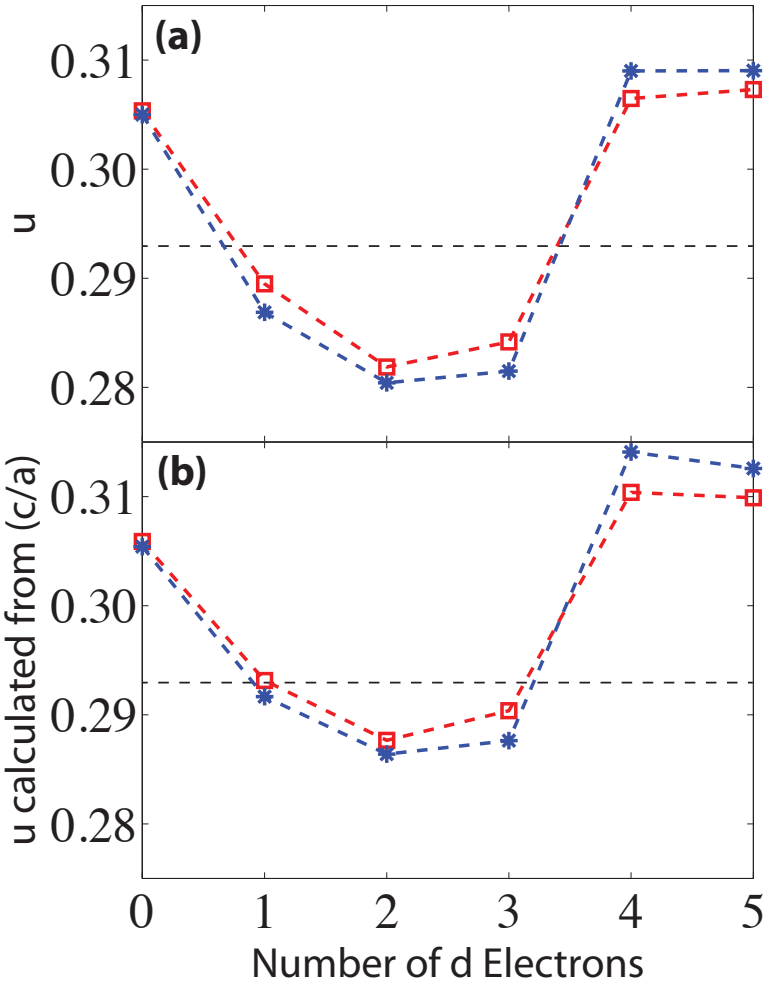

Figure 4.5: The anion parameter u as a function of the number of d electrons on the M^{4+} cation; (a) obtained from ionic relaxations, and (b) calculated from using c/a through Eq. 4.1. Red and blue data correspond to 4d and 5d cations respectively. Horizontal, dashed black lines correspond to the value of u in the ideal Rutile structure, i.e. when the oxygen octahedra are regular.

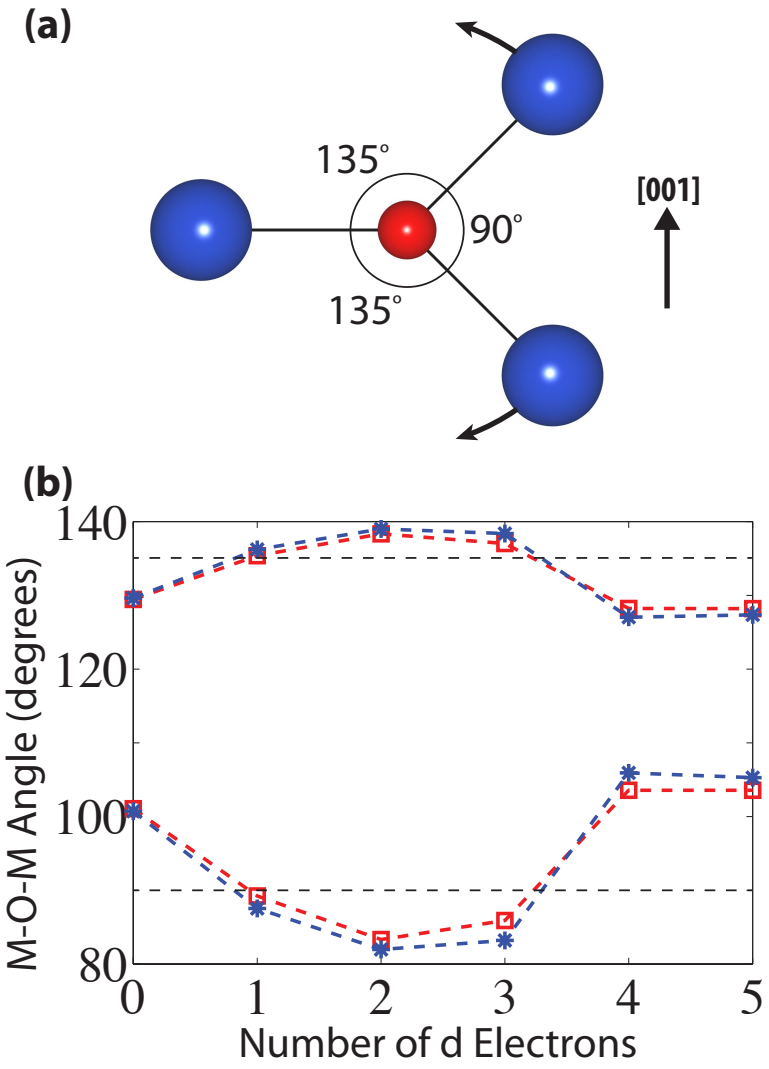

Figure 4.6: (a) Sketch of the Metal-Oxygen angles in the ideal Rutile structure. (b) The Metal-Oxygen-Metal angles in the TM dioxides in the high symmetry Rutile structure as a function of the number of d electrons on the M^{4+} cation, from first-principles. Red and blue data correspond to 4d and 5d cations respectively. The horizontal lines drawn at 90° and 135° correspond to the angles in the ideal Rutile structure.

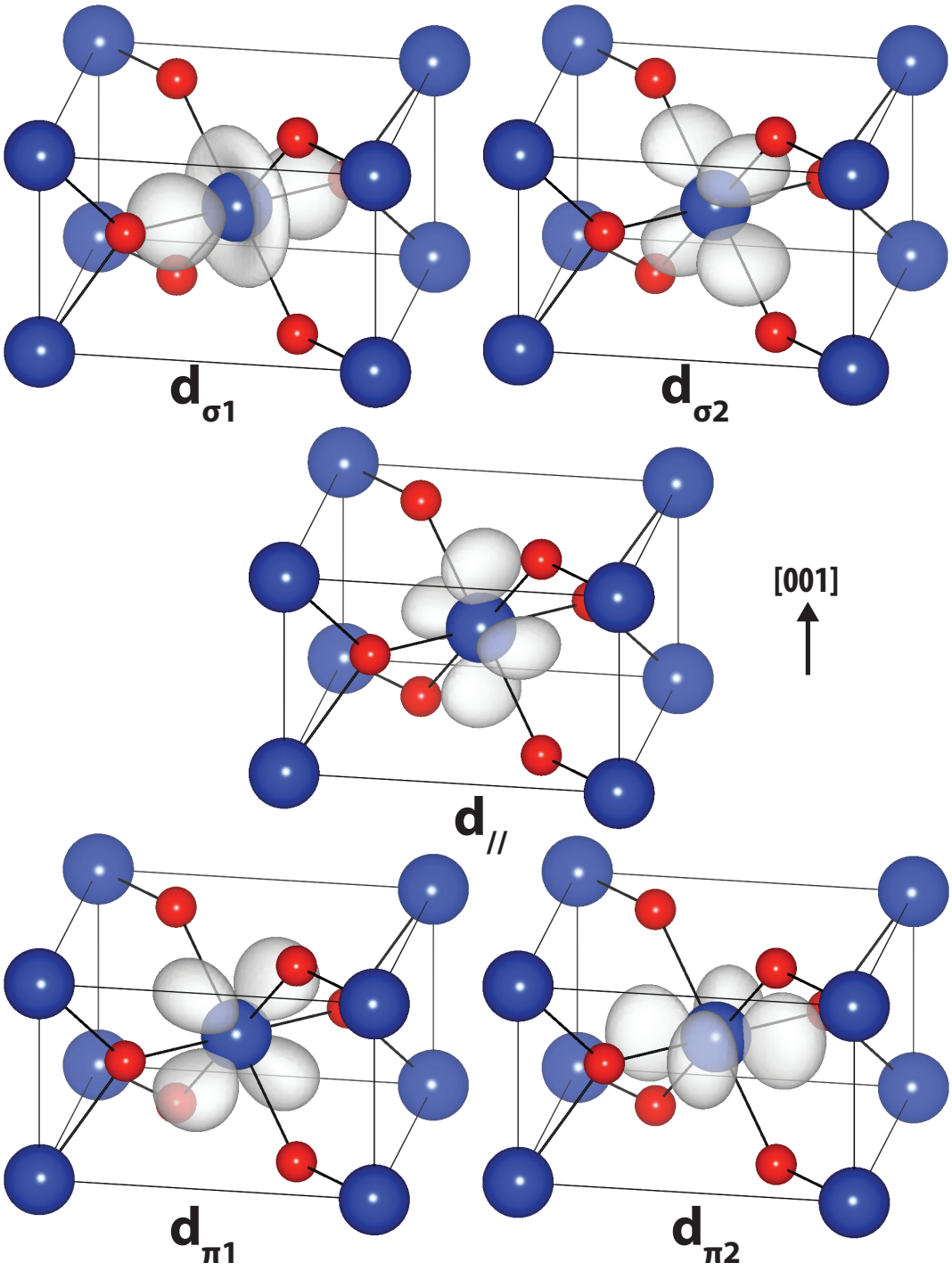

Figure 4.7: Sketch of the angular part of the transition metal d orbitals' charge densities. (The choice of axes and their naming follow Ref. [48, 68].) The red and blue atoms represent oxygen and metal ions respectively.

and its effect on the crystal structure.

The Fermi levels of the compounds that we consider, except for ZrO_2 and HfO_2 which are insulators, are located in the partially filled TM d bands. Sketches of the charge densities of the d atomic orbitals of a TM in the Rutile structure are shown in Fig. 4.7. For the choice of the naming of these orbitals, we follow Ref. [48] and [68]. Even though the oxygen octahedra are not regular in general, they are not too far from regular and so a splitting between the pseudo-e_g and the pseudo-t_{2g} orbitals of the TM cations can be seen in the density of states of all the compounds (not shown). $d_{\sigma 1}$ and $d_{\sigma 2}$ are σ bonding with oxygens and form the pseudo-e_g manifold. The pseudo-t_{2g} states $d_{\pi 1}$, $d_{\pi 2}$, and $d_{\|}$ are π bonding with oxygens and lie at lower energies than the pseudo-e_g states. From this point on, we drop the pseudo- prefix for brevity.

Due to the geometry of the Rutile phase, which involves edge-sharing octahedral chains, strong M-M interactions are possible between neighboring metal cations in the [001] direction [67]. The M-O bonding is mostly due to the e_g orbitals, but the M-M bonding is mostly due to the t_{2g} ones. In Fig. 4.8, we show the charge densities of the $d_{\|}$, $d_{\pi 1}$, and $d_{\sigma 2}$ orbitals, which have lobes extended along the [001] direction and as a result possibly contribute to the M-M bonding. $d_{\|}$ is σ bonding with the neighboring cations, whereas $d_{\pi 1}$ and $d_{\sigma 2}$ can form π bonds. However, in the early transition metals we consider, the formal occupation of the TM d orbitals is no larger than 6, as a result, the e_g manifold is unoccupied. In other words, the $d_{\sigma 1,2}$ states are pushed to higher energies than the Fermi level due to their hybridization with the oxygens. As a result, $d_{\sigma 2}$ orbitals cannot contribute to the M-M bonding.

It has been experimentally observed as early as 1962 that in the Rutile struc-

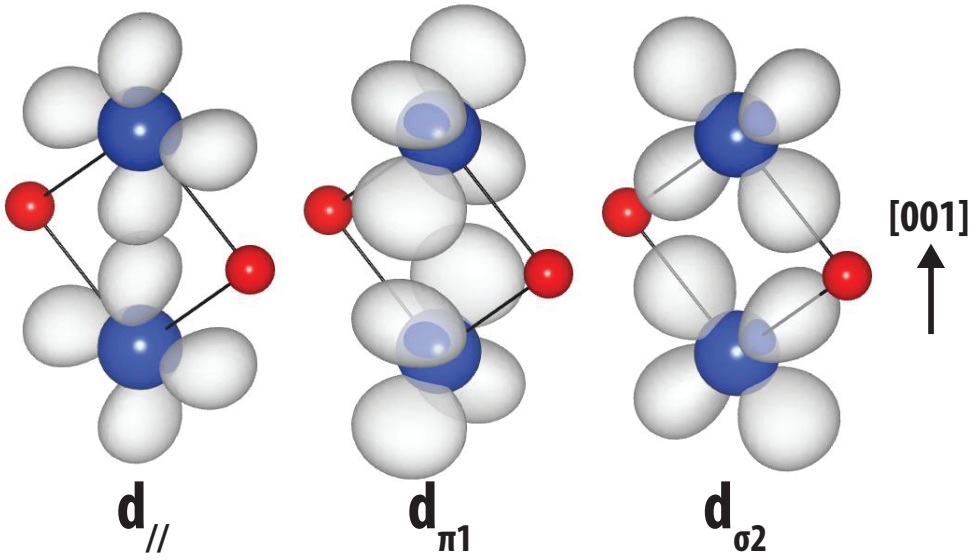

Figure 4.8: Sketch of the angular part of the charge densities of the three d orbitals which have overlapping lobes with the other metal cations. Red and blue atoms represent oxygen and metal ions respectively.

ture, the amount of electrons available for M-M bonding determines the c/a ratio [106]. Our present analysis emphasizes that this results in a decreasing trend in c/a up to 2 electrons on the d orbitals, because there are only two t_{2g} orbitals available for bonding. This is consistent with observations such as the absence of a triple M-M bond in TcO_2 [137], or between the Re ions in $La_4Re_6O_{19}$ and α-ReO_2 [152]. The first-principles results in Fig. 4.2c also agrees: d^1 compounds (NbO_2 and TaO_2) have smaller c/a ratios than the d^0 ones (ZrO_2 and HfO_2) because they have a metallic bond between neighboring cations in the [001] direction. d^2 compounds (MoO_2 and WO_2) have two orbitals which contribute to the metallic bonding, so they have an even smaller c/a ratio. The d^3 compounds (TcO_2 and ReO_2) do not have more than 2 metallic bonds, so their c/a ratio is not smaller than the d^2 compounds. Finally, d^4 and d^5 compounds (RuO_2, OsO_2, RhO_2, and IrO_2) have larger c/a ratios because of two reasons: *(i)* They have

more than three electrons on the TM cation, so the M-M anti-bonding orbitals are partially filled. *(ii)* The energy cost of having a smaller c/a ratio increases with larger number of electrons on the the orbitals due to the M-O interactions. The elastic moduli along the [001] direction is larger for d^4 and d^5 compounds, which supports this claim: The elastic moduli of MoO_2, TcO_2, RuO_2 and RhO_2 along [001] are 0.334, 0.332, 0.428 and 0.429 meV/Å^3 respectively.

4.6 Cation Pairing

In this section, we focus on the cation pairing by performing a group theoretical analysis and linear response calculations. We start by giving a brief introduction to the particular lattice modes in the high symmetry Rutile phase that are related to cation pairing in Section 4.6.1. Then, in Section 4.6.2, we present the results of linear response calculations, the Force Constants Matrix (FCM) eigenvalues. Compounds that exist in a distorted Rutile phase have at least one negative FCM eigenvalue (or equivalently an unstable phonon with imaginary frequency) which signal lattice instabilities. We discuss the microscopic mechanism behind these instabilities in Section 4.6.3. The structural ground state can be obtained by freezing in the unstable lattice modes and performing ionic relaxations in the resulting low symmetry phases. Results of such calculations, as well as a discussion of what determines the particular ground state structure that is observed, is presented in Section 4.6.4. Finally, in Section 4.6.5, we discuss whether the pairing instability is local; in other words, whether even a single cation pair can form a covalent bond and reduce the energy. We argue that the pairing instability has a cooperative character, such that multiple cation pairs need to be displaced coherently to reduce energy.

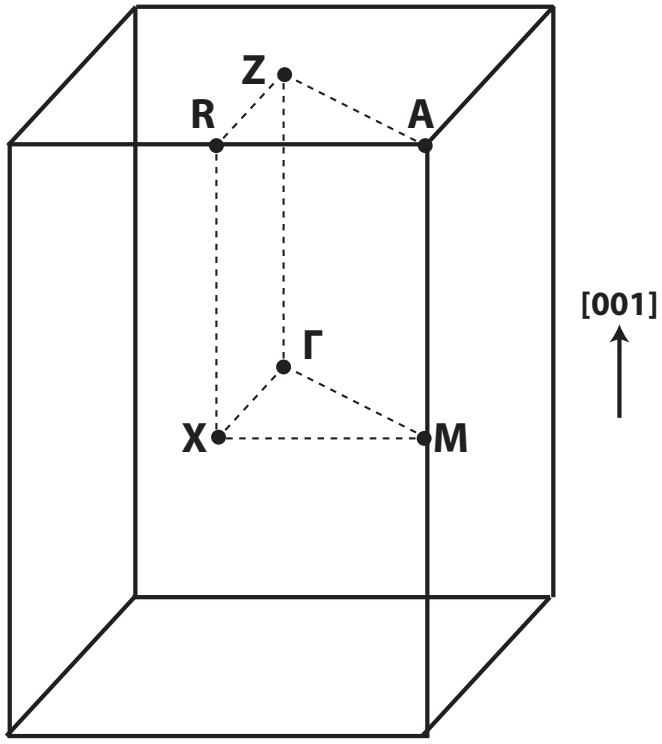

Figure 4.9: High symmetry q-points in the first Brillouin zone of simple tetragonal point group.

4.6.1 Symmetry Analysis of Cation Pairing in Rutile Structure

In this section, we consider the properties of pairing related phonon modes in the high symmetry Rutile phase, and the reduction of symmetry that these phonon modes lead to when they freeze in. The theoretical basis of this sort of symmetry mode approaches can be found in Ref. [156, 74, 130].

High symmetry Rutile phase is in a simple tetragonal space group, the reciprocal lattice of which is also simple tetragonal. The 1^{st} Brillouin zone is shown in Fig. 4.9. In a coordinate system where $\hat{z}$ is aligned with the [001] direction, the cartesian components of the six high symmetry q-points are

$\Gamma = (0,0,0)$, $X = (\pi/a,0,0)$, $M = (\pi/a,\pi/a,0)$, $Z = (0,0,\pi/c)$, $R = (\pi/a,0,\pi/a)$, and $A = (\pi/a,\pi/a,\pi/c)$. Since the cation pairing involves displacement of cations neighboring in [001] direction towards each other, the wavevector of the corresponding normal mode must have a z component that is equal to π/c. As a result, it is only the wavevectors on the *Z*-*A*-*R* plane that can be responsible of cation pairing. The MoO_2 structure is obtained by an *R*-point mode, whereas the NbO_2 structure involves a normal mode with a wavevector on the high symmetry line between *Z* and *R* points [61]. For simplicity, we limit our discussion to only the 6 high symmetry q-points shown in Fig. 4.9.

Any wavevector on the *Z*-*A*-*R* plane has an irreducible representation (irrep) that a normal mode that involves cations forming pairs along the edge sharing chains transforms as. The main difference between these irreps from a cation pairing perspective is the different pairing patterns that result from the difference in the in-plane components of the wavevectors. In Fig. 4.10a-c, the different pairing patterns for *A*, *R* and *Z* q-points are sketched. The irreps corresponding to these patterns are A_1, R_1^+, and Z_1. The A_1 and Z_1 irreps have three symmetry adapted modes each: one of these is the cation pairing, and other two are oxygen displacements. R_1^+, on the other hand, has a larger number of degrees of freedom: It has 6 symmetry adapted modes: one is cation pairing, three are oxygen displacements, and two are cation zig-zag displacements in the *x*-*y* plane. How this larger number of symmetry adapted modes might be the factor that determines the groundstate will be discussed in Section 4.6.4.

The lower symmetry structures that these phonon modes lead to are shown in Fig. 4.11. All three of the high symmetry pairing modes are at least doubly degenerate, and therefore they can lead to multiple different low symmetry

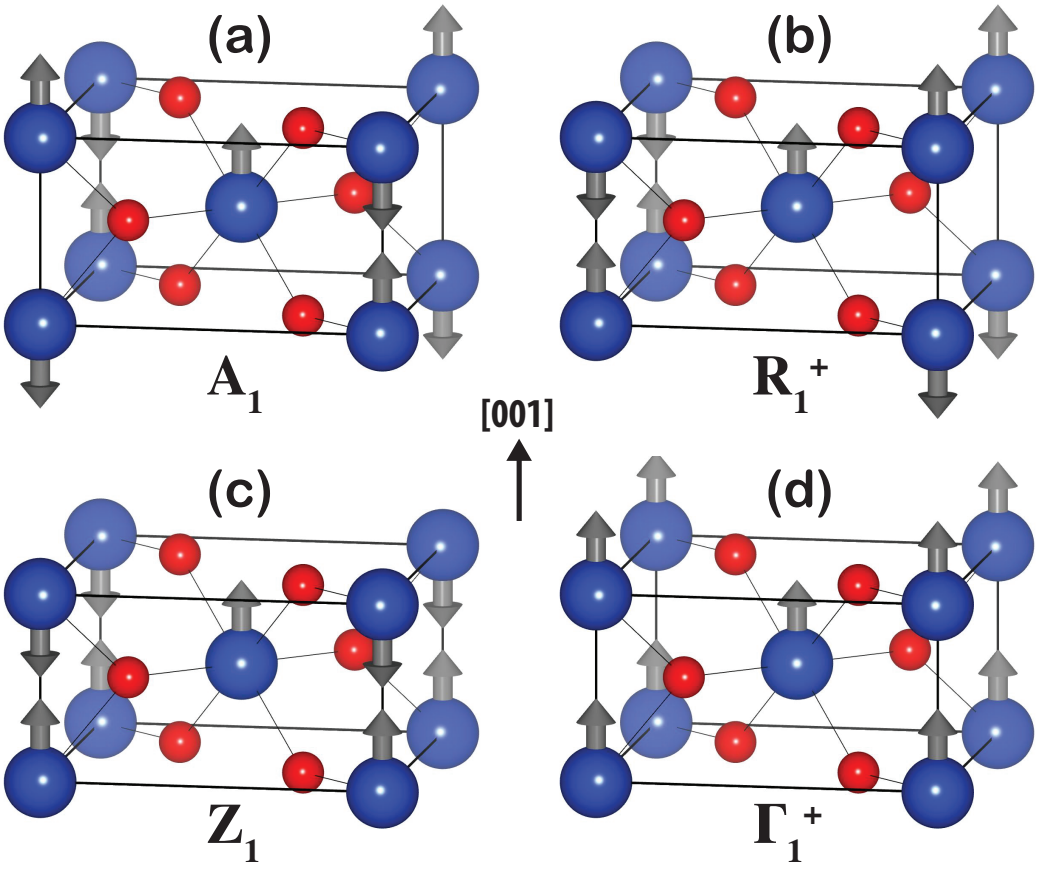

Figure 4.10: Sketches of the cation pairing patterns corresponding to A_1, R_1^+, and Z_1 irreps, and also the cation displacement pattern corresponding to the Γ_3^- irrep. Red circles represent oxygens, blue circles represent metal cations. For A_1, R_1^+, and Z_1 irreps, there are multiple possible directions, but only the high symmetry direction which gives the lowest energy is sketched in this figure. Also, only the cation pairing displacements are shown, and the displacements of the other symmetry adapted modes, such as oxygen displacements, are omitted for simplicity.

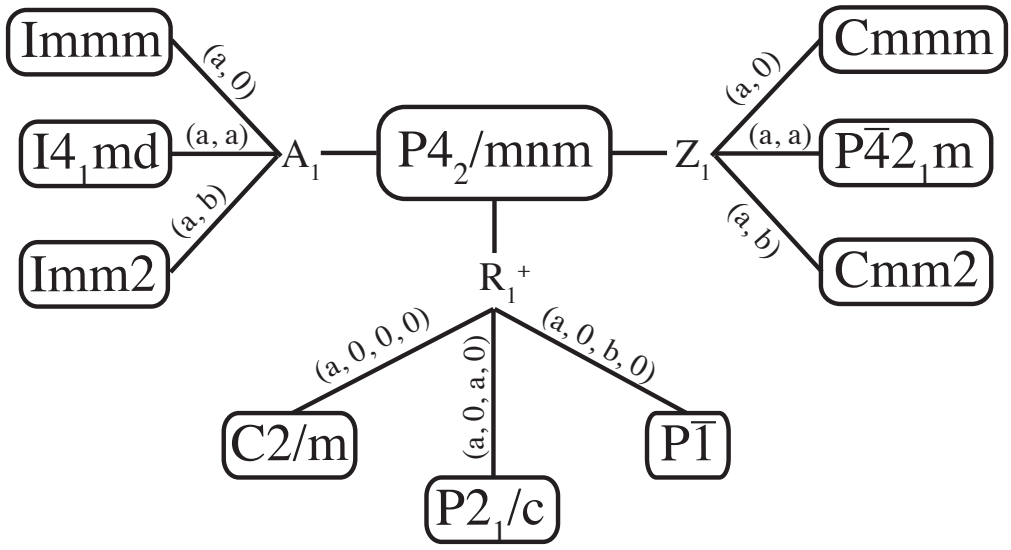

Figure 4.11: Unstable modes of the high symmetry Rutile structure and possible groundstates they can lead to. Only the subgroups that can be reached in a 4 formula unit supercell are listed. The MoO_2 structure $P2_1/c$ is obtained by the irrep R_1^+ along $(a, 0, a, 0)$ direction.

structures. We only consider the structures that require a supercell no larger than 4 formula units.

One last mode that is important for understanding the cation pairing is Γ_3^-, shown in Fig. 4.10d. Γ_3^- is one of the two infrared active irreps present in the simple tetragonal point group, and induces a polarization in the [001] direction. The importance of the optical mode that transforms as this irrep stems from its simplicity: It corresponds to an in-phase motion of all cations against the oxygens in the [001] direction. It does not involve any change in M-M distances or distortion of oxygen octahedra. The frequency of this mode is a pure measure of the energy cost of displacing the metal cations from the center of the octahedra. In this respect, it can be used as a quantitative measure of how much the oxygen matrix opposes the cation displacements, and hence, the cation pairing. (This

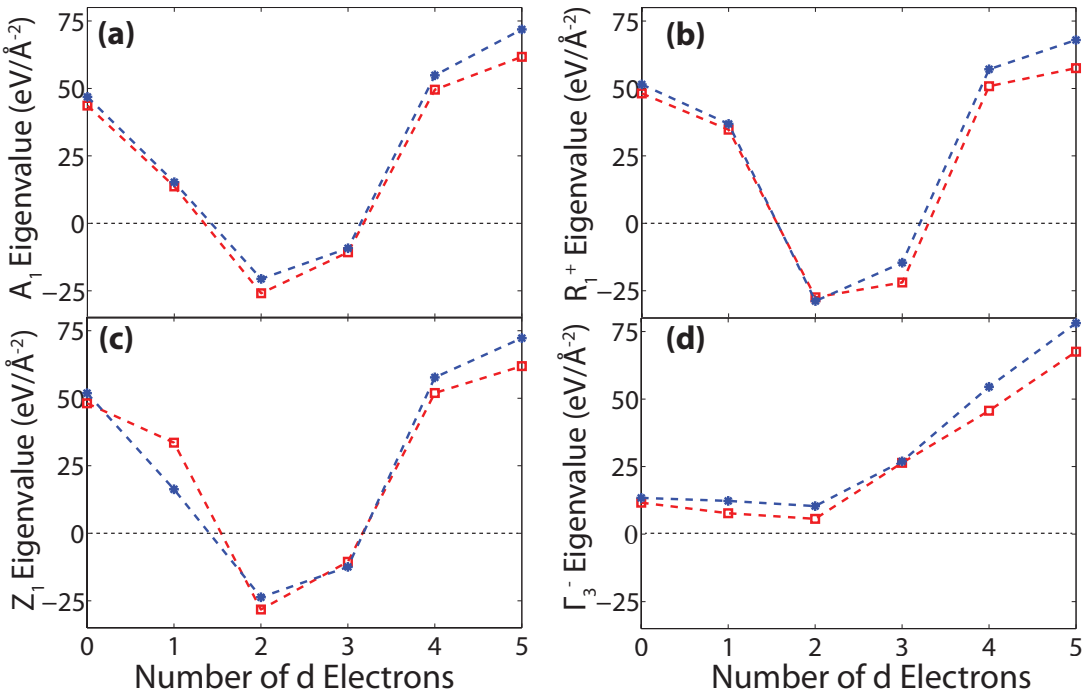

Figure 4.12: Force constants matrix eigenvalue of the normal modes with the largest cation pairing components for (a) A_1, (b) R_1^+, (c) Z_1 irreps. (d) The force constants matrix eigenvalue for the optical Γ_3^- mode. The red and blue data correspond to 4d and 5d cations respectively.

corresponds to the crystal field stabilization discussed in Ref. [137].)

4.6.2 Instabilities From DFT

In this section, we present the results of linear response calculations. We have calculated the force constants matrix (FCM) and the phonon frequencies by building supercells and using DFPT as implemented in VASP [13, 93, 92]. While the phonon frequencies, which are related to the eigenvalues of the dynamical matrix, can be used to study the lattice instabilities, in this study we prefer to

work with FCM eigenvalues and eigenvectors, since we are interested in the structures and structural transitions, but not the dynamics.

We calculated the FCM eigenvalues in all six high symmetry q-points of all the compounds by considering them in the high symmetry Rutile structure. Our results show that instabilities, which are signaled by negative FCM eigenvalues, exist on only the A, R and Z points, and only in the compounds that are reported to have a cation paired structure. The d^2 and d^3 compounds (MoO_2, TcO_2, WO_2, and ReO_2), which have the MoO_2 structure at all temperatures, have strong instabilities at A, R and Z points. NbO_2, which exists in a different cation paired structure, has a weak instability on only the R point. TaO_2, which has conflicting experimental reports about its structure, has no instabilities in the high symmetry q-points.

The displacement patterns corresponding to these unstable modes reveal that they transform as the three pairing related irreps considered in the previous section. Furthermore, their characters all exhibit a significant contribution from cation pairing. Except for in the d^1 compound NbO_2, the unstable FCM eigenvectors consists of 60% to 90% cation pairing component. This result is consistent with the experimental observation of a cation paired state at all temperatures in the d^2 and d^3 compounds. The instability of the d^1 compound NbO_2, on the other hand, is not as strong as the instabilities in these compounds. This is consistent with the fact that NbO_2 undergoes a transition to a cation paired state only at low temperatures.

In Fig. 4.12a-c, we plot the FCM eigenvalue C of the normal modes that have the largest cation pairing components on the A, R, and Z q-points. For all three high symmetry pairing irreps A_1, Z_1 and R_1^+, the eigenvalue C not only depends

on the number of d electrons, but also has a very similar trend for both 4d and 5d compounds. This suggests that the driving force of the pairing instability is the electronic structure of these compounds. Also note that the value of the FCM eigenvalues are very similar for all three pairing related irreps. This observation, and the fact that all of the unstable eigenmodes for d^2 and d^3 compounds have large cation pairing components suggest that it is the cations' tendency to displace and pairs that drives the instabilities. This will be discussed further in the following section.

The FCM eigenvalue for the Γ_3^- optical mode is shown in 4.12. Like the pairing modes, Γ_3^- has a strong dependence on the number of outer shell d electrons, and its trends are very similar for $4d$ and $5d$ compounds. The force constant C corresponding to Γ_3^- is small and relatively constant for d^0 to d^2. For 3 or more electrons it increases rapidly and gets ~ 5 times larger for d^4 and d^5 compounds. The importance of this result in the suppression of pairing instabilities in these compounds will be discussed in the following section.

4.6.3 Mechanism of Pairing

In the high symmetry Rutile phase, there are metallic bonds between the metal cations in the edge-sharing octahedral chains. Cation pairing is unfavorable for these bonds since it causes half of the M-M distances along each chain get larger. Furthermore, pairing displaces the cations from the center of the oxygen octahedra, which is also unfavorable because of the M-O interactions. However, a cation paired state can be nevertheless favorable if covalent M-M bonds are formed as a result of it [67, 68]. This can explain the instability towards a

cation paired state in Rutile compounds with a nonzero number electrons on the outermost d shell of the M cations.

The trend observed in the pairing modes' force constants eigenvalues (C) (Fig. 4.12a-c) can be explained by a competition of the M-M covalent bond formation and the M-O interactions. d^0 compounds do not have a tendency to form cation pairs since there are no d electrons to form M-M bonds. d^1 compounds have smaller C compared to d^0 compounds because they have an electron that can form a M-M bond, however, the energy gain of this single bond is not large enough to overcome the energy cost due to unfavorable M-O distances, and as a result, C is not negative. Cost of displacing the d^2 cations from the center of the octahedra are similar to that of d^1 compounds, as evidenced from the force constant of the Γ_3^- mode. But these compounds have two electrons that can form covalent bonds, and as a result, have strong pairing instabilities. d^3 compounds can also form 2 covalent bonds, however, the M-O interactions lead to a higher energy cost of displacing these cations from their high symmetry positions as seen in the trend of Γ_3^- force constant. The reason of this is that the t_{2g} orbitals are half filled, and as a result, when the octahedral coordination of the metal cation gets more irregular, the d electrons cannot reduce the energy by changing their distribution as much as they can when t_{2g} orbitals are less than half filled. d^4 and d^5 compounds can in principle form M-M covalent bonds, however, there are more than three d electrons per ion and as a result the antibonding M-M states are filled as well. Also, these compounds have a huge energy cost associated with displacing the metal cation from the center of the octahedra, as seen in the FCM eigenvalue of the Γ_3^- mode; because the M ion's t_{2g} states are more than half filled. As a result, any pairing instability is suppressed, and they have a very large and positive force constant associated with the pairing modes. This

is in line with Burdett et al.'s observation that the local M-O interactions can stabilize the high symmetry structures without cation pairing, even in compounds with d electron counts suitable for M-M pairing [33, 34].

As a summary, we have explained the tendency of the early $4d$ and $5d$ TM oxides in the Rutile structure to distort and have a cation paired state by a competition of the energy gain from metal ions' forming covalent M-M bonds, and the energy cost of displacing the metal ions from the center of the octahedra. Both of these quantities strongly depend on the number of d electrons in the outermost shell of the M cation. This gives rise to the nonmonotonic trend observed in Fig. 4.12.

4.6.4 Structural Groundstate

The multiple unstable lattice modes in the high symmetry Rutile phase lead to various possible structural groundstate candidates for NbO_2, MoO_2, TcO_2, WO_2, and ReO_2 (Fig. 4.11). In order to determine the groundstate of these compounds, we perform ionic relaxations with various pairing patterns frozen in, in other words, in different space groups listed in Fig. 4.11. Energy gains of different structures with respect to the high symmetry Rutile phase, obtained from these relaxations that optimize the cell vectors as well as the internal coordinates, are presented in Figure 4.13a. The structure that has the largest energy gain is the groundstate structure. All compounds with instabilities have the same structural groundstate, $P2_1/c$ (#14), which is connected to the high symmetry Rutile structure via the irrep R_1^+. This is the MoO_2 structure which is the experimentally observed structure of MoO_2, TcO_2, WO_2 and ReO_2, so our results

are consistent with experimental observations for these compounds.[2] While our procedure cannot reproduce the correct low temperature structure for NbO_2, since the NbO_2 structure ($I4_1/a$) involves a distortion corresponding to a normal mode that is not on a high symmetry point; the result is consistent with the experiments in that a distorted Rutile phase is predicted. For the d^4 and d^5 compounds we observe no instabilities, which is in line with the fact that these compounds are observed in a high symmetry Rutile phase at all temperatures. Finally, the d^0 compounds, which are yet to be synthesized in a Rutile related structure, exhibit no instabilities in this structure according to our calculations.

One question that arises at this point is: *Why is the groundstate $P2_1/c$, i.e. why does the R_1^+ mode lead to a larger energy gain compared to the A_1 and Z_1 modes?* In other words, why is a certain cation pairing pattern is favored to the other ones? The three possible explanations for this are: (i) The coupling with strain, (ii) the interactions between the next nearest neighbor cations, or (iii) the effect of surrounding oxygens.

The simplest explanation is the coupling of the normal modes with strain: The normal mode that leads to the largest energy gain when coupled to strain could be the groundstate, as has been observed in other pairing driven phase transitions [171]. In order to see whether this is the reason in the present compounds, we repeat the ionic relaxations in different space groups, but this time keeping the cell vectors fixed to those of the high symmetry Rutile phase. This way, the effect of strain is zeroed out, and the energy gain for each mode in the

[2]There is a misunderstanding in the literature [48] that the MoO_2 structure is obtained from the high symmetry Rutile structure via two distinct modes, namely the cation pairing and a lateral zig-zag displacement of the M cations. However, we find that it is a single normal mode, i.e. a single irrep, that connects the MoO_2 structure to the high symmetry Rutile phase. The cation pairing and zig-zag distortions are just different components (i.e. symmetry adapted modes) of this single mode.

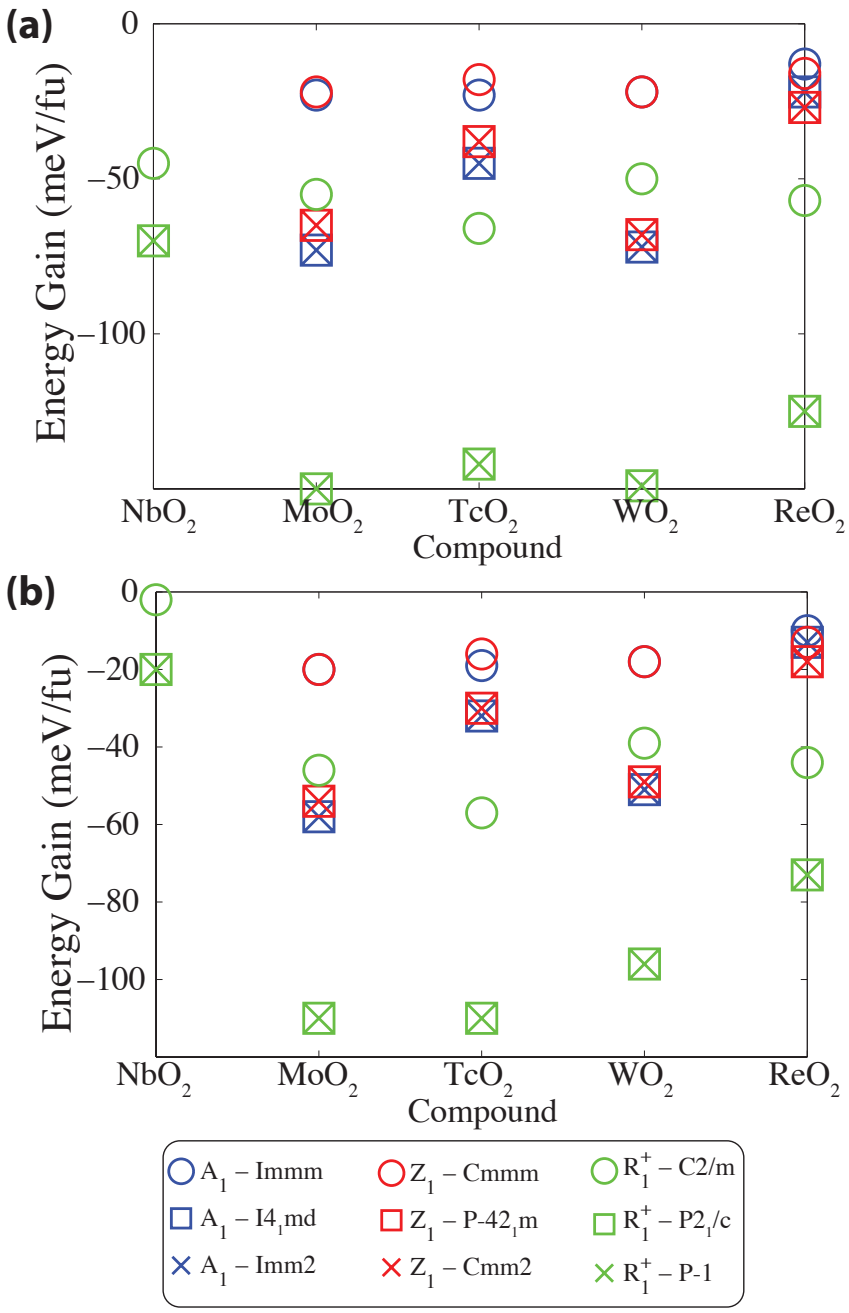

Figure 4.13: Energies of structures in different spacegroups with respect to the nondistorted Rutile structure. The normal modes and the spacegroups that they lead to are given at the legend. (a) Results of full geometric relaxations, which include the optimization of the cell shape and volume as well as the ion coordinates. (b) Results of relaxations made with fixed lattice vectors.

absence of coupling to strain is calculated. The results of these calculations, presented in Figure 4.13b, show that the groundstate structure is the same even in the absence of strain energy gain. As a result, the strain-coupling cannot be the factor that determines the lowest energy structure.

The second possible reason for the observed pairing pattern is that the cations in neighboring octahedral chains interact with each other in a way that favors the particular pairing pattern observed. In order to test whether this is the case, we calculate the energy gain due to cation pairing with the R, A and Z wavevectors for different amplitudes of displacement. The results are presented in Fig. 4.14a for MoO_2. For these calculations, only the cation pairing distortion is considered, and the other components of the FCM eigenvectors are not taken into account. (So, for example, the oxygen ions are not displaced.) The resulting maximum energy gains (obtained from the minimum point of the energy well) are of similar magnitude for all three pairing patterns, and even more, Z_1 is more favorable than R_1^+. Thus we conclude that the reason that the R_1^+ modes lead to a higher energy gain is not because of the preference for a certain cation pairing pattern and thus cannot be explained by the interaction between M cations. The other components of the normal modes, such as the oxygen displacements, are of importance in determining the lowest energy structure. In order to see the magnitude of the effect of these other components, in Figure 4.14b the amplitude of pairing and energy gain are plotted also for structures that are relaxed (circles). The difference between the lowest points on the energy curves, which correspond to the largest energy gain that can be obtained by only pairing, and the energy of the relaxed structure measures how much energy is gained by the components other than pairing. These components are not unstable by themselves, i.e. their self-force constants are always positive, and is possibly quite

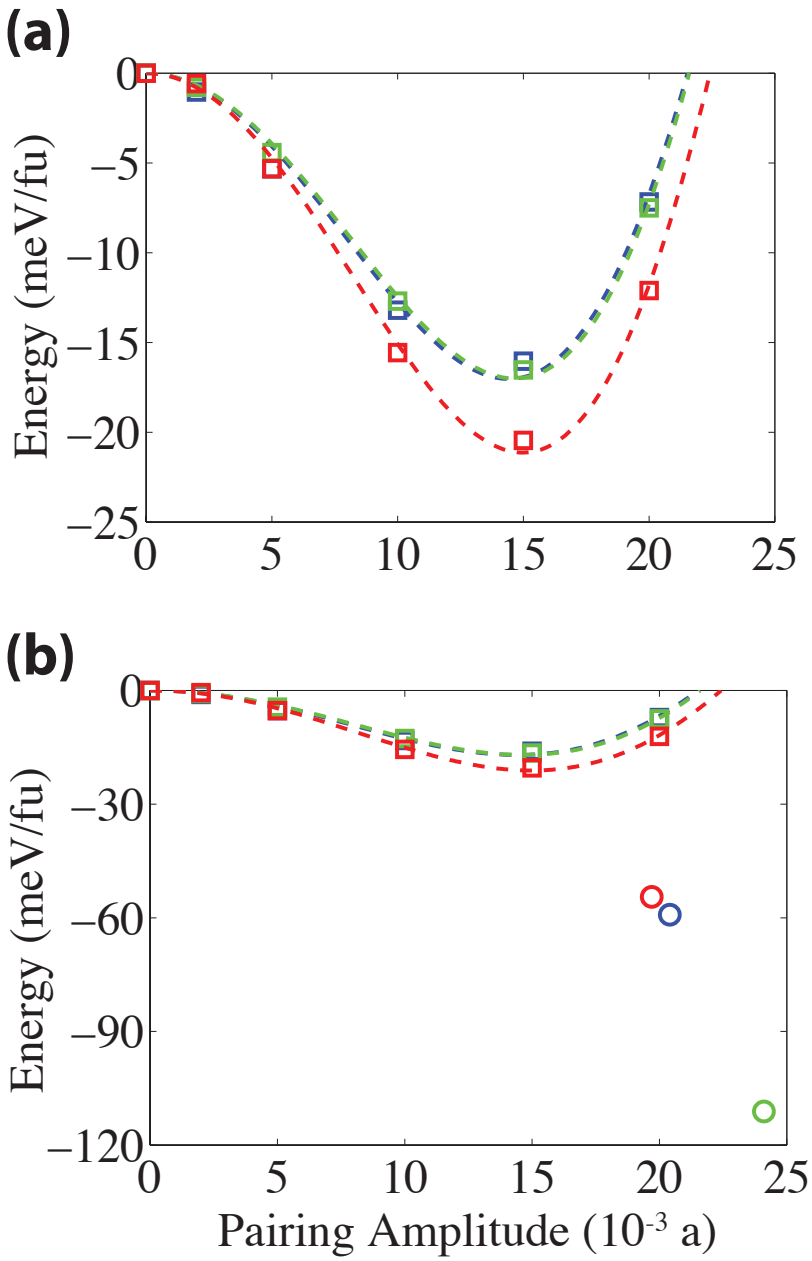

Figure 4.14: (a) Pairing amplitude vs. energy gain for wavevectors *R* (green), *A* (blue) and *Z* (red). The data points are from first principle calculations, and the dashed lines are a 6th order fit to the data. Amplitude of pairing is given in terms of the lattice constant *a*. (b) Curves are the same as (a). The circles correspond to the energy gain and pairing amplitude for the structures with relaxed ionic coordinates in the spacegroups with R_1^+ (green), A_1 (blue), and Z_1 (red) modes frozen in.

large. However, they nevertheless lead to a very large energy gain by their coupling to the pairing distortion.

When cations are displaced to form pairs, the M-O bonds become unfavorable. The only remaining explanation for the fact that the R_1^+ mode can decrease the energy more than the A_1 and Z_1 ones is because R_1^+ reduces the stress on these unfavorable M-O bonds better than A_1 and Z_1. While there is no obvious explanation of why this is the case, it is not surprising because of the higher number of degrees of freedom that R_1^+ provides. This point can be made clear by considering the Landau free energy of a system with two modes, one of which is unstable.

Consider two symmetry adapted modes, P and Q, which transform as the same irrep, such that P is unstable but Q is not. (In the case of, for example, MoO_2, P would be the cation pairing and Q would be an oxygen displacement or a cation zig-zag displacement.) As P is unstable, one should consider terms up to 4^{th} order in P in the Landau free energy. However, since Q is hard, it is usually sufficient to go up to only second order in Q. So, the free energy F around the high symmetry structure can be written as

$$F = \alpha_P P^2 + \beta_P P^4 + \alpha_Q Q^2 + \gamma PQ. \tag{4.4}$$

Here, α_P is negative whereas α_Q is positive. Going upto only the second order in Q is equivalent to assuming that Q is considerably smaller than P. (Exceptions to this occur when a large amplitude of a hard mode is observed in the ground state of a material. Such cases do not invalidate the present argument.) Since P and Q transform as the same irrep but are not eigenmodes, there is a bilinear coupling (γ) between them, but higher order couplings such as $\sim P^3Q$ or P^2Q^2 can be omitted since they are smaller than $\sim P^4$.

Minimizing F with respect to ϕ gives

$$Q = -\frac{\gamma}{2\alpha_Q} P, \tag{4.5}$$

which, upon substituting in Eq. 4.4 results in

$$F = \alpha_P P^2 + \beta_P P^4 - \frac{\gamma^2}{4\alpha_Q} P^2. \tag{4.6}$$

Given that α_Q is positive, the last term is necessarily negative. In other words, even though it is not unstable, Q leads to an energy gain second order in P.[3] Thus, we can say that any hard mode that transforms as the same irrep as a soft mode necessarily leads to an energy gain in the groundstate.

As discussed in Section 4.6.1, A_1 and Z_1 irreps have three symmetry adapted modes. So, there are only two symmetry allowed oxygen displacements that can relieve the M-O bonds in the structures reached by these irreps. R_1^+, on the other hand, has six symmetry adapted modes. So, R_1^+ has five hard symmetry modes that can couple to the cation pairing and lead to an energy gain playing the role of Q in the example above; whereas A_1 and Z_1 have only two such modes. If the coupling constants (γ) between these symmetry adapted modes and the unstable cation pairing symmetry adapted mode are of similar magnitude, then R_1^+ will lead to a higher energy gain in second order thanks to the coupling of the cation pairing distortion with the hard components. The Baur distortion indices and bond angle variances of TcO_2, listed in Table 4.6.4, also support this scenario: Among the different groundstate candidates, $P2_1/c$ (reached by R_1^+) has the smallest Baur index, so the most favorable M-O distances. However, it has the largest bond angle variance, which shows that the oxygen octahedra is distorted most in this spacegroup to have favorable M-O distances. The results for the other compounds are similar.

[3]This energy gain should not be confused with a decrease in the FCM eigenvalue because here the hard mode Q is assumed to be fully relaxed.

	Baur Distortion Index	Bond Angle Variance
$P4_2/mnm$	0.016	2.4
A_1 - $I4_1md$	0.020	3.2
R_1^+ - $P2_1/c$	0.011	4.9
Z_1 - $P\bar{4}2_1m$	0.015	3.2

Table 4.2: Baur distortion indices and bond angle variances of fully relaxed TcO_2 for different groundstate structure candidates. Spacegroups $I4_1md$ and $P\bar{4}2_1m$ have two inequivalent octahedra - the numbers reported for these spacegroups are the average values.

We emphasize that the argument presented here is nothing but an plausibility argument and is not supported by conclusive evidence. Even though Baur distortion indices etc. are in line with these claims, it is possible that the coupling strength γ is very different for different modes/compounds.

In summary, the groundstate structure is determined by an interplay of multiple effects: The compounds with nonzero d electrons on the metal cation tend to form covalent M-M bonds and hence have a tendency toward a cation paired state. The M-O interactions, which favor a symmetric environment around the metal cation, oppose to this pairing. As a result, only some of the compounds have a pairing instability. Among the multiple possible groundstate structures, the groundstate is the one that allows the largest number of degrees of freedom to relieve the stress on the M-O bonds.

4.6.5 Is the Pairing Instability Cooperative?

A question that our analysis so far does not answer is whether the pairing instability in the d^2 and d^3 compounds is local; in other words, whether a single pair of M cations can reduce the energy by displacing towards each other and

forming a covalently bonded pair. As early as 1960, Goodenough explained the possibility of cooperative vs. noncooperative pairing in TM oxides with edge- or face-sharing octahedral chains. If the pairing is a noncooperative, local phenomenon, then an individual pair of cations can be displaced and lower the energy. However, there is no consensus on whether the pairing in Rutiles is cooperative or not in the literature. There are multiple studies which approach the pairing from a Peierls point of view, which implies a cooperative character (For example [16, 66, 50, 47, 48, 49, 170, 12]). On the other hand, many authors have referred to covalent bonds between cations, which implicitly points to a local picture (For example [137, 25]). This far, we have been referring to the formation of covalent bonds as the driving force of instability as well; however, we considered instabilities only in the context of collective normal modes. So we need other calculations to figure out whether the instability has a local, noncooperative character.

In this section, we focus on MoO_2 to extract a coherence length scale which quantifies how local the pairing instability is [63, 23]. If the instability is purely local, then a single pair of cations can lower the energy, and the coherence length is a single lattice constant (c). We build a 1×1×32 supercell, which has 64 formula units. We then calculate the self force constant for an ionic displacement that involves pairing of $2n$ neighboring cations. For example, $n = 1$ corresponds to only two cations being displaced (Fig. 4.15a, left panel) in the $1 \times 1 \times 32$ unit cell, $n = 2$ (Fig. 4.15a, right panel) corresponds to four neighboring cations pairing, etc. The force constants are plotted in Fig. 4.15b. The force constant is positive for $n = 1$, i.e. a single pair of atoms cannot lower the energy by pairing. This indicates that the instability is not purely local. As expected, the force constant decreases with increasing n, and is negative for $n > 2$: three neighboring pairs

of metal cations can for dimers and decrease their energy. However, this does not necessarily mean that the coherence length for MoO_2 is three unit cells: the force constant keeps on decreasing even for $n = 8$, which is the largest length we can go up to in a $1 \times 1 \times 32$ supercell. This indicates that the cations have long range interactions, and while 3 neighboring pairs are sufficient to decrease the energy, energy decrease per pair is larger if a larger number of cations form bonds cooperatively.

Does this mean that the covalent bonding of metal cations, which is a local phenomenon, is not the driving force behind the pairing instability? The answer is negative. While covalent bonds are indeed local and the resulting energy gain would not depend on the neighboring cations' behavior, in order to form a covalent bond the cations break the metallic bonds they have in the high symmetry Rutile phase. Since the electrons in metal bands are delocalized; when a single pair of metal cations break the metallic bond, there is an energy cost due to multiple electrons. As a result, the system needs to build multiple covalent bonds in order to overcome the energy cost of breaking the metallic bonds and decrease its energy.

As a summary, we showed that the cation pairing instability in MoO_2 has a cooperative character with a coherence length larger than ~ 8 unit cells along the edge sharing chains. The reason of this cooperative behavior is that in order to make up for the energy cost of localizing electrons, multiple covalent M-M bonds need to be formed.

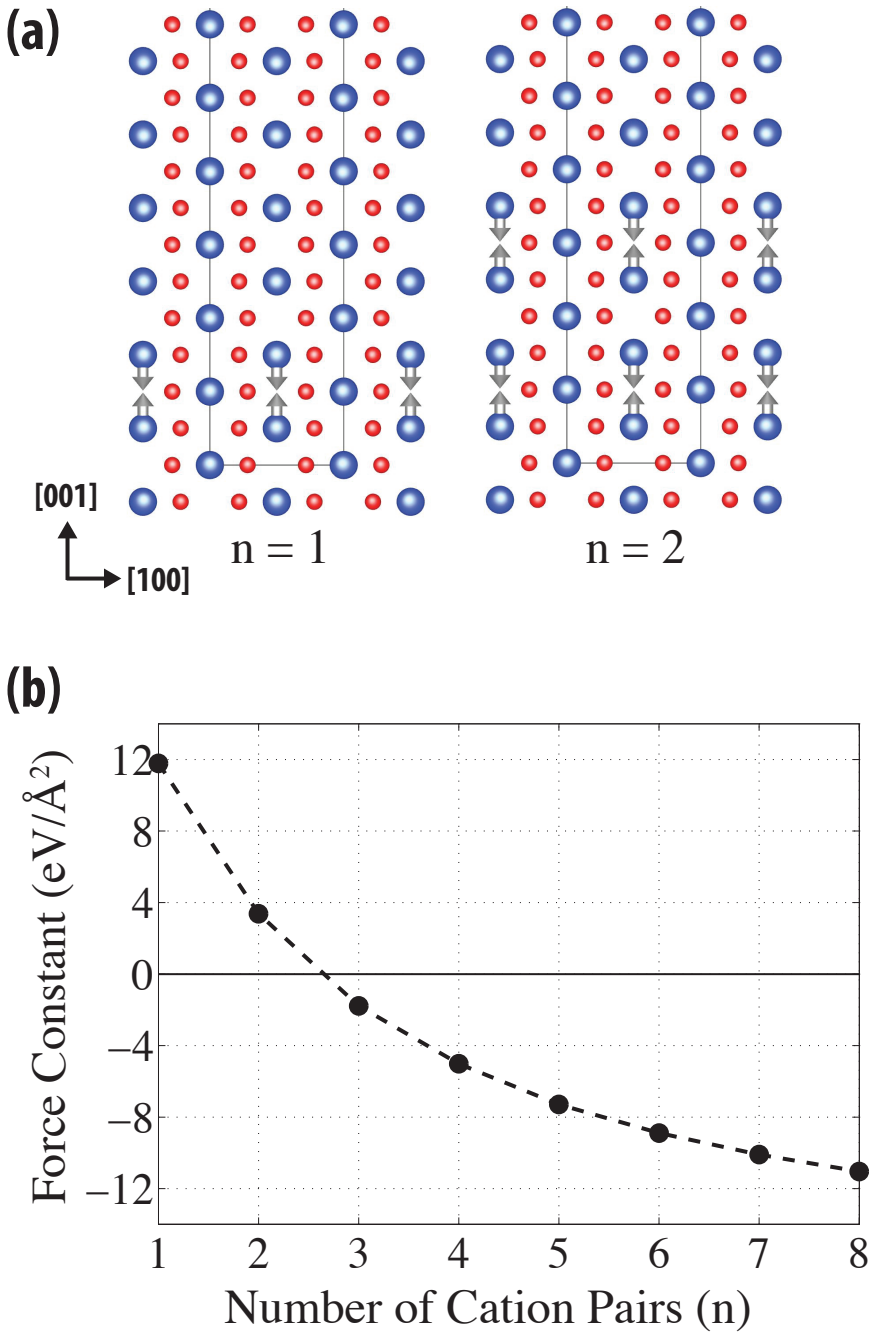

Figure 4.15: (a) Local cation pairing distortions with $n = 1$ (left) and $n = 2$ pairs of cations along the edge-sharing chains being displaced. The calculations are performed in a $1 \times 1 \times 1$ supercell, as a result, the displacements have $\vec{k} = (0, 0, \frac{\pi}{32c})$. (b) Self force constants of cation pairing displacement with respect to the number of cation pairs displaced along the [001] direction (n).

4.7 Summary & Conclusions

We presented a comprehensive and systematic study of the early 4d and 5d TM oxides in the Rutile related structures using first-principles computational tools. We studied the structural trends in the high symmetry Rutile phase of these compounds in detail with the aim of shedding light to how the steric, electronic and local bonding effects determine the structure of these compounds. We performed linear response calculations aided with a group theoretical analysis to understand the cation pairing tendencies, and discussed the underlying mechanisms. We also analyzed the effect of the oxygen anions, which not only suppress the cation pairing in d^4 and d^5 compounds, but also determine the particular groundstate structure (the MoO_2 structure, spacegroup $P2_1/c$) of the d^2 and d^3 compounds. We hope that the present study will fill the gap between various first-principles studies that focus on single compounds and provide a unified understanding of the structures of 4d and 5d TM dioxides in Rutile related phases.

4.8 Appendix: The Baur Distortion Index and The Bond Angle Variance

Two important measures that can be used to quantify how distorted the oxygen octahedra in TM oxides are the Baur Distortion Index and The Bond Angle Variance [14, 136]. The Baur Distortion Index B is defined as

$$B = \sum_{i=1}^{6} \frac{|d_i - d_M|}{6 d_M} \tag{4.7}$$

where d_i is the i^{th} Metal-Oxygen bond length, d_M is the average of d_i [14]. B is a dimensionless quantity that measures the width of the distribution of M-O bond lengths. It is zero for a regular octahedron with equal bond lengths, however, it is also zero for a non-regular octahedron with equal bond lengths but very different O-M-O bond angles. In order to measure the variation of bond angles, the Bond Angle Variance σ_θ is defined as

$$\sigma_\theta^2 = \sum_{i=1}^{12} \frac{(\theta_i - 90^\circ)^2}{11} \tag{4.8}$$

where θ_i is the i^{th} O-M-O bond angle [136]. σ_θ is zero for a regular octahedron with all O-M-O angles equal to 90°, but carries no information about the variation of bond lengths. So, it is complementary to B as a measure of how regular the octahedra are.

CHAPTER 5

CONCLUSIONS

This thesis constitutes an attempt to advance the understanding of the physics of Transition Metal (TM) Oxides. The interest in TM oxides is still increasing, as seen in Fig. 5.1, and we hope that this work is an incremental advancement in this field. While it is focused on only a particular group of compounds, and certain phenomena such as ferroelectricity or the magnetoelectric effect; the approaches used here can be applied to other compounds and other phenomena involving structural dynamics and phase transitions. In this section, we conclude by commenting what else can be done to contribute further in the directions taken in this work.

While not all possible TM oxide compounds are neither synthesized nor theoretically studied, there are other similar families of solid state compounds that deserve attention. TM Fluorides is an example. These compounds have fluorine instead of oxygen, and are more ionic due to the higher electronegativity of fluorine compared to oxygen. (Fluorine is immediately to the right of oxygen on the periodic table.) There also exist TM Oxyfluorides, which are transition metal compounds with both oxygen and fluorine ions. These compounds exhibit properties between those of oxides and fluorides given the intermediate amount of ionicity they have. Crystal structure families, such as Ruddlesden-Popper or Dion-Jacobson phases, are very commonly observed in these compounds as well [166] and as a result the information and intuition gained from TM Oxides can be immediately used to study both Fluorides and Oxyfluorides. We believe that these areas have many open problems and we will witness significant advances and discoveries involving these compounds.

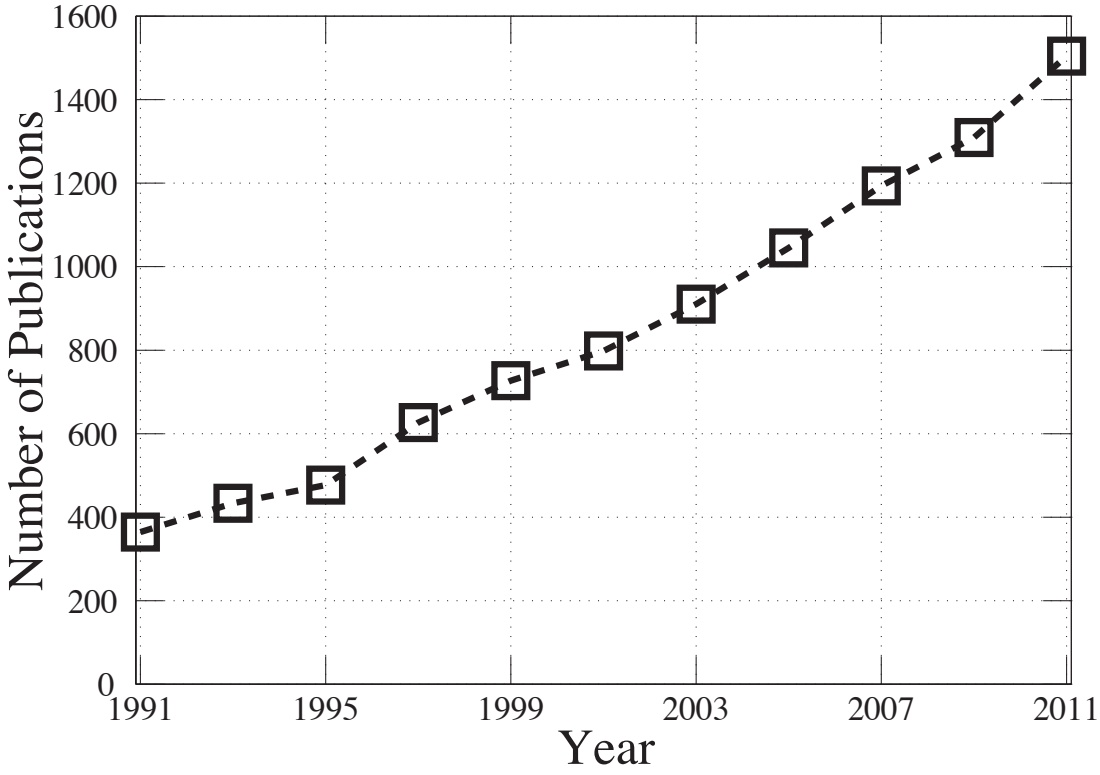

Figure 5.1: Number of publications in the Web of Knowledge that have 'transition metal oxides' as their topic. Data is obtained by averaging citations in two consecutive years.

Instead of moving horizontally on the periodic table, one can also consider moving down from oxygen to sulfur, selenium, or tellerium, and hence consider TM Chalcogenides. Replacing oxygen with other chalcogens and finding systematic trends can be used to gain insight about the physics of these materials. An example of work in this line is the seminal paper by Kasuya on the magnetic exchange mechanisms in Europium Chalcagonides [85].

The macroscopic phenomena we focused on, namely ferroelectricity, magnetoelectric effect, and the multiferroicity are very important in their own rights as well. Be it in the TM Oxides or other compounds, both the fundamental understanding and materials realizations of these phenomena are of utmost impor-

tance. The possible technological applications of ferroelectric, multiferroic and magnetoelectric materials are numerous and can be the topic of separate PhD theses. However, while some commercial applications of ferroelectricity exist, the coupling of magnetism and electric polarization is not used in any real world devices. While the magnetoelectric material we considered, $EuTiO_3$ is not particularly fit for such a purpose due to the low ordering temperatures involved, the search for and analysis of magnetoelectrics and multiferroics are still going on. We hope that the understanding about $EuTiO_3$ that we presented here will pave the way for the predictions of new magnetoelectric and multiferroic materials. Our results about the novel polar phase in Sr-Ti-O Ruddlesden-Popper compounds, on the other hand, are of more practical relevance. The experimental measurements are promising, and with the further advance of commercial Molecular Beam Epitaxy systems these materials can be mass produced and may find widespread use in electronic devices.

Our study on the structural trends of Rutile compounds provides an understanding of the various effects that compete to determine the crystal structure. The results of and the understanding gained from this study can be used to predict the properties of heterostructures built from these compounds. Given the need of new catalyst and catalyst support materials for applications such as water-splitting by sun light, and the suitability of oxide compounds for these purposes, we believe that TM dioxides with Rutile and related structures will attract a lot of well deserved attention in the near future.

While the work presented in this thesis is not the first application of the methods used in it, it supports the validity of these methods applied to these systems. The combination of first-principles Kohn-Sham DFT approaches sup-

ported by a symmetry analysis of the structures and the structural distortions (that uses the point and space groups as well as the representation theory for the lattice distortions) has proved very successful. Both the PAW formalism and the DFT+U method are very well established, and are standard tools used in the fields of solid state physics and materials science. The use of Wannier functions are also very widespread, and they are used for the study of multiple phenomena from magnetism to Fermi surface effects [110]. The way that the evolution of hybridization between ions with changing local correlation strength (U) is made explicit by considering the Wannier functions is, to the best of our knowledge, achieved for the first time in the present work. In this respect, it can be considered as a contribution to the possible uses of Wannier functions.

The future of this kind of studies will certainly involve alternatives to the simple LDA/GGA+U framework used here. This is related with not only the increasing computer power, but also improving methodologies. The hybrid functionals are already finding very common use, and we hope that the meta-GGAs will soon become a standard tool used in the community. Each of these methods catch some physics beyond LDA/GGA and therefore are necessary for the observation of certain phenomena in first principles calculations. Another method that builds upon the first-principles LDA/GGA calculations but imposes electron correlations to a better extend is the Dynamical Mean Field Theory (DMFT) [60, 91]. This method has been studied for a long time in model Hamiltonians, but it recently started to be applied to real materials in conjunction for Kohn-Sham DFT. This provided the opportunity to study phenomena for which both the material specific details and the electronic effects well beyond LDA, GGA, or Hartree-Fock methods are important; such as the volume collapse of rare-earth elements. DFT+DMFT provides a very suitable method to study phases

where structural distortions' interplay with the dynamical electronic effects are important, such as the site-selective Mott phase predicted in Nickelates [124].

In summary, we believe that while the compounds and the macroscopic phenomena considered in this work are important for both physical understanding and technological applications, and while the methods used are well suitable for studying these phenomena to a good extent, there is much room for further studies both on new compounds and using new methods. The first-principles computational methods brought a new point of view to both solid state physics and materials science. In the future will there certainly be new paradigm shifts driven and supported by these methods.

BIBLIOGRAPHY

[1] Hirofumi Akamatsu, Koji Fujita, Hiroyuki Hayashi, Takahiro Kawamoto, Yu Kumagai, Yanhua Zong, Koji Iwata, Fumiyasu Oba, Isao Tanaka, and Katsuhisa Tanaka. Crystal and electronic structure and magnetic properties of divalent europium perovskite oxides $eumo_3$ (m = ti, zr, and hf): Experimental and first-principles approaches. *Inorganic Chemistry*, 51(8):4560–4567, 2012.

[2] Hirofumi Akamatsu, Yu Kumagai, Fumiyasu Oba, Koji Fujita, Hideo Murakami, Katsuhisa Tanaka, and Isao Tanaka. Antiferromagnetic superexchange via 3d states of titanium in $eutio_3$ as seen from hybrid hartree-fock density functional calculations. *Physical Review B*, 83(21):214421, 2011.

[3] Hirofumi Akamatsu, Yu Kumagai, Fumiyasu Oba, Koji Fujita, Katsuhisa Tanaka, and Isao Tanaka. Strong spin-lattice coupling through oxygen octahedral rotation in divalent europium perovskites. *Advanced Functional Materials*, 23(15):1864–1872, 2013.

[4] Mattia Allieta, Marco Scavini, Leszek J. Spalek, Valerio Scagnoli, Helen C. Walker, Christos Panagopoulos, Siddharth S. Saxena, Takuro Katsufuji, and Claudio Mazzoli. Role of intrinsic disorder in the structural phase transition of magnetoelectric $eutio_3$. *Phys. Rev. B*, 85:184107, 2012.

[5] P.W. Anderson. More is Different - Broken Symmetry And Nature of Hierarchical Structure of Science. *Science*, 177(4047):393–&, 1972.

[6] Vladimir I. Anisimov, Jan Zaanen, and Ole K. Andersen. Band theory and mott insulators: Hubbard *U* instead of stoner *I*. *Phys. Rev. B*, 44:943–954, Jul 1991.

[7] Vladimir I Anisimov, Jan Zaanen, and Ole K Andersen. Band theory and mott insulators: Hubbard U instead of stoner I. *Physical Review B*, 44:943, 1991.

[8] Armin Antons, J. B. Neaton, Karin M. Rabe, and David Vanderbilt. Tunability of the dielectric response of epitaxially strained $SrTiO_3$ from first principles. *Phys. Rev. B*, 71(2):024102, Jan 2005.

[9] M. I. Aroyo, J. M. Perez-Mato, D. Orobengoa, E. Tasci, G. de la Flor, and A. Kirov. Crystallography online: Bilbao crystallographic server. *Bulgarian Chemical Communications*, 43(2):183–197, 2011.

[10] MI Aroyo, JM Perez-Mato, C Capillas, E Kroumova, S Ivantchev, G Madariaga, A Kirov, and H Wondratschek. Bilbao crystallographic server: I. databases and crystallographic computing programs. *Zeitschrift fur Kristallographie*, 221(1):15–27, 2006.

[11] Mois I. Aroyo, Asen Kirov, Cesar Capillas, J. M. Perez-Mato, and Hans Wondratschek. Bilbao crystallographic server. ii. representations of crystallographic point groups and space groups. *Acta Crystallographica Section A*, 62(2):115–128, Mar 2006.

[12] Masoud Aryanpour, Roald Hoffmann, and Francis J. DiSalvo. Tungsten-doped titanium dioxide in the rutile structure: Theoretical considerations. *Chemistry of Materials*, 21(8):1627–1635, 2009.

[13] Stefano Baroni, Stefano de Gironcoli, Andrea Dal Corso, and Paolo Giannozzi. Phonons and related crystal properties from density-functional perturbation theory. *Rev. Mod. Phys.*, 73:515–562, Jul 2001.

[14] W.H. Baur. The geometry of polyhedral distortions - predictive relationships for the phosphate group. *Acta Crystallographica Section B - Structural Science*, 30:1195–1215, 1974.

[15] Axel D. Becke. A new mixing of Hartree–Fock and local density-functional theories. *The Journal of Chemical Physics*, 98(2):1372–1377, 1993.

[16] A. S. Belozerov, M. A. Korotin, V. I. Anisimov, and A. I. Poteryaev. Monoclinic M_1 phase of vo_2: Mott-hubbard versus band insulator. *Phys. Rev. B*, 85:045109, Jan 2012.

[17] Nicole A. Benedek and Craig J. Fennie. Hybrid improper ferroelectricity: A mechanism for controllable polarization-magnetization coupling. *Phys. Rev. Lett.*, 106:107204, Mar 2011.

[18] I. B. Bersuker and B. G. Vekhter. The vibronic theory of ferroelectricity. *Ferroelectrics*, 19(1):137–150, 1978.

[19] Isaac B. Bersuker. Pseudo jahn-teller origin of perovskite multiferroics, magnetic-ferroelectric crossover, and magnetoelectric effects: The d^0-d^{10} problem. *Phys. Rev. Lett.*, 108:137202, Mar 2012.

[20] Satadeep Bhattacharjee, Eric Bousquet, and Philippe Ghosez. Engineering multiferroism in $CaMnO_3$. *Phys. Rev. Lett.*, 102(11):117602, Mar 2009.

[21] D. I. Bilc and D. J. Singh. Frustration of tilts and *a*-site driven ferroelectricity in knbo$_3$-linbo$_3$ alloys. *Phys. Rev. Lett.*, 96(14):147602, Apr 2006.

[22] Turan Birol, Nicole A. Benedek, Hena Das, Aleksander L. Wysocki, Andrew T. Mulder, Brian M. Abbett, Eva H. Smith, Saurabh Ghosh, and Craig J. Fennie. The magnetoelectric effect in transition metal oxides: Insights and the rational design of new materials from first principles. *Current Opinion in Solid State and Materials Science*, 16(5):227 – 242, 2012.

[23] Turan Birol, Nicole A. Benedek, and Craig J. Fennie. Interface control of emergent ferroic order in Ruddlesden-Popper $Sr_{n+1}Ti_nO_{3n+1}$. *Phys. Rev. Lett.*, 107:257602, Dec 2011.

[24] P. E. Blöchl. Projector augmented-wave method. *Phys. Rev. B*, 50:17953–17979, 1994.

[25] A. A. Bolzan, C. Fong, B. J. Kennedy, and C. J. Howard. A powder neutron-diffraction study of semiconducting and metallic niobium dioxide. *Journal of Solis State Chemistry*, 113(1):9–14, NOV 1994.

[26] A. A. Bolzan, C. Fong, B. J. Kennedy, and C. J. Howard. Structural Studies of Rutile-Type Metal Dioxides. *Acta Crystallographica Section B*, 53(3):373–380, Jun 1997.

[27] A. A. Bolzan, B. J. Kennedy, and C. J. Howard. Neutron powder diffraction study of molybdenum and tungsten dioxides. *Australian Journal of Chemistry*, 48(8):1473–1477, 1995.

[28] M. Born and K. Huang. *Dynamical Theory of Crystal Lattices*. Oxford Classic Texts in the Physical Sciences. Oxford University Press, USA, 1998.

[29] Eric Bousquet, Javier Junquera, and Philippe Ghosez. First-principles study of competing ferroelectric and antiferroelectric instabilities in $BaTiO_3$/BaO superlattices. *Phys. Rev. B*, 82:045426, 2010.

[30] Eric Bousquet and Nicola Spaldin. J dependence in the LSDA+U treatment of noncollinear magnets. *Phys. Rev. B*, 82:220402, Dec 2010.

[31] Eric Bousquet and Nicola Spaldin. Induced magnetoelectric response in *Pnma* perovskites. *Phys. Rev. Lett.*, 107:197603, Nov 2011.

[32] Claudia Bungaro, K. M. Rabe, and A. Dal Corso. First-principles study of

lattice instabilities in ferromagnetic Ni_2MnGa. *Phys. Rev. B*, 68:134104, Oct 2003.

[33] Jeremy K. Burdett. Electronic control of the geometry of rutile and related structures. *Inorganic Chemistry*, 24(14):2244–2253, 1985.

[34] Jeremy K. Burdett and Timothy Hughbanks. Aspects of metal-metal bonding in early-transition-metal dioxides. *Inorganic Chemistry*, 24(12):1741–1750, 1985.

[35] E. Canadell and M.H. Whangbo. Conceptual aspects of structure property correlations and electronic instabilities, with applications to low-dimensional transition-metal oxides. *Chemical Reviews*, 91(5):965–1034, Jul-Aug 1991.

[36] Tay-Rong Chang, Horng-Tay Jeng, Chung-Yuan Ren, and Chen-Shiung Hsue. Charge-orbital ordering and ferroelectric polarization in multiferroic $tbmn_2o_5$ from first principles. *Phys. Rev. B*, 84:024421, Jul 2011.

[37] Chia-Ling Chien, S DeBenedetti, and F De S Barros. Magnetic properties of $EuTiO_3$, Eu_2TiO_4, and $Eu_3Ti_2O_7$. *Physical Review B*, 10(9):3913, 1974.

[38] W. Cochran and R. A. Cowley. Dielectric constants and lattice vibrations. *Journal of Physics and Chemistry of Solids*, 23(5):447–450, 5 1962.

[39] Matteo Cococcioni and Stefano de Gironcoli. *A LDA+U study of selected iron compounds*. PhD thesis, International School for Advanced Studies (SISSA), Trieste, 2002.

[40] M.L. Cohen. Predicting useful materials. *Science*, 261(5119):307–308, 1993.

[41] Ronald E. Cohen. Origin of ferroelectricity in perovskite oxides. *Nature*, 358(6382):136–138, 07 1992.

[42] M. T. Czyzyk and G. A. Sawatzky. Local-density functional and on-site correlations: The electronic structure of La_2CuO_4 and $LaCuO_3$. *Phys. Rev. B*, 49:14211–14228, May 1994.

[43] Oswaldo Diéguez, Karin M. Rabe, and David Vanderbilt. First-principles study of epitaxial strain in perovskites. *Phys. Rev. B*, 72:144101, Oct 2005.

[44] P.A.M. Dirac. On the theory of quantum mechanics. *Proceedings of the Royal Society of London. Series A, Containing Papers of a Mathematical and Physical Character*, 112(762):661–677, Oct 1926.

[45] P.A.M. Dirac. Quantum mechanics of many-electron systems. *Proceedings of the Royal Society of London. Series A, Containing Papers of a Mathematical and Physical Character*, 123(792):714–733, 04 1929.

[46] S. L. Dudarev, G. A. Botton, S. Y. Savrasov, C. J. Humphreys, and A. P. Sutton. Electron-energy-loss spectra and the structural stability of nickel oxide: an LSDA+U study. *Phys. Rev. B*, 57:1505–1509, Jan 1998.

[47] V. Eyert. The metal-insulator transition of NbO_2: An embedded peierls instability. *Europhysics Letters*, 58(6):851, 2002.

[48] V. Eyert. The metal-insulator transitions of VO_2: A band theoretical approach. *Annalen der Physik*, 11(9):650–704, 2002.

[49] V. Eyert. VO_2: A novel view from band theory. *Phys. Rev. Lett.*, 107:016401, Jun 2011.

[50] V Eyert, R Horny, K-H Hck, and S Horn. Embedded peierls instability and the electronic structure of MoO_2. *Journal of Physics: Condensed Matter*, 12(23):4923, 2000.

[51] Craig J. Fennie and Karin M. Rabe. Structural and dielectric properties of Sr_2TiO_4 from first principles. *Phys. Rev. B*, 68(18):184111, Nov 2003.

[52] Craig J. Fennie and Karin M. Rabe. Magnetic and electric phase control in epitaxial $EuTiO_3$ from first principles. *Phys. Rev. Lett.*, 97(26):267602, Dec 2006.

[53] E. Fermi. Un metodo statistico per la determinazione di alcune prioprietà dell'atomo. *Rend. Accad. Naz. Lincei*, 6:602–607, 1927.

[54] R. P. Feynman. Forces in molecules. *Phys. Rev.*, 56:340–343, Aug 1939.

[55] P. A. Fleury, J. F. Scott, and J. M. Worlock. Soft phonon modes and the 110 k phase transition in $SrTiO_3$. *Phys. Rev. Lett.*, 21:16–19, Jul 1968.

[56] A Franceschetti and A Zunger. The inverse hand-structure problem of

finding an atomic configuration with given electronic properties. *Nature*, 402(6757):60–63, 1999.

[57] A. Fujisjima and K. Honda. Electrochemical photolysis of water at a semiconductor electrode. *Nature*, 238(5358):37+, 1972.

[58] Yizhi Ge and Amy Y. Liu. Effect of dimensionality and spin-orbit coupling on charge-density-wave transition in 2H-$TaSe_2$. *Phys. Rev. B*, 86:104101, Sep 2012.

[59] Gregory Geneste, Eric Bousquet, and Philippe Ghosez. New insight into the concept of ferroelectric correlation volume. *Journal of Computational and Theoretical Nanoscience*, 5:517–520(4), 2008.

[60] Antoine Georges, Gabriel Kotliar, Werner Krauth, and Marcelo J. Rozenberg. Dynamical mean-field theory of strongly correlated fermion systems and the limit of infinite dimensions. *Rev. Mod. Phys.*, 68:13–125, Jan 1996.

[61] Francois Gervais and Winfried Kress. Lattice dynamics of oxides with rutile structure and instabilities at the metal-semiconductor phase transitions of NbO_2 and VO_2. *Phys. Rev. B*, 31:4809–4814, Apr 1985.

[62] Ph. Ghosez, J.-P. Michenaud, and X. Gonze. Dynamical atomic charges: The case of ABO_3 compounds. *Phys. Rev. B*, 58(10):6224–6240, Sep 1998.

[63] P.Sc. H. Ghosez, X. Gonze, and J. P. Michenaud. Ab initio phonon dispersion curves and interatomic force constants of Barium Titanate. *Ferroelectrics*, 206(1):205–217, 1998.

[64] Gianluca Giovannetti and Jeroen van den Brink. Electronic correlations decimate the ferroelectric polarization of multiferroic $homn_2o_5$. *Phys. Rev. Lett.*, 100:227603, Jun 2008.

[65] V. Goian, S. Kamba, O. Pacherova, J. Drahokoupil, L. Palatinus, M. Dusek, J. Rohlicek, M. Savinov, F. Laufek, W. Schranz, A. Fuith, M. Kachlik, K. Maca, A. Shkabko, L. Sagarna, A. Weidenkaff, and A. A. Belik. Antiferrodistortive phase transition in $eutio_3$. *Phys. Rev. B*, 86:054112, Aug 2012.

[66] J. B. Goodenough and H. Y-P. Hong. Structures and a two-band model for the system $V_{1-x}Cr_xO_2$. *Phys. Rev. B*, 8:1323–1331, Aug 1973.

[67] John B. Goodenough. Direct cation- -cation interactions in several oxides. *Phys. Rev.*, 117:1442–1451, Mar 1960.

[68] John B. Goodenough. The two components of the crystallographic transition in VO_2. *Journal of Solid State Chemistry*, 3(4):490 – 500, 1971.

[69] J. H. Haeni, C. D. Theis, D. G. Schlom, W. Tian, X. Q. Pan, H. Chang, I. Takeuchi, and X.-D. Xiang. Epitaxial growth of the first five members of the sr[sub n + 1]ti[sub n]o[sub 3n + 1] ruddlesden–popper homologous series. *Applied Physics Letters*, 78(21):3292–3294, 2001.

[70] JH Haeni, P Irvin, W Chang, R Uecker, P Reiche, YL Li, S Choudhury, W Tian, ME Hawley, B Craigo, AK Tagantsev, XQ Pan, SK Streiffer, LQ Chen, SW Kirchoefer, J Levy, and DG Schlom. Room-temperature ferroelectricity in strained $SrTiO_3$. *Nature*, 430(7001):758–761, 2004.

[71] Jurgen Hafner, Christopher Wolverton, and Gerbrand Ceder. Toward computational materials design: The impact of density functional theory on materials research. *MRS Bulletin*, 31:659–665, 2006.

[72] B. A. Hamad. First-principle calculations of structural and electronic properties of rutile-phase dioxides MO_2, M = Ti, V, Ru, Ir and Sn. *The European Physical Journal B - Condensed Matter and Complex Systems*, 70:163–169, 2009. 10.1140/epjb/e2009-00218-0.

[73] DR Hartree. The wave mechanics of an atom with a non-Coulomb central field Part I theory and methods. *Proceedings of the Cambridge Philosophical Society*, 24:89–110, JUL 1928.

[74] Dorian M. Hatch and Harold T. Stokes. Complete listing of order parameters for a crystalline phase transition: A solution to the generalized inverse Landau problem. *Phys. Rev. B*, 65:014113, 2001.

[75] Q. He, E. Arenholz, A. Scholl, Y.-H. Chu, and R. Ramesh. Nanoscale characterization of emergent phenomena in multiferroics. *Current Opinion in Solid State and Materials Science*, 16:216 – 226, 2012.

[76] W Heisenberg. Multi-body problem and resonance in the quantum mechanics. *Zeitschrift fur Physik*, 38(6/7):411–426, AUG 1926.

[77] W Heisenberg. Quantum mechanics. *Naturwissenschaften*, 14:989–994, 1926.

[78] NA Hill. Why are there so few magnetic ferroelectrics? *Journal of Phsical Chemistry B*, 104(29):6694–6709, 2000.

[79] P. Hohenberg and W. Kohn. Inhomogeneous electron gas. *Phys. Rev.*, 136:B864–B871, Nov 1964.

[80] Jiawang Hong, Alessandro Stroppa, Jorge Íñiguez, Silvia Picozzi, and David Vanderbilt. Spin-phonon coupling effects in transition-metal perovskites: A dft+u and hybrid-functional. *Physical Review B*, 85(5):054417, 2012.

[81] R. O. Jones and O. Gunnarsson. The density functional formalism, its applications and prospects. *Rev. Mod. Phys.*, 61:689–746, Jul 1989.

[82] Javier Junquera and Philippe Ghosez. Critical thickness for ferroelectricity in perovskite ultrathin films. *Nature*, 422(6931):506–509, 04 2003.

[83] S. Kamba, V. Goian, M. Orlita, D. Nuzhnyy, J. H. Lee, D. G. Schlom, K. Z. Rushchanskii, M. Ležaić, T. Birol, C. J. Fennie, P. Gemeiner, B. Dkhil, V. Bovtun, M. Kempa, J. Hlinka, and J. Petzelt. Magnetodielectric effect and phonon properties of compressively strained $EuTiO_3$ thin films deposited on (001)LSAT. *Phys. Rev. B*, 85:094435, Mar 2012.

[84] S Kamba, D Nuzhnyy, P Vaněk, M Savinov, K Knížek, Z Shen, E Šantavá, K Maca, M Sadowski, and J Petzelt. Magnetodielectric effect and optic soft mode behaviour in quantum paraelectric $EuTiO_3$ ceramics. *Europhysics Letters*, 80(2):27002, 2007.

[85] T Kasuya. Exchange mechanisms in europium chalcogenides. *IBM Journal of Research and Development*, 14(3):214–&, 1970.

[86] T Katsufuji and H Takagi. Coupling between magnetism and dielectric properties in quantum paraelectric $EuTiO_3$. *Physical Review B*, 64(5):054415, 2001.

[87] DI Khomskii. Multiferroics: Different ways to combine magnetism and ferroelectricity. *Journal of Magnetism and Magnetic Materials*, 306(1):1–8, 2006.

[88] W. Kohn and L. J. Sham. Self-consistent equations including exchange and correlation effects. *Phys. Rev.*, 140:A1133–A1138, Nov 1965.

[89] T. Kolodiazhnyi, K. Fujita, L. Wang, Y. Zong, K. Tanaka, Y. Sakka, and E. Takayama-Muromachi. Magnetodielectric effect in $EuZrO_3$. *Applied Physics Letters*, 96(25), 2010.

[90] Igor Kornev, Huaxiang Fu, and L. Bellaiche. Ultrathin films of ferroelectric solid solutions under a residual depolarizing field. *Phys. Rev. Lett.*, 93(19):196104, Nov 2004.

[91] G. Kotliar, S. Y. Savrasov, K. Haule, V. S. Oudovenko, O. Parcollet, and C. A. Marianetti. Electronic structure calculations with dynamical mean-field theory. *Rev. Mod. Phys.*, 78:865–951, Aug 2006.

[92] G. Kresse and J. Furthmuller. Efficiency of ab-initio total energy calculations for metals and semiconductors using a plane-wave basis set. *Computational Materials Science*, 6(1):15 – 50, 1996.

[93] G. Kresse and J. Furthmüller. Efficient iterative schemes for ab initio total-energy calculations using a plane-wave basis set. *Phys. Rev. B*, 54:11169–11186, Oct 1996.

[94] G. Kresse and D. Joubert. From ultrasoft pseudopotentials to the projector augmented-wave method. *Phys. Rev. B*, 59:1758–1775, Jan 1999.

[95] Kresse, G. and Hafner, J. . Ab initio molecular dynamics for liquid metals. *Phys. Rev. B*, 47(1):558–561, Jan 1993.

[96] Heather J. Kulik, Matteo Cococcioni, Damian A. Scherlis, and Nicola Marzari. Density functional theory in transition-metal chemistry: A self-consistent hubbard U approach. *Phys. Rev. Lett.*, 97:103001, Sep 2006.

[97] Chris Lasota, Cheng-Zhang Wang, Rici Yu, and Henry Krakauer. Ab initio linear response study of $SrTiO_3$. *Ferroelectrics*, 194:109–118, 1997.

[98] J. Laverock, L. F. J. Piper, A. R. H. Preston, B. Chen, J. McNulty, K. E. Smith, S. Kittiwatanakul, J. W. Lu, S. A. Wolf, P.-A. Glans, and J.-H. Guo. Strain dependence of bonding and hybridization across the metal-insulator transition of VO_2. *Phys. Rev. B*, 85:081104, Feb 2012.

[99] Bence Lazarovits, Kyoo Kim, Kristjan Haule, and Gabriel Kotliar. Effects of strain on the electronic structure of VO_2. *Phys. Rev. B*, 81:115117, Mar 2010.

[100] Che-Hui Lee, Nathan D. Orloff, Turan Birol, Ye Zhu, Veronica Goian, Ryan Haislmaier, Eftihia Vlahos, Julia A. Mundy, Yuefeng Nie, Michael D. Biegalski, Jingshu Zhang, Margitta Bernhagen, Nicole A. Benedek, Yongsam Kim, Joel D. Brock, Reinhard Uecker, X. X. Xi, Lena F. Kourkoutis, Venkatraman Gopalan, Dmitry Nuzhnyy, Stanislav Kamba, David A. Muller, Ichiro Takeuchi, James C. Booth, Craig J. Fennie, and Darrell G. Schlom. Exploiting dimensionality and defect mitigation to create tunable microwave dielectrics. *Nature*, 2013.

[101] Jeehye Lee and Tomás A. Arias. Structural phase transitions in ruddlesden-popper phases of strontium titanate: *Ab initio* and modulated ginzburg-landau approaches. *Phys. Rev. B*, 82:180104, Nov 2010.

[102] June Hyuk Lee, Lei Fang, Eftihia Vlahos, Xianglin Ke, Young Woo Jung, Lena Fitting Kourkoutis, Jong-Woo Kim, Philip J Ryan, Tassilo Heeg, Martin Roeckerath, et al. A strong ferroelectric ferromagnet created by means of spin-lattice coupling. *Nature*, 466(7309):954–958, 2010.

[103] A. I. Liechtenstein, V. I. Anisimov, and J. Zaanen. Density-functional theory and strong interactions: Orbital ordering in mott-hubbard insulators. *Phys. Rev. B*, 52:R5467–R5470, Aug 1995.

[104] M.E. Lines and A.M. Glass. *Principles and Applications of Ferroelectrics and Related Materials*. Clarendon Press Oxford, 1977.

[105] A.A. Maradudin. *Lattice dynamics*. Progress in physics. Benjamin, 1969.

[106] BENGT-OLOV Marinder, EBBA Dorm, and MADELEINE Seleborg. Studies on rutile-type phases in mixed transition metal dioxide ii. *Acta Chem. Scand*, 16(2), 1962.

[107] L. W. Martin and R. Ramesh. Multiferroic and magnetoelectric heterostructures. *Acta Materialia*, 60(6-7):2449–2470, 2012.

[108] Lane W. Martin and Darrell G. Schlom. Advanced synthesis techniques and routes to new single-phase multiferroics. *Current Opinion in Solid State and Materials Science*, 16(5):199 – 215, 2012.

[109] R.M. Martin. *Electronic Structure: Basic Theory and Practical Methods*. Cambridge University Press, 2004.

[110] Nicola Marzari, Arash A. Mostofi, Jonathan R. Yates, Ivo Souza, and

David Vanderbilt. Maximally localized wannier functions: Theory and applications. *Rev. Mod. Phys.*, 84:1419–1475, Oct 2012.

[111] TR McGuire, MW Shafer, RJ Joenk, HA Alperin, and SJ Pickart. Magnetic structure of $EuTiO_3$. *Journal of Applied Physics*, 37(3):981–982, 1966.

[112] B. Meyer and David Vanderbilt. Ab initio study of $BaTiO_3$ and $PbTiO_3$ surfaces in external electric fields. *Phys. Rev. B*, 63(20):205426, May 2001.

[113] Koichi Momma and Fujio Izumi. VESTA: A three-dimensional visualization system for electronic and structural analysis. *Journal of Applied Crystallography*, 41:653–658, 2008.

[114] F. J. Morin. Oxides which show a metal-to-insulator transition at the neel temperature. *Phys. Rev. Lett.*, 3:34–36, Jul 1959.

[115] Arash A. Mostofi, Jonathan R. Yates, Young-Su Lee, Ivo Souza, David Vanderbilt, and Nicola Marzari. wannier90: A tool for obtaining maximally-localised wannier functions. *Computer Physics Communications*, 178(9):685 – 699, 2008.

[116] U. Mueller. *Inorganic Structural Chemistry*. Inorganic Chemistry. John Wiley & Sons, 2006.

[117] K. A. Müller and H. Burkard. $SrTi_3$: An intrinsic quantum paraelectric below 4 k. *Phys. Rev. B*, 19:3593–3602, Apr 1979.

[118] Ce-Wen Nan, M. I. Bichurin, Shuxiang Dong, D. Viehland, and G. Srinivasan. Multiferroic magnetoelectric composites: Historical perspective, status, and future directions. *Journal of Applied Physics*, 103(3):031101, 2008.

[119] J. B. Neaton and K. M. Rabe. Theory of polarization enhancement in epitaxial $BaTiO_3/SrTiO_3$ superlattices. *Applied Physics Letters*, 82(10):1586–1588, 2003.

[120] R. E. Newnham. Phase transformations in smart materials. *Acta Crystallographica Section A*, 54(6-1):729–737, 1998.

[121] N. D. Orloff, W. Tian, C. J. Fennie, C. H. Lee, D. Gu, J. Mateu, X. X. Xi, K. M. Rabe, D. G. Schlom, I. Takeuchi, and J. C. Booth. Broadband dielectric

spectroscopy of Ruddlesden–Popper $Sr_{n+1}Ti_nO_{3n+1}$ (n = 1,2,3) thin films. *Applied Physics Letters*, 94(4):042908, 2009.

[122] J. Paier, M. Marsman, K. Hummer, G. Kresse, I. C. Gerber, and J. G. Angyan. Screened hybrid density functionals applied to solids. *The Journal of Chemical Physics*, 124(15):154709, 2006.

[123] Victor Pardo and Warren E. Pickett. Metal-insulator transition through a semi-dirac point in oxide nanostructures: VO_2 (001) layers confined within TiO_2. *Phys. Rev. B*, 81:035111, Jan 2010.

[124] Hyowon Park, Andrew J. Millis, and Chris A. Marianetti. Site-selective mott transition in rare-earth-element nickelates. *Phys. Rev. Lett.*, 109:156402, Oct 2012.

[125] J. E. Pask, D. J. Singh, I. I. Mazin, C. S. Hellberg, and J. Kortus. Structural, electronic, and magnetic properties of MnO. *Phys. Rev. B*, 64:024403, Jun 2001.

[126] J. P. Perdew and Alex Zunger. Self-interaction correction to density-functional approximations for many-electron systems. *Phys. Rev. B*, 23:5048–5079, May 1981.

[127] John P. Perdew, Kieron Burke, and Matthias Ernzerhof. Generalized gradient approximation made simple. *Phys. Rev. Lett.*, 77:3865–3868, Oct 1996.

[128] John P. Perdew, Matthias Ernzerhof, and Kieron Burke. Rationale for mixing exact exchange with density functional approximations. *The Journal of Chemical Physics*, 105(22):9982–9985, 1996.

[129] John P. Perdew, Robert G. Parr, Mel Levy, and Jose L. Balduz. Density-functional theory for fractional particle number: Derivative discontinuities of the energy. *Phys. Rev. Lett.*, 49:1691–1694, Dec 1982.

[130] J. M. Perez-Mato, D. Orobengoa, and M. I. Aroyo. Mode crystallography of distorted structures. *Acta Crystallographica Section A*, 66:558–590, 2010.

[131] Robert M. Pick, Morrel H. Cohen, and Richard M. Martin. Microscopic theory of force constants in the adiabatic approximation. *Phys. Rev. B*, 1:910–920, Jan 1970.

[132] S. Picozzi and A. Stroppa. Advances in ab-initio theory of multiferroics. *European Physical Journal B*, 85(7):1–22, 2012.

[133] K.M. Rabe, C.H. Ahn, and J.M. Triscone. *Physics of Ferroelectrics: A Modern Perspective*. Topics in applied physics. Springer-Verlag Berlin/Heidelberg, 2007.

[134] Rajeev Ranjan, Hasan Sadat Nabi, and Rossitza Pentcheva. Electronic structure and magnetism of $EuTiO_3$: a first-principles study. *Journal of Physics: Condensed Matter*, 19(40):406217, 2007.

[135] Rajeev Ranjan, Hasan Sadat Nabi, and Rossitza Pentcheva. First principles study of magnetism in divalent eu perovskites. *Journal of Applied Physics*, 105(5):053905–053905, 2009.

[136] Keith Robinson, G. V. Gibbs, and P. H. Ribbe. Quadratic elongation: A quantitative measure of distortion in coordination polyhedra. *Science*, 172(3983):567–570, 1971.

[137] Efrain E. Rodriguez, Frederic Poineau, Anna Llobet, Alfred P. Sattelberger, Joydeep Bhattacharjee, Umesh V. Waghmare, Thomas Hartmann, and Anthony K. Cheetham. Structural studies of TcO_2 by neutron powder diffraction and first-principles calculations. *Journal of the American Chemical Society*, 129(33):10244–10248, 2007.

[138] Donald B. Rogers, Robert D. Shannon, Arthur W. Sleight, and Joseph L. Gillson. Crystal chemistry of metal dioxides with rutile-related structures. *Inorganic Chemistry*, 8(4):841–849, 1969.

[139] D. Romanov and V. Skrobot. Distortions of octahedra in rutile-type structures of transition element dioxides. *Glass Physics and Chemistry*, 35:518–524, 2009. 10.1134/S1087659609050101.

[140] S. N. Ruddlesden and P. Popper. New compounds of the K_2NiF_4 type. *Acta. Crystallogr.*, 10:538, 1957.

[141] S. N. Ruddlesden and P. Popper. The compound $Sr_3Ti_2O_7$ and its structure. *Acta. Crystallogr.*, 11:54, 1958.

[142] Konstantin Z Rushchanskii, Nicola A Spaldin, and Marjana Ležaić. First-principles prediction of oxygen octahedral rotations in perovskite-structure $EuTiO_3$. *Physical Review B*, 85(10):104109, 2012.

[143] PJ Ryan, J-W Kim, T Birol, P Thompson, J-H Lee, X Ke, PS Normile, E Karapetrova, P Schiffer, SD Brown, CJ Fennie, and DG Schlom. Reversible control of magnetic interactions by electric field in a single phase material. *Nature Communications*, 4:1334, 2013.

[144] Na Sai, Alexie M. Kolpak, and Andrew M. Rappe. Ferroelectricity in ultrathin perovskite films. *Phys. Rev. B*, 72(2):020101, Jul 2005.

[145] Na Sai and David Vanderbilt. First-principles study of ferroelectric and antiferrodistortive instabilities in tetragonal $SrTiO_3$. *Phys. Rev. B*, 62:13942–13950, Dec 2000.

[146] G. A. Samara, T. Sakudo, and K. Yoshimitsu. Important generalization concerning the role of competing forces in displacive phase transitions. *Phys. Rev. Lett.*, 35(26):1767–1769, 1975.

[147] D.G. Schlom, L.-Q. Chen, C.-B. Eom, K. M. Rabe, S. K. Streiffer, and J.-M. Triscone. Strain tuning of ferroelectric thin films. *Annual Review of Materials Research*, 37(1):589–626, 2007.

[148] N. Schonberg. An X-ray investigation of the tantalum-oxygen system. *Acta Chemica Scandinavica*, 8(2):240–245, 1954.

[149] R.D. Shannon. Synthesis and properties of two new members of the rutile family RhO_2 and PtO_2. *Solid State Communications*, 6(3):139 – 143, 1968.

[150] D. J. Singh, M. Ghita, M. Fornari, and S. V. Halilov. Role of A-site and B-site ions in perovskite ferroelectricity. *Ferroelectrics*, 338:1489+, 2006.

[151] D. J. Singh and Chul Hong Park. Polar behavior in a magnetic perovskite from *a*-site size disorder: A density functional study. *Phys. Rev. Lett.*, 100(8):087601, Feb 2008.

[152] T.P. Sleight, C.R. Hare, and A.W. Sleight. Metal-metal bonding in $La_4Re_6O_19$ and rutile related dioxides. *Materials Research Bulletin*, 3(5):437 – 444, 1968.

[153] Peter I. Sorantin and Karlheinz Schwarz. Chemical bonding in rutile-type compounds. *Inorganic Chemistry*, 31(4):567–576, 1992.

[154] Nicola A. Spaldin and Warren E. Pickett. Computational design of multifunctional materials. *Journal of Solid State Chemistry*, 176:615 – 632, 2003.

[155] Massimiliano Stengel and Nicola A. Spaldin. Origin of the dielectric dead layer in nanoscale capacitors. *Nature*, 443(7112):679–682, OCT 12 2006.

[156] Harold T. Stokes, Dorian M. Hatch, and James D. Wells. Group-theoretical methods for obtaining distortions in crystals: Applications to vibrational modes and phase transitions. *Phys. Rev. B*, 43:11010–11018, 1991.

[157] H.T. Stokes, D.M Hatch, and B.J. Campbell. Isotropy, 2007.

[158] Alessandro Stroppa, Martijn Marsman, Georg Kresse, and Silvia Picozzi. The multiferroic phase of dyfeo 3 : an ab initio study. *New Journal of Physics*, 12(9):093026, 2010.

[159] Jianwei Sun, Martijn Marsman, Gábor I. Csonka, Adrienn Ruzsinszky, Pan Hao, Yoon-Suk Kim, Georg Kresse, and John P. Perdew. Self-consistent meta-generalized gradient approximation within the projector-augmented-wave method. *Phys. Rev. B*, 84:035117, Jul 2011.

[160] Jianmin Tao, John P. Perdew, Viktor N. Staroverov, and Gustavo E. Scuseria. Climbing the density functional ladder: Nonempirical meta-generalized gradient approximation designed for molecules and solids. *Phys. Rev. Lett.*, 91:146401, Sep 2003.

[161] Zhensheng Tao, Tzong-Ru T. Han, Subhendra D. Mahanti, Phillip M. Duxbury, Fei Yuan, Chong-Yu Ruan, Kevin Wang, and Junqiao Wu. Decoupling of structural and electronic phase transitions in VO_2. *Phys. Rev. Lett.*, 109:166406, Oct 2012.

[162] E. S. Tasci, G. de La Flor, D. Orobengoa, C. Capillas, J. M. Perez-Mato, and M. I. Aroyo. An introduction to the tools hosted in the bilbao crystallographic server. In *European Physical Journal Web of Conferences*, volume 22 of *European Physical Journal Web of Conferences*, page 9, March 2012.

[163] LH Thomas. The calculation of atomic fields. *Proceedings of the Cambridge Philosophical Society*, 23:542–548, 1927.

[164] W. Tian, X.Q. Pan, J.H. Haeni, and D.G. Schlom. Transmission electron microscopy study of n=1-5 $Sr_{n+1}Ti_nO_{3n+1}$ epitaxial thin films. *J. Mater. Res.*, 16(7):2001, 2001.

[165] Y Tokura. Critical features of colossal magnetoresistive manganites. *Reports on Progress in Physics*, 69(3):797, 2006.

[166] Yoshihiro Tsujimoto, Kazunari Yamaura, and Eiji Takayama-Muromachi. Oxyfluoride chemistry of layered perovskite compounds. *Applied Sciences*, 2(1):206–219, 2012.

[167] L. Vegard. Results of crystal analysis - III. *Philosophical Magazine*, 32(187-92):505–518, Jul-Dec 1916.

[168] R. V. Wang, D. D. Fong, F. Jiang, M. J. Highland, P. H. Fuoss, Carol Thompson, A. M. Kolpak, J. A. Eastman, S. K. Streiffer, A. M. Rappe, and G. B. Stephenson. Reversible chemical switching of a ferroelectric film. *Phys. Rev. Lett.*, 102(4):047601, Jan 2009.

[169] H.E. Weaver. Dielectric properties of single crystals of srtio3 at low temperatures. *Journal of Physics and Chemistry of Solids*, 11:274 – 277, 1959.

[170] Cédric Weber, David D. O'Regan, Nicholas D. M. Hine, Mike C. Payne, Gabriel Kotliar, and Peter B. Littlewood. Vanadium dioxide: A peierls-mott insulator stable against disorder. *Phys. Rev. Lett.*, 108:256402, Jun 2012.

[171] M.H. Whangbo, E. Canadell, P. Foury, and J.P. Pouget. Hidden fermi surface nesting and charge density wave instability in low-dimensional metals. *Science*, 252(5002):96–98, 1991.

[172] P. M. Woodward. Octahedral tilting in perovskites. ii. structure stabilizing forces. *Acta Crystallographica Section B*, 53(1):44–66, 1997.

[173] Yurong Yang, Wei Ren, Dawei Wang, and L Bellaiche. Understanding and revisiting properties of $EuTiO_3$ bulk material and films from first principles. *Physical Review Letters*, 109(26):267602, 2012.

[174] Z. P. Yin and G. Kotliar. Rational material design of mixed-valent high-tc superconductors. *Europhysics Letters*, 101, 2013.

[175] Rici Yu and Henry Krakauer. First-principles determination of chain-structure instability in KNbO3. *Phys. Rev. Lett.*, 74(20):4067–4070, May 1995.

[176] W. Zhong and David Vanderbilt. Effect of quantum fluctuations on structural phase transitions in $SrTiO_3$ and $BaTiO_3$. *Phys. Rev. B*, 53:5047–5050, Mar 1996.